

**International Ocean Discovery Program  
Expedition 349 Preliminary Report**

**South China Sea Tectonics**

**Opening of the South China Sea and its implications for  
southeast Asian tectonics, climates, and deep mantle  
processes since the late Mesozoic**

26 January–30 March 2014

Expedition 349 Scientists



Published by  
International Ocean Discovery Program

## Publisher's notes

Material in this publication may be copied without restraint for library, abstract service, educational, or personal research purposes; however, this source should be appropriately acknowledged. Core samples and the wider set of data from the science program covered in this report are under moratorium and accessible only to Science Party members until 30 March 2015.

This publication was prepared by the International Ocean Discovery Program U.S. Implementing Organization (IODP-USIO): Consortium for Ocean Leadership, Lamont-Doherty Earth Observatory of Columbia University, and Texas A&M University, as an account of work performed under the International Ocean Discovery Program. Funding for the program is provided by the following agencies:

National Science Foundation (NSF), United States

Ministry of Education, Culture, Sports, Science and Technology (MEXT), Japan

European Consortium for Ocean Research Drilling (ECORD)

Ministry of Science and Technology (MOST), People's Republic of China

Korea Institute of Geoscience and Mineral Resources (KIGAM)

Australian Research Council (ARC) and GNS Science (New Zealand), Australian/New Zealand Consortium

Ministry of Earth Sciences (MoES), India

Coordination for Improvement of Higher Education Personnel, Brazil

## Disclaimer

Any opinions, findings, and conclusions or recommendations expressed in this publication are those of the author(s) and do not necessarily reflect the views of the participating agencies, Consortium for Ocean Leadership, Lamont-Doherty Earth Observatory of Columbia University, Texas A&M University, or Texas A&M Research Foundation.

Portions of this work may have been published in whole or in part in other International Ocean Discovery Program documents or publications.

## Copyright

Except where otherwise noted, this work is licensed under a [Creative Commons Attribution License](#). Unrestricted use, distribution, and reproduction is permitted, provided the original author and source are credited.

Citation:

Expedition 349 Scientists, 2014. South China Sea tectonics: opening of the South China Sea and its implications for southeast Asian tectonics, climates, and deep mantle processes since the late Mesozoic. *International Ocean Discovery Program Preliminary Report*, 349. <http://dx.doi.org/10.14379/iodp.pr.349.2014>

## ISSN

World Wide Web: 2372-9562

## Expedition 349 participants

### Expedition 349 scientists

**Chun-Feng Li**  
**Co-chief Scientist**  
State Key Laboratory of Marine Geology  
Tongji University  
1239 Siping Road  
200092 Shanghai  
China  
[cfl@tongji.edu.cn](mailto:cfl@tongji.edu.cn)

**Jian Lin**  
**Co-chief Scientist**  
Department of Geology and Geophysics  
Woods Hole Oceanographic Institution  
360 Woods Hole Road  
Woods Hole MA 02543  
USA  
[jlin@whoi.edu](mailto:jlin@whoi.edu)

**Denise K. Kulhanek**  
**Expedition Project Manager/Staff Scientist**  
International Ocean Discovery Program  
Texas A&M University  
1000 Discovery Drive  
College Station TX 77845-9547  
USA  
[kulhanek@iodp.tamu.edu](mailto:kulhanek@iodp.tamu.edu)

**Trevor Williams**  
**Logging Staff Scientist**  
Borehole Research Group  
Lamont-Doherty Earth Observatory  
of Columbia University  
PO Box 1000, 61 Route 9W  
Palisades NY 10964  
USA  
[trevor@ldeo.columbia.edu](mailto:trevor@ldeo.columbia.edu)

**Rui Bao**  
**Organic Geochemist**  
Geologisches Institut  
Swiss Federal Institute of Technology (ETH  
Zürich)  
Sonneggstrasse 5, NO E57  
8092 Zürich  
Switzerland  
[ruibao@erdw.ethz.ch](mailto:ruibao@erdw.ethz.ch)

**Anne Briaïs**  
**Physical Properties Specialist**  
Géosciences Environnement Toulouse  
Centre National de la Recherche Scientifique  
(CNRS)  
Observatoire Midi-Pyrénées, University  
of Toulouse  
14 Avenue Edouard Belin  
31400 Toulouse  
France  
[anne.briaïs@get.obs-mip.fr](mailto:anne.briaïs@get.obs-mip.fr)

**Elizabeth A. Brown**  
**Paleontologist (foraminifers)**  
College of Marine Science  
University of South Florida  
140 7th Avenue South  
St. Petersburg FL 33701  
USA  
[eabrown@mail.usf.edu](mailto:eabrown@mail.usf.edu)

**Yifeng Chen**  
**Inorganic Geochemist**  
Key Laboratory of Marginal Sea Geology  
Guangzhou Institute of Geochemistry,  
Chinese Academy of Sciences  
511 Kehua Street, Tianhe District  
510640 Guangzhou  
China  
[yfchen@gig.ac.cn](mailto:yfchen@gig.ac.cn)

**Peter D. Clift**  
**Sedimentologist**  
Department of Geology and Geophysics  
Louisiana State University  
E253 Howe-Russell-Kniffen Geoscience  
Complex  
Baton Rouge LA 70803  
USA  
[pclift@lsu.edu](mailto:pclift@lsu.edu)

**Frederick S. Colwell**  
**Microbiologist**  
College of Earth, Ocean and Atmospheric  
Sciences  
Oregon State University  
104 CEOAS Administration Building  
Corvallis OR 97331-5503  
USA  
[rcolwell@coas.oregonstate.edu](mailto:rcolwell@coas.oregonstate.edu)

**Kelsie A. Dadd**  
**Sedimentologist**  
Department of Earth and Planetary Sciences  
Macquarie University  
Sydney NSW 2109  
Australia  
[kelsie.dadd@mq.edu.au](mailto:kelsie.dadd@mq.edu.au)

**Weiwei Ding**  
**Structural Geologist**  
Key Laboratory of Submarine Geoscience  
Second Institute of Oceanography,  
State Oceanic Administration  
36 Baochubei Road  
310012 Hangzhou  
China  
[wwding@gmail.com](mailto:wwding@gmail.com)

**Iván Hernández Almeida**  
**Paleontologist (radiolarians)**  
Institute of Geography/Oeschger Centre  
for Climate Change Research  
University of Bern  
Erlachstrasse 9a  
3012 Bern  
Switzerland  
[ivan.hernandez@giub.unibe.ch](mailto:ivan.hernandez@giub.unibe.ch)

**Xiao-Long Huang**  
**Inorganic Geochemist**  
State Key Laboratory of Isotope Geochemistry  
Guangzhou Institute of Geochemistry,  
Chinese Academy of Sciences  
511 Kehua Street, Tianhe District  
510640 Guangzhou  
China  
[xlhuang@gig.ac.cn](mailto:xlhuang@gig.ac.cn)

**Sangmin Hyun**  
**Sedimentologist**  
Marine Environment and Conservation  
Research Division  
Korea Institute of Ocean Science and  
Technology (KIOST)  
787 Haeanlo  
Ansan426-744  
Republic of Korea  
[smhyun@kiost.ac](mailto:smhyun@kiost.ac)

**Tao Jiang**  
**Sedimentologist**  
Department of Marine Science and  
Engineering  
Faculty of Earth Resources  
China University of Geosciences  
388 Lumo Road  
Wuhan 430074  
P.R. China  
[taojiang@cug.edu.cn](mailto:taojiang@cug.edu.cn)  
Secondary address:  
Kochi Institute for Core Sample Research  
Japan Agency for Marine-Earth Science and  
Technology (JAMSTEC)  
200 Monobe-Otsu  
Nanko-ku, Kochi  
783-8502  
Japan  
[jiangtao@jamstec.go.jp](mailto:jiangtao@jamstec.go.jp)

**Anthony A.P. Koppers**  
**Petrologist**  
College of Earth, Ocean and Atmospheric  
Sciences  
Oregon State University  
104 CEOAS Administration Building  
Corvallis OR 97331  
USA  
[akoppers@coas.oregonstate.edu](mailto:akoppers@coas.oregonstate.edu)

**Qianyu Li**  
**Paleontologist (foraminifers)**  
School of Ocean and Earth Sciences  
Tongji University  
1239 Siping Road  
200092 Shanghai  
China  
[qli01@tongji.edu.cn](mailto:qli01@tongji.edu.cn)

**Chuanlian Liu**  
**Paleontologist (nannofossils)**  
School of Ocean and Earth Sciences  
Tongji University  
1239 Siping Road  
200092 Shanghai  
China  
[liucl@tongji.edu.cn](mailto:liucl@tongji.edu.cn)

**Qingsong Liu**  
**Paleomagnetist**  
State Key Laboratory of Lithospheric  
Evolution  
Institute of Geology and Geophysics,  
Chinese Academy of Sciences  
19 Beitucheng Western Road  
Chaoyang District  
100029 Beijing  
China  
[qslu@mail.iggcas.ac.cn](mailto:qslu@mail.iggcas.ac.cn)

**Zhifei Liu**  
**Sedimentologist**  
State Key Laboratory of Marine Geology  
Tongji University  
1239 Siping Road  
200092 Shanghai  
China  
[lzhifei@tongji.edu.cn](mailto:lzhifei@tongji.edu.cn)

**Renata H. Nagai**  
**Paleontologist (foraminifers)**  
Department of Physical, Chemical and  
Geological Oceanography  
Instituto Oceanográfico  
Universidade de São Paulo  
191 sala 171 Praça do Oceanográfico  
05508-120 São Paulo-SP  
Brazil  
[renatanagai@usp.br](mailto:renatanagai@usp.br)

**Alyssa Peleo-Alampay**  
**Observer/Paleontologist (nannofossils)**  
National Institute of Geological Sciences  
University of the Philippines  
Diliman  
1101 Quezon City  
Philippines  
[ampanigs@yahoo.com](mailto:ampanigs@yahoo.com)

**Xin Su**  
**Paleontologist (nannofossils)**  
School of Marine Geosciences  
China University of Geosciences  
29 Xueyuan Road  
100083 Beijing  
China  
[xsu@cugb.edu.cn](mailto:xsu@cugb.edu.cn)

**Zhen Sun**  
**Structural Geologist**  
Department of Marine Geology  
South China Sea Institute of Oceanology  
164 Xingangxi Road  
510301 Guangzhou  
China  
[zhensun@scsio.ac.cn](mailto:zhensun@scsio.ac.cn)

**Maria Luisa (Marissa) G. Tejada**  
**Petrologist**  
Japan Agency for Marine-Earth Science and  
Technology (JAMSTEC)  
2-15 Natsushima-cho, Yokosuka-shi  
Kanagawa  
237-0061  
Japan  
[mtejada@jamstec.go.jp](mailto:mtejada@jamstec.go.jp)

**Hai Son Trinh**  
**Observer/Physical Properties Specialist**  
Department of Science and Technology  
Ministry of Natural Resources and  
Environment (MONRE)  
10 Ton That Thuyet Street  
Hanoi  
Vietnam  
[thaison@monre.gov.vn](mailto:thaison@monre.gov.vn)

**Yi-Ching Yeh**  
**Observer/Physical Properties Specialist**  
Taiwan Ocean Research Institute  
219 Dongfang Road, Section 1  
Kaohsiung City 852  
Taiwan  
[ycyeh@narlabs.org.tw](mailto:ycyeh@narlabs.org.tw)

**Chuanlun Zhang**  
**Organic Geochemist**  
School of Ocean and Earth Sciences  
Tongji University  
1239 Siping Road  
200092 Shanghai  
China  
[archaea.zhang@gmail.com](mailto:archaea.zhang@gmail.com)

**Fan Zhang**  
**Physical Properties Specialist**  
Department of Geology and Geophysics  
Woods Hole Oceanographic Institution  
243 Clark Laboratory  
266 Woods Hole Road  
Woods Hole MA 02543  
USA  
[fzhang@whoi.edu](mailto:fzhang@whoi.edu)

**Guo-Liang Zhang**  
**Petrologist**  
Key Laboratory of Marine Geology and  
Environment  
Institute of Oceanology, Chinese Academy  
of Sciences  
7 Nanhai Road  
266071 Qingdao  
China  
[zhangguoliang@qdio.ac.cn](mailto:zhangguoliang@qdio.ac.cn)

**Xixi Zhao**  
**Paleomagnetist**  
Department of Earth and Planetary Sciences  
University of California, Santa Cruz  
1156 High Street  
Santa Cruz CA 95064  
USA  
[xzhao@ucsc.edu](mailto:xzhao@ucsc.edu)

## Education and outreach

**Haopeng Tang**  
**Reporter**  
TV News Center, Shanghai Media Group  
298 Weihai Road  
200041 Shanghai  
China

## Abstract

The South China Sea (SCS) provides an outstanding opportunity to better understand complex patterns of continental margin breakup and basin formation. The sea is situated at the junction of the Eurasian, Pacific, and Indo-Australian plates and is a critical site linking some of the major western Pacific tectonic units. Despite extensive studies, sampling of basement rock and directly overlying basal sediment in the deep basin is lacking. This leaves a large margin of error in estimated ages of the SCS opening and closing, rendering various hypotheses regarding its opening mechanism and history untested. This also hampers understanding of East Asian tectonic and paleo-environmental evolution.

We drilled five sites in the deep basin of the SCS. Three of these sites (U1431, U1433, and U1434) cored into oceanic basement near the fossil spreading center. The two remaining sites (U1432 and U1435) are located proximal to the northern continent/ocean boundary. We recovered a total of 1524 m of sediment/sedimentary rock and 78 m of oceanic basalt and also carried out downhole geophysical logging (triple combination and Formation MicroScanner-sonic tool strings) at the two deepest sites (U1431 and U1433). These materials and data were extensively examined and discussed during the expedition and allowed us to draw the following principal conclusions on the opening of the SCS:

1. Based on shipboard dating of microfossils in the sediment immediately above the basaltic basement and between the lava flow units, the preliminary cessation age of spreading in both the East and Southwest Subbasins is around early Miocene (16–20 Ma). Further postcruise radiometric dating of basement basalt from these sites plus additional calibration of magnetic anomaly models and paleomagnetic measurements will further refine the age range. Overall, a large difference is not apparent in the terminal ages of seafloor spreading between the two subbasins.
2. At Site U1435, we were able to drill into a structural high standing along the continent/ocean boundary. Coring at this site recovered a sharp unconformity at ~33 Ma, above which is marine sediment and below which are poorly sorted sandstone and black mudstone, interpreted as littoral deposits. Environmental interpretation will require further shore-based studies because the sequence is almost entirely barren of marine microfossils. Nevertheless, we interpret this unconformity to be likely directly related to the continental break-up during the

initial opening of the SCS. The onset of seafloor spreading is therefore estimated to be at ~33 Ma.

3. All sites contain deep marine deposits but show significant areal variations in postspreading sedimentary environment and provenance. Site U1431 records evidence for deep-marine turbidite deposition from terrestrial sources. The observed coarser silt turbidites may have a source in Taiwan or other surrounding blocks, whereas interbedded calcareous turbidites at this site could be transported from local sources, such as nearby seamounts topped by carbonate platforms. In contrast, the source for upper Miocene clay and silt turbidites at Site U1433 could be from Borneo or mainland Southeast Asia, with the source of the interbedded carbonate turbidites likely from the Dangerous Grounds or Reed Bank area located south of the site.
4. Sites U1431 and U1434 are close to seamounts developed along the relict spreading center. Occurrences of basaltic clasts and mineral fragments in the volcanoclastic sandstone and breccia may reveal the magmatic history and mantle source of the seamounts and potentially their relationship with the terminal processes of spreading. The volcanoclastic breccia and sandstone at Site U1431 are dated as late middle Miocene to early late Miocene (~8–13 Ma), suggesting a 5 m.y. duration of seamount volcanism starting a few million years after the cessation of seafloor spreading. At Site U1434, volcanoclastic breccia and sandstone are most likely sourced from the adjacent seamount ~15 km to the north. The age of this recovered unit is late Miocene (younger than 9 Ma). Further postcruise sedimentological and geochemical studies, as well as radiometric dating of potassium-bearing mineral fragments, will refine the ages and timing of these seamount activities and reveal how magma sources at the dying spreading center evolved through time.
5. We successfully cored into ocean basement in the SCS for the first time and recovered basalt at three sites (U1431, U1433, and U1434). The cored basalt has variable phase assemblages of plagioclase, olivine, and clinopyroxene and is concluded to be typical mid-ocean-ridge basalt based on petrological and geochemical evidence. Postcruise radiometric dating will determine the absolute ages of the basaltic basement units. Postcruise petrological and geochemical analyses on the basalts will provide information on the mantle sources, melting, and crystallization history of the youngest ocean crust.

## Introduction

Since the late Mesozoic, the South China Sea (SCS) area (Figs. F1, F2) has been at the center of many first-order tectonic and paleoclimatic events. Mesozoic subduction of the paleo-Pacific plate under the Eurasian plate partially occurred along the present-day northeastern SCS continental margin (Jahn et al., 1976; Hilde et al., 1977; Hamilton, 1979; Holloway, 1982; Taylor and Hayes, 1983; Hayes et al., 1995; Zhou and Li, 2000; Yang and Feng, 2003; Xiao and Zheng, 2004; Zhou et al., 2008; Li et al., 2008a). This subduction resulted in the emplacement of igneous rocks and the formation of a wide orogenic belt in Southeast Asia (Zhou and Li, 2000; Shi and Li, 2012). Subduction is thought to have ceased in the mid-Cretaceous, with a transition to regional extension during the Late Cretaceous. Opening of the SCS began in the Cenozoic through continental breakup and subsequent seafloor spreading. The Ailao Shan-Red River strike-slip fault also displaced the Indochina block by hundreds of kilometers during the Oligocene and Miocene (Tapponnier et al., 1986, 1990; Lacassin et al., 1997; Leloup et al., 2001; Gilley et al., 2003). The early work of Taylor and Hayes (1980, 1983) and Briaies et al. (1993) suggested that the SCS opened from ~32 to ~16 Ma during the Oligocene and early Miocene. Recently, Barckhausen and Roeser (2004) and Barckhausen et al. (2014) argued that seafloor spreading was faster in the later stages than at the beginning of the opening and ceased at 20.5 Ma (Anomaly 6a1) over the entire SCS, ~4 m.y. earlier than interpreted in previous studies.

Ages of the oceanic crust in the SCS Basin are only constrained from magnetic anomaly correlations and empirical relationships between ages and bathymetry and/or heat flow. The uncertainties in the timing and episodes of the Cenozoic opening of the SCS hamper understanding of other key geological processes in Southeast Asia, including the geodynamic transition from Mesozoic subduction to Cenozoic rifting, the relationship between the motion on the large strike-slip faults and the extension (extrusion), the Cenozoic opening mechanism, oceanic crustal accretion and mantle evolution, and paleoceanographic and sedimentary responses. In order to address regional questions related to East Asian geology and fundamental issues regarding continental breakup and the mechanism through which the SCS Basin opened, it is essential to determine when seafloor spreading initiated and when it ceased. To do this, during Expedition 349 we drilled into the oceanic basement and retrieved both sedimentary and basaltic rocks from two subbasins of the SCS. Drilling and coring into igneous basement is the only means of validating various opening mechanisms.

Expedition 349 was based on Integrated Ocean Drilling Program Proposal 735-CPP2, developed in part from results of an international workshop held at Tongji University in Shanghai, China, in early 2012 (Li et al., 2012). The primary objectives of the expedition fall under four major categories and address the Earth Connections and Climate and Ocean Change themes in the science plan for the International Ocean Discovery Program (IODP) (available at [www.iodp.org/science-plan-for-2013-2023](http://www.iodp.org/science-plan-for-2013-2023)):

1. To examine the mechanisms, timing, and sequences of Cenozoic seafloor spreading; to establish the complex opening history of different subbasins and styles of oceanic crustal accretion in the SCS; and to constrain the tectonic controls (such as spreading rate) on distinct magnetic contrasts among the subbasins;
2. To examine oceanic crustal accretion and mantle evolution and reveal the crustal nature and affinities of different subbasins in order to understand oceanic crustal and deep mantle processes associated with tectonic extrusion, magmatism, and magnetization;
3. To examine paleoceanographic and sedimentary responses to tectonic evolution of the SCS through development of a more complete 3-D sedimentation and subsidence model and linking it to regional climatic processes in response to various tectonic events; and
4. To examine driving forces leading to continental breakup and seafloor spreading and constrain whether the forces were far-field (triggered by the tectonic extrusion of the Indochina block), near-field (due to back-arc spreading or slab pull), or in situ (mantle plume and magmatism driven) in order to deepen our general understanding of the geodynamic interplay of mantle and lithosphere processes that led to the development of continental margin basins in the geological past and today.

## Background

### Geological setting

The SCS is a western Pacific marginal sea situated at the junction of the Eurasian, Pacific, and Indo-Australian plates. It developed from Cenozoic continental margin rifting, and its central portion is floored with oceanic crust. Despite its relatively small size and short evolutionary history, the SCS has undergone nearly a complete Wilson cycle from continental breakup to seafloor spreading to subduction and is well suited for studying various plate boundary activities, such as continental margin rifting

(e.g., Hayes and Nissen, 2005), seafloor subduction (the Manila Trench; e.g., Li et al., 2007a), strike-slip faulting (the Ailao Shan-Red River fault; e.g., Leloup et al., 2001; Clift and Sun, 2006), and active orogenic processes (Taiwan; e.g., Huang et al., 2001) (Fig. **F1**).

Hypotheses for the opening mechanism of the SCS differ markedly (Fig. **F3**) and include

1. India-Eurasia collision and the consequent tectonic extrusion mainly along the Ailao Shan-Red River fault (Fig. **F3A**) (Tapponnier et al., 1982; Lallemand and Jolivet, 1986; Schärer et al., 1990; Briais et al., 1993; Flower et al., 2001; Leloup et al., 2001),
2. Slab pull and subduction of the proto-SCS under Sabah/Borneo (Fig. **F3B**) (Taylor and Hayes, 1980, 1983; Holloway, 1982; Hall, 2002),
3. Extension related to an upwelling mantle plume (Fig. **F3C**) (e.g., Fan and Menzies, 1992; Xu et al., 2012), and
4. Regional extension related to subduction and retreat of the Pacific plate along the western Pacific margin (Fig. **F3D**) (Taylor and Hayes, 1980, 1983; Shi and Li, 2012).

In addition to these end-member models, hybrid models have been proposed (e.g., Cullen et al., 2010).

The original SCS Basin before its subduction along the Manila Trench may have been twice the size that it is today (Sibuet et al., 2002), so geodynamic models must be able to explain the formation of this larger ocean basin. The Ailao Shan-Red River fault was active from 35 to 15 Ma, with displacement of as much as several hundred kilometers (e.g., Leloup et al., 2001; Gilley et al., 2003). Ages obtained from sites drilled during Expedition 349 will aid in testing the hypothesis that the motion on the Ailao Shan-Red River fault is coeval to and may have driven part of the extension and spreading in the SCS. Others suggested that only a minor amount of extension associated with the SCS spreading center may have been transferred to the Ailao Shan-Red River fault (Rangin et al., 1995; Morley, 2002; Clift et al., 2008). The initiation of regional rifting in East Asia during the Mesozoic occurred before the India-Eurasia collision (Fig. **F3D**) and is thought to be associated with subduction of the paleo-Pacific plate (Taylor and Hayes, 1980, 1983; Shi and Li, 2012).

Some hypotheses require the existence of a proto-SCS oceanic basin (Haile, 1973; Madon et al., 2000) that was once connected to the Pacific plate and began to close

around 44 Ma (e.g., Hall, 1996, 2002) in order to drive and accommodate the opening of the SCS (Fig. F3B). A large part of this proto-SCS may have been subducted into or uplifted as island arcs formed to the south in Borneo/Sabah and Palawan (Hall, 2002; Hutchinson, 1996, 2004), where remnants of the proto-SCS oceanic crust may be present (Hutchinson, 2005) and are one possible origin of the ophiolites of South Palawan (Rangin et al., 1990; Tu et al., 1992; Schlüter et al., 1996; Pubellier et al., 2004; Cullen, 2010). Slab-pull force from this subducting proto-SCS plate and a hypothesized in situ mantle plume may also have triggered or contributed to the opening of the SCS.

The opening of the SCS reveals complex patterns of continental breakup and seafloor spreading. Magnetic and seismic data suggest that the SCS Basin can be divided into five magnetically distinct zones (Li et al., 2008b) (Zones A–E in Fig. F4). In particular, magnetic amplitudes and orientations in the Southwest Subbasin (Zone E) differ markedly from those in the East Subbasin (Zone D). These two subbasins are divided by a complex set of transform faults forming the Zhongnan fault zone (Figs. F2, F4) (Yao, 1995; Jin et al., 2002; Li et al., 2007b, 2008b). This magnetic contrast may support an episodic seafloor-spreading model (Ru and Pigott, 1986) or may be attributed to the different tectonic contexts within which the two subbasins evolved. Pautot et al. (1986) suggested that the youngest part of the East Subbasin in Zone D developed within an older, preexisting oceanic crust, whereas the Southwest Subbasin in Zone E resulted from continental rifting. Within the East Subbasin, two distinct conjugate magnetic anomalies (M1 and M2 in Fig. F4) are thought to be the same age (anomaly 8 in Taylor and Hayes [1983] and Briais et al. [1993] models) and further divide the subbasin into a central part with high magnetic amplitudes and two separated parts with slightly weaker magnetization (Zones C1 and C1') near the two conjugate continental margins. The magnetic pattern of the Northwest Subbasin also differs from its adjacent segment in the East Subbasin.

Additional important contrasts exist between the East and Southwest Subbasins. For example, the greater average water depths of the Southwest Subbasin compared to the East Subbasin have been interpreted to imply relatively older crustal ages (Ru and Pigott, 1986; Yao et al., 1994; Li et al., 2008b), which conflict with younger ages inferred from the higher heat flow and shallower Curie-point depths of the Southwest Subbasin (Ru and Pigott, 1986; Li et al., 2010). Recent heating from magmatic activity could have contributed to the high heat flow in the Southwest Subbasin (Ru and Pigott, 1986; Li and Song, 2012), but this hypothesis needs to be tested through drilling.

A number of Cenozoic tectonic models have been proposed, but it remains uncertain as to whether the SCS Basin experienced a single episode or multiple episodes of extension and seafloor spreading and, if multiple episodes, in what sequence the subbasins evolved (e.g., Taylor and Hayes, 1980; Pautot et al., 1986; Ru and Pigott, 1986; Briais et al., 1993; Yao et al., 1994; Hayes and Nissen, 2005; Li et al., 2007b, 2008b). For example, the opening of the East and Northwest Subbasins may have predated or been synchronous with that of the Southwest Subbasin (Fig. F5A) (Taylor and Hayes, 1983; Briais et al., 1993; Lee and Lawver, 1995; Tongkul, 1994; Honza, 1995; Zhou et al., 1995; Schlüter et al., 1996; Hall, 2002; Hall and Morley, 2004; Hayes and Nissen, 2005; Braitenberg et al., 2006; Sun et al., 2009). This model contrasts with others in which an earlier opening of the Southwest Subbasin is preferred (Fig. F5B) (e.g., Ru and Pigott, 1986; Yao et al., 1994; Li et al., 2007b). This latter group of models considers the sharp contrasts between the East and Southwest Subbasins and the important role of the Zhongnan fault (Figs. F2, F4). There are also two models of slow propagation of the SCS spreading center, one with opening gradually propagating toward the northeast and the Taiwan Strait (Chung et al., 1994) and the other toward the Southwest Subbasin (Zhou et al., 1995).

## Previous drilling

Five sites were drilled in the peripheral continental slope of the SCS during Ocean Drilling Program (ODP) Leg 184 (Feb–April 1999; Wang, Prell, Blum, et al., 2000). The major objectives of Leg 184 were to study the variability of East Asian monsoonal climates (including millennial- to possibly centennial-, orbital-, and tectonic-scale variability) from cored late Cenozoic hemipelagic sediment. All Leg 184 sites are located on the continental slope, and none penetrated into igneous basement rock. The deepest hole cored during the leg reached 861 meters below seafloor (mbsf) at Site 1148 in 3294 m of water (Figs. F2, F4), with the oldest sediment recovered of early Oligocene age. The records from both Leg 184 and Expedition 349 will be used to establish links between the East Asian and Indian monsoons and to evaluate mechanisms of internal (climate system feedbacks) and external (orbital and tectonic) climate forcing.

## Seismic studies and site survey data

Figure F2 shows the sites drilled during Expedition 349 and available multichannel seismic (MCS) lines crossing those sites. Most drill sites are located at the intersection of two MCS lines; however, Sites U1434 and U1435 are not located on crossing points

but were interpreted to have only thin sedimentary cover above the igneous basement.

A dense 2-D MCS grid exists in the northern SCS continental margin and the northern part of the central SCS Basin. The Chinese National Offshore Oil Corporation (CNOOC) recently acquired most of these high-quality data. The northeastern part of the SCS has also been well studied and imaged with numerous geophysical surveys during Cruises SCSIO87, 973GMGS, ACT, TAICRUST, ORI645, and ORI689. More recent geophysical studies include the Taiwan Integrated Geodynamics Research (TAIGER) project (McIntosh et al., 2012) and surveys for gas hydrates.

Guangzhou Marine Geological Survey (GMGS) has undertaken extensive geophysical and geological mapping of a large portion of the central SCS Basin in recent years. As a result, MCS data and shallow sediment cores are regularly added to our existing site survey database. This mapping activity has already started producing 2-D seismic grids around our drill sites. Other MCS and magnetic data were collected near the drill sites by the R/Vs *Vema*, *Conrad*, and *Haiyang IV* (Taylor and Hayes, 1980, 1983; Yao et al., 1994; Hayes et al., 1995) (Fig. F2). Two stages of Sino-US cooperation in the early 1980s added more dense geophysical data coverage, which includes sonobuoy measurements, two-ship expanding spread profiles, and piston cores (Taylor and Hayes, 1983; Yao et al., 1994; Hayes et al., 1995). The German R/V *Sonne* carried out five cruises in 1987 (SO-49 and SO-50B), 1990 (SO-72A), 1994 (SO-95), and 2008 (SO-197) (Franke et al., 2011), and collected >10,000 km of MCS data and high-resolution echograms (Lüdmann and Wong, 1999; Lüdmann et al., 2001).

Swath bathymetry data are available for the entire SCS Basin from GMGS and the 2nd Institute of Oceanography of the State Oceanic Administration of China (Li et al., 2011). Magnetic anomalies covering all proposed drill sites were compiled by the Geological Survey of Japan and Coordinating Committee for Coastal and Offshore Geoscience Programs in East and Southeast Asia (CCOP) in 1996 (Ishihara and Kishimoto, 1996) (Fig. F4). This compilation offers remarkable coverage and accuracy and yields new insights into the dynamic opening process of the SCS (Li et al., 2008b, 2010; Li and Song, 2012).

A number of ocean bottom seismometer (OBS) studies have been carried out since 2000 (e.g., Yan et al., 2001; Zhang et al., 2013). The South China Sea Deep (SCSD) major research program of the National Science Foundation of China has funded coincident seismic refraction/reflection surveys, local active source 3-D OBS surveys, the

first regional passive source OBS survey, and the first deep-tow magnetic survey (Wang, 2012). Both deep-towed and surface-towed magnetic survey lines were designed to traverse the primary sites, allowing the establishment of the best possible magnetic anomaly model and calibrated age model of the ocean crust of the entire basin. The supporting site survey data for Expedition 349 are archived at the [Integrated Ocean Drilling Program Site Survey Data Bank](#).

## Scientific objectives

Expedition 349 focuses on coring into igneous basement at multiple sites in the SCS Basin to better understand seafloor spreading, ocean crust accretion, and mantle evolution. In addition, coring the sedimentary sections above basement will allow examination of the sedimentary and paleoceanographic responses to basin opening and eventual subduction along the Manila Trench.

- 1. Date the timing of the opening of different subbasins of the SCS and correlate the ages from magnetic anomalies to biostratigraphic, magnetostratigraphic, and radiometric ages.*

Magnetostratigraphy, biostratigraphy, and radiometric dating are the three principal techniques that will be used for chronostratigraphic analysis of the recovered sequences. Age control in the sedimentary section will be made from routine microfossil analyses, paleomagnetism, and isotope analysis. The age sequences can also be constrained by correlating seismic reflections to different drill sites. Because drilling at all expedition sites intends to recover the oldest sediment deposited directly on the top of oceanic basement, paleontological analyses will provide a minimum age constraint for the basement. Except for the upper ~900 m at Site U1432 in the primary operations plan, we plan to core all intervals within the three primary sites, with micropaleontological analyses conducted on all core catcher material and additional samples from split-core sections to refine the biostratigraphy, as time permits. Calcareous microfossils, including nannofossils and foraminifers, should be abundant in the carbonate successions at all sites. Within some intervals, particularly in the Neogene, we expect to find well-preserved and abundant siliceous microfossils (biogenic silica dominated by diatoms and radiolarians) that can provide additional biostratigraphic control.

Basement volcanic rock will be dated with  $^{40}\text{Ar}/^{39}\text{Ar}$  (Koppers et al., 2011) and possibly other high-resolution zircon dating techniques with uranium-series isotopes (Goldstein et al., 1991, 1994; Goldstein, 1995; Schwartz et al., 2005). Ocean crust rock

typically is very low in K concentrations and therefore more vulnerable to disturbances by submarine alteration. To ensure high-quality  $^{40}\text{Ar}/^{39}\text{Ar}$  dating on basement samples collected in the SCS, we will (1) carefully select fresh highly crystalline groundmass and plagioclase phenocrysts, which are the most suitable for  $^{40}\text{Ar}/^{39}\text{Ar}$  dating and (2) apply extended acid leaching procedures to remove altered portions of the groundmass or mineral separates (Koppers et al., 2011).

The half-spreading rates of the SCS are slow to intermediate, between 20 and 40 mm/y (Briais et al., 1993; Song and Li, 2012). Near the continent/ocean boundary, where Sites U1432 and U1435 are located, hyperextended crust exhuming possible lower crust and upper mantle could exist (Franke et al., 2011). If so, gabbro with late-stage minerals or felsic lithologies could be available for uranium-lead zircon dating using sensitive high-resolution ion microprobe reverse geometry (SHRIMP-RG), as well as for  $^{40}\text{Ar}/^{39}\text{Ar}$  dating of plagioclase, biotite, and/or hornblende mineral separates. A newly developed method that detects tiny amounts of uranium-bearing minerals, such as zircon, in rocks could reliably date the age of ocean crust (Schwartz et al., 2005; Grimes et al., 2007).

*2. Measure the magnetization, mineralization, and geochemical compositions of basement rocks to understand the causes of the sharp magnetic contrast between different subbasins.*

Magnetic susceptibilities of extrusive basalt normally decrease with increasing degree of alteration, which reduces their titanomagnetite content (e.g., Bleil and Petersen, 1983). Serpentinization of peridotite at deeper depths is also known to smear surface magnetic anomalies (e.g., Dymant et al., 1997). Detailed mineralogical studies are essential to understand these processes that may cause the magnetic contrast between the East and the Southwest Subbasins. Because of the complex patterns of magnetic anomalies in the SCS, careful measurements of magnetic susceptibility are needed to constrain models of, for example, tectonic settings or spreading rates (Dymant and Arkani-Hamed, 1995) that can explain the distinct differences in magnetic patterns between different subbasins, as well as their crustal affinities. Magnetization measurements from cores are also vital for creation of an initial model for predicting magnetic anomaly strength, in order to better understand the observed magnetic anomalies.

*3. Evaluate the origin and source evolution of SCS basement rock to understand the formation of SCS oceanic crust and the deep mantle processes driving crustal formation.*

Trace element chemical analyses and measurement of Sr, Nd, and Pb isotopic ratios will provide insights into the material influx and deep crustal and mantle processes

(Castillo et al., 1991; Tejada et al., 2004). The opening mechanism of the SCS can be constrained by investigating the variation in these geochemical tracers in the igneous basement rock. The basaltic rock cored during this expedition could have three potential mantle sources: (1) Indian Ocean/Eurasian lithospheric mantle, (2) Pacific mantle, or (3) a putative mantle plume.

All of these sources have distinctive geochemical characteristics in their incompatible trace element and long-lived radiogenic isotope ratios, which are not affected by variations in degree of partial melting of the mantle and fractional crystallization of the resultant melt. Therefore, based on the Expedition 349 drilling transect, we should be able to test several geochemical evolution scenarios corresponding to the rifting and spreading models of the SCS, including (1) continental rifting leading to seafloor spreading (due to Indochina extrusion tectonism or slab pull with southward subduction under Borneo), (2) subduction-induced back-arc spreading, and (3) plume-initiated rifting.

*4. Evaluate the paleoceanographic and climatic responses to the opening of the SCS and develop a 3-D sedimentation and subsidence model.*

Because our drill sites are located in different parts of the SCS, we can build a detailed 3-D postspreading model of seismic stratigraphy that will offer invaluable insights into deepwater sedimentary processes and how they evolved through time. This sedimentary model will be coupled with paleoenvironmental and paleoceanographic data from analyses of sediment cores to detect major geological events. Information on sedimentation rates, provenance, water depths, tectonic subsidence, and facies changes will be determined and will be correlated to known tectonic and climatic events. By core-log-seismic integration, we can build detailed 3-D sedimentation models. Major unconformities and boundaries found in the different subbasins will be correlated with those in the continental slopes and rifting basins to trace the dynamic transitional process from rifting to spreading, and also constrain critical paleoceanographic and tectonic changes during opening of the SCS.

Mineralogical and geochemical analyses will help identify sediment provenance in the SCS and how it has evolved through time. Analyses of detrital zircon in the sediment, for example, can (1) determine the maximum age of stratigraphic successions and lead to a better understanding of the source-to-sink processes, (2) determine provenance characteristics such as age and composition, (3) test regional paleogeographic models via provenance analysis, and (4) unravel facets of geological history locked in the mineral chemistry of detrital zircon (Fedo et al., 2003).

Structural analyses of core samples will focus on deformation features such as fractures, faults, veins, deformation bands, etc. Postcruise statistical analyses on these structural features will help reveal the regional stress field and its changes through time. Together with geophysical downhole logging and other data, the structural features recorded in cores could reveal regional SCS magmatic and tectonic events, as well as local rock deformation and stress heterogeneities.

*5. Obtain downhole geophysical logs to reveal physical properties of the sediments and the top oceanic basement and to provide a record of unrecovered intervals.*

Our proposed deployment of a minimum of two wireline logging tool strings (the standard triple combination [triple combo] and the Formation MicroScanner [FMS]-sonic) will measure a wide spectrum of geophysical properties and will provide structural, mineralogical, and geochemical information of the penetrated sequences. These data will be particularly important for unrecovered intervals that typically occur when using the extended core barrel (XCB) and rotary core barrel (RCB).

The triple combo tool string records geophysical signals of the penetrated sediment and basement rock by measuring the total and spectral natural gamma radiation (NGR), density, porosity, and resistivity of the formation. Gamma ray data will be used to infer lithology and provenance. Porosity, sonic, and density logs will be critical for decompaction and backstripping analyses and for constraining tectonic subsidence. The subsidence and rifting parameters so obtained can offer new insights on the episodic opening history of the SCS and reveal mantle properties.

Wireline logs will provide a continuous record to aid in the detection of lava flow boundaries, interlayered sediment, and alteration zones in the basement to evaluate the dip of lava flows. The number of lava flow units penetrated has implications for how well geomagnetic secular variation has been sampled and hence the extent to which paleolatitudes can be most precisely constrained.

With FMS-sonic logging, we will obtain high-resolution quasi-2-D images (electrofacies) of the borehole wall to reveal the structure and orientation of the rock. These data will provide constraints on volcanostratigraphy and crustal accretion processes (e.g., Tominaga et al., 2009). The high-resolution FMS images will help to detect small-scale fractures and lithologic variations, evaluate the dips of lava flows, and reorient core pieces. The General Purpose Inclinator Tool, which includes both a three-axis inclinometer and a three-axis magnetometer, will be used to measure changes in magnetic properties of lithologies and in paleomagnetic direction.

## Drilling and coring strategy

Our proposed operations plan for this expedition consisted of drilling three sites into basement (proposed Sites SCS-3G [U1431], SCS-6A [U1432], and SCS-4B [U1433]). Because of the predicted depth to basement at these sites (865–1830 mbsf) and to maximize our operational time, we requested and received approval from the Environmental Protection and Safety Panel and the Texas A&M Safety Panel to drill down through the uppermost ~900 m at the second site (U1432), provided that we encountered nothing unexpected at the first site (U1431), which was tied seismically to the second one. Even with this drill-down approval, it was unlikely that we would have sufficient time in the schedule to reach basement at all three of our primary sites unless operations proceeded better than predicted in the operations plan. With these issues in mind, we identified 10 alternate sites in the vicinity of our primary sites that required shallower penetration depths to reach basement. Three additional alternate sites in other locations targeted secondary objectives that could be addressed if for any reason we were unable to drill in the vicinity of one of our primary sites (Li et al., 2013).

Alternate sites with shallower penetration depths to basement were also important because coring at deeper depths is challenging. Hole stability is always a risk during coring and logging operations, and the longer the open-hole section, the higher the risk. Hole cleaning is also more difficult in deeper sections, particularly when coring dense basement material. We planned a reentry system to 900 mbsf for the deepest site (U1432; predicted total depth of 1930 mbsf) to help mitigate these issues. Given the relatively shallower total depths planned at the other two primary sites (U1431 and U1433), we felt that we could achieve the objectives without the aid of a reentry system. The reentry system at the deep site would serve two main purposes. First it would stabilize the upper portion of the hole, where unconsolidated sediment is more likely to cause hole stability problems. It also would provide a smaller annulus for hole cleaning, which increases annular velocity without having to significantly increase pump rates to remove dense basement cuttings from the hole. Higher flow rates generally result in washed-out sections in parts of the hole and can lead to stability issues. For the other primary sites, we planned to deploy a free-fall funnel to decrease the amount of time required to reach the basement objective.

This strategy of having multiple alternate sites approved for drilling prior to the start of the expedition proved to be valuable during this expedition. While installing the reentry system in Hole U1432B, we discovered that two of the three fiber optic cables

within the subsea camera wireline had failed. During a subsequent deployment, the camera system failed and we initially suspected that the final fiber optic cable had broken. Fortunately, the failure was related to the pan and tilt unit of the camera, so that after the problematic unit was removed the system worked again. This failure prompted discussions of alternate plans to meet the expedition objectives without the ability to perform reentries. During cementing of the final (10<sup>3</sup>/<sub>4</sub> inch) casing string in Hole U1432B, the pipe became stuck in the cement and ultimately forced us to abandon the hole. There was not enough time left in the expedition schedule to try another approach to reach the basement objective at that site; however, we were able to use the remaining time to reach basement at our primary site in the Southwest Subbasin (Site U1433). Additionally we were able to core at two alternate sites, proposed Sites SCS-4E (U1434) and SCS-6C (U1435). The latter site was thought to be a basement high very near the continent/ocean boundary (Fig. F6) with very thin (~10 m) sediment cover, whereas Site U1434 formed a short sampling transect with Site U1433, with Site U1434 located closer to the relict spreading center and also adjacent to a large seamount (Fig. F7).

## Site summaries

### Site U1431

#### Background and objectives

Site U1431 (proposed Site SCS-3G) is located near the relict spreading ridge where the youngest crustal magnetic anomalies are observed in the East Subbasin of the SCS (Figs. F4, F8). A positive magnetic anomaly that runs through this site allows regional correlation of crustal ages. This site is also surrounded by abyssal highs in the ocean crust, as well as younger seamounts (Figs. F6, F8B) whose volcanic and/or redepositional events may be recorded by sediments recovered from this site.

The primary objective at Site U1431 was to core into the oceanic basement to determine the age at which seafloor spreading ceased in the East Subbasin. The ~900 m thick package of sediment overlying basement also provides important constraints on the evolution of the ridge and associated late-stage magmatism, deep-marine sedimentary processes, and the paleoceanographic history following the termination of spreading in the SCS. Additionally, coring at this site will allow correlation of biostratigraphic, magnetostratigraphic, and radiometric ages to the observed crustal magnetic anomalies. Physical property and paleomagnetism measurements of base-

ment rock will help to elucidate the cause of the distinct contrasts in the nature of oceanic crust magnetic anomalies of the East and Southwest Subbasins. Furthermore, this site will provide constraints on mantle source, melting, and magmatic processes in the latest stages of basin formation. Physical property measurements of core samples and wireline logging measurements will provide stratigraphic information for correlation with regional seismic profiles. Microbiological sampling will explore the deep biosphere in the SCS to examine how sharp changes in lithology (interfaces) may affect subsurface community structure and function, as well as how posteruption processes might have influenced past ecosystems in the SCS.

## Operations

After a 463 nmi transit from Hong Kong averaging 11.0 kt, the vessel stabilized over Site U1431 at 0640 h (UTC + 8 h) on 31 January 2014. We cored five holes at Site U1431 (Table T1). The original operations plan called for one hole to a depth of ~1061 mbsf, which included ~100 m of basement. The plan was modified during transit to include two additional short holes for high-resolution sampling of the upper ~20 m of section. Hole U1431A was successfully cored to 28.4 mbsf and Hole U1431B to 17.0 mbsf. After the first core from Hole U1431C retrieved a split core liner and no mudline, we opted to abandon the hole, which was completed to a depth of 14.2 mbsf, and spudded Hole U1431D. Hole U1431D was cored to 617.0 mbsf when the XCB failed, leaving the cutting shoe, core catcher sub assembly, and breakoff sub in the hole. We abandoned Hole U1431D and switched to the RCB to spud Hole U1431E, which was drilled to 507.0 mbsf, spot cored, and then cored continuously from 575.0 mbsf to total depth at 1008.8 mbsf in igneous basement. After conditioning the hole for logging, two logging runs were performed. The triple combo tool string was run to 463.0 m wireline depth below seafloor (WSF), and the FMS-sonic tool string was run to 444 m WSF with two passes. Total time spent at Site U1431 was 385.7 h (16.1 days).

A total of 122 cores were collected at this site. The advanced piston corer (APC) was deployed 26 times, recovering 225.61 m of core over 228.50 m of penetration (98.7% recovery). The XCB was deployed 48 times, recovering 236.50 m of core over 448.10 m (52.8% recovery). The RCB was deployed 48 times, recovering 243.00 m of core over 443.5 m of penetration (54.8% recovery).

## Principal results

The cored section at Site U1431 is divided into 11 lithostratigraphic units, 9 sedimentary and 2 igneous, based mainly on a combination of data from Holes U1431D and U1431E (Fig. F9). Lithostratigraphic Unit I is a 101.16 m thick Pleistocene sequence of dark greenish gray clay and silty clay. Graded silt intervals are abundant and interpreted as turbidites. Discrete volcanic ash layers that are either mafic or felsic in composition and 0.5–5 cm thick occur throughout the unit. This unit is underlain by Unit II (Pliocene–Pleistocene age), which is divided into Subunits IIA (101.16–194.95 mbsf) and IIB (194.95–267.82 mbsf). The 166.66 m of Unit II is dominated by dark greenish gray clay with fewer volcanic tephra layers than Unit I. Subunit IIA is characterized by the presence of clay with nannofossils and calcareous turbidites, which are not found in Subunit IIB. Rare, thin silt turbidites are largely limited to Subunit IIB. Unit III (267.82–326.12 mbsf) is a 58.30 m thick upper Miocene to Pliocene sequence of dark greenish gray clay with modest amounts of interbedded calcareous turbidites. These graded turbidites typically have sandy foraminifer-rich intervals at the base and are interpreted to represent mass wasting events from neighboring seamounts. Unit IV (326.12–412.42 mbsf) is an upper Miocene unit comprising 86.30 m of dark greenish gray clay and silty clay with minor amounts of silt and fine sand interbeds interpreted as turbidites. This unit is much reduced in carbonate content compared to overlying Unit III. Unit V (412.42–603.42 mbsf) is a 191 m thick sequence of upper Miocene dark greenish gray silty sand and interbedded clay with nannofossil ooze. Recovery is low throughout the section, but sandy core catcher samples suggest that many of the unrecovered intervals may consist of sand.

Unit VI (603.42–797.30 mbsf) is readily distinguished from the overlying units by the abundance of greenish black volcanoclastic breccia and sandstone interbedded with minor amounts of claystone. This unit is 193.88 m thick and dated to the late Miocene. The clasts in this breccia are primarily composed of highly vesicular aphanitic basalt and scoria, nonvesicular to sparsely vesicular basalt, basaltic glass shards, and lesser amounts of pumice and mudstone. Major element data indicate that these clasts are characteristic of ocean island basalt (OIB). The breccia beds are typically massive and have erosive bases, indicative of deposition by mass wasting either as debris or grain flows. Based on the composition of the clasts and abundant magmatic mineral fragments, these deposits are likely sourced from the nearby seamounts. Unit VII (797.30–885.25 mbsf), 87.95 m thick and middle to late Miocene in age, is composed of interbedded dark greenish gray sandstone with lesser amounts of siltstone and claystone in a turbidite sequence. It is essentially a less coarse grained equivalent

to Unit VI and coarsens uphole through the unit. Unit VIII (885.25–889.88 mbsf) is a 4.63 m thick middle Miocene sequence of massive, dark olive-brown claystone that directly overlies the basalt of Unit IX (889.88–962.51 mbsf). The mudstone represents deep-marine sedimentation. Unit X (962.51–972.00 mbsf) is a 9.49 m thick sequence of lower Miocene yellowish brown claystone and claystone breccia that lies within the volcanic sequence. This unit is underlain by the basalt of Unit XI (972.00–1007.89 mbsf).

Calcareous nannofossils, planktonic foraminifers, and radiolarians recovered at Site U1431 are typical of low-latitude assemblages, characterized by species widely found in the tropical western Pacific region. Calcareous nannofossils are generally poorly preserved and frequent or common in Units I–IV but rare or absent downhole. Planktonic foraminifers are also poorly preserved and vary from frequent to rare in Units I–IV but are absent more frequently in samples from deeper units. Radiolarians are common and well preserved in samples from the uppermost 30 m, absent from 30 to 870 mbsf, and present but poorly preserved in Units VIII and X.

The biostratigraphy of Site U1431 is based on analysis of calcareous nannofossil, planktonic foraminifer, and radiolarian assemblages in all core catcher samples and additional samples from within cores from Holes U1431D and U1431E. The sedimentary succession recovered at Site U1431 spans the lower Miocene through Pleistocene (Fig. F10). Sediment from Units I–VIII is assigned to middle Miocene to Pleistocene calcareous nannofossil Zones NN6–NN21 and planktonic foraminifer Zones M9–Pt1, with no obvious hiatuses. The Pliocene/Pleistocene boundary is located between Cores 349-U1431D-15H and 18H, and the Miocene/Pliocene boundary is located between Cores 31X and 33X. Biostratigraphic control for the upper Miocene section is hampered by a paucity of nannofossils and planktonic foraminifers and poor core recovery in Units IV and V, which are dominated by turbidites. Nevertheless, the middle/late Miocene boundary is placed between Cores 349-U1431E-27R and 33R. In situ calcareous microfossils are absent from the claystones of Unit X; however, radiolarian biostratigraphy indicates that the rock is early Miocene in age (~16.7–17.5 Ma), corresponding to radiolarian Zone RN4. Sedimentation rates varied from ~8 cm/k.y. in the middle to early late Miocene, ~14 cm/k.y. for the remainder of the late Miocene, to ~5 cm/k.y. in the Pliocene–Pleistocene. Extremely low sedimentation rates (<2 cm/k.y.) occurred in the early to earliest middle Miocene during deposition of the claystones of Units VIII and X (Fig. F10).

The basalt of Unit IX was encountered at ~890 mbsf in Hole U1431E. Coring continued to ~1008 mbsf, recovering basement basalt separated by an interflow claystone between 3.7 and 9.5 m thick at 962.3 mbsf. In total, 46.2 m of basalt was recovered over a cored interval of 108.4 m, yielding an average recovery of 42.6%. The basalt is divided into 13 igneous lithologic units (Fig. F11) and is mainly composed of massive lava flows (six in Unit IX and two in Unit XI) as thick as ~26.7 m, with limited evidence for pillow basalt flows in between. Because no contacts between flow units were recovered, boundary locations and unit thickness estimates are approximate. The interpretation of igneous lithologic Units 1, 7–10, and 12 as pillow basalts is uncertain and is based on scarce evidence, such as the presence of glassy (curved) chilled margins, ropy flow structure, and a single occurrence of a hyaloclastite breccia.

Most basalt at Site U1431 is aphyric and ranges in grain size from microcrystalline to fine grained, with the groundmass grain size getting coarser (0.7–1 mm) in the cores of the thickest massive lava flows. All basalt has a phase assemblage of plagioclase and clinopyroxene ( $\pm$  olivine) in its groundmass, with 0.1–0.5 mm subhedral-euhedral olivine microphenocrysts present in some igneous lithologic units, resembling a typical mid-ocean-ridge basalt (MORB) crystallization history and, in conjunction with geochemical evidence, indicates that basalt recovered at Site U1431 is representative of typical MORB.

The alteration style of basalt at Site U1431 is typical of MORB. Alteration color is dominated by gray to dark gray-green and yellow to red-brown. Typical secondary minerals include saponite, Fe oxides, carbonate, and celadonite, which represent alteration assemblages at low temperature. Alteration intensity varies from slight to complete, but the majority of the recovered basement rock is moderately altered. There is no systematic change in the alteration nature (e.g., alteration color) with depth that might indicate a transition from more oxidizing to reducing conditions. The strongest alteration occurs in halos flanking veins, which overprints the background pervasive alteration, indicating that the overall distribution of alteration was controlled by fractures and vein structures. Most lithologic basement units include intervals with slight alteration, preserving remarkably fresh olivine crystals that show only limited alteration along their rims and “maschen” fractures.

Fractures and veins occur throughout the basalt in Hole U1431E. These features are randomly oriented, with no obvious offset or thickness variation. A fracture with ~1 cm of normal offset occurs in the interflow claystone of Unit X. The basalt fractures likely formed during cooling of the lava, whereas the fractures in the interflow clay-

stone may suggest slight movement as the lava of Unit IX flowed over it. The major veins are white or reddish brown and filled with carbonate and iron oxides. Arched veins generally occur in sets, often in combination with linear veins, forming a vein network consistent with fractures formed during cooling.

Geochemistry measurements at Site U1431 aimed to characterize the interstitial water chemistry, total organic carbon (TOC), bulk carbonate content, and igneous basement rock. The depth profiles of major elements and nutrients indicate that organic matter diagenesis, biogenic carbonate dissolution and recrystallization, and volcanic ash alteration occurred in the sediment. The interstitial water never reaches complete sulfate reduction in Hole U1431D, with minimum concentrations of ~2.3 mM occurring from ~170 to 260 mbsf. This is consistent with the very low methane concentrations, which range from 1.6 to 4.8 ppmv. Sulfate concentrations gradually increase below 260 mbsf, reaching 24.0 mM at the bottom of Hole U1431D (~600 mbsf). Shore-based isotopic analysis of these interstitial water samples should constrain the source of the sulfate-bearing fluid in Hole U1431D.

Bulk carbonate content varies with depth, ranging from 0 to 47 wt% in Hole U1431D and from 0 to 57 wt% in Hole U1431E. The discrete intervals with higher carbonate content in Hole U1431D correspond to nannofossil ooze beds, whereas in Hole U1431E higher carbonate content is associated with diagenetic carbonate concretions visible in the cores. TOC varies from 0 to 4.7 wt% in Hole U1431D, whereas in Hole U1431E, TOC is lower and ranges from 0 to 0.74 wt%. The TOC to total nitrogen (C/N) ratio is generally <4 at Site U1431, indicating that TOC is derived from a marine source; however, C/N ratios range from 8 to 12 in some intervals of lithostratigraphic Units III and IV in Hole U1431D, which could indicate a mixture of marine and terrestrial organic matter sources.

Major and minor element concentrations measured by inductively coupled plasma-atomic emission spectroscopy (ICP-AES) on Hole U1431D sediment indicate that it is most likely derived from an intermediate igneous source. The basalt recovered from below ~890 mbsf in Hole U1431E has moderately high loss on ignition (LOI) values (0.46–2.85 wt%), but low K<sub>2</sub>O (≤0.53 wt%) and TiO<sub>2</sub> (1.01–1.77 wt%). The basalt samples of Unit IX contain higher MgO, FeO, and Ni concentrations than those of Unit XI, likely because of olivine accumulation. The basalt major element composition is similar to that of mid-ocean-ridge tholeiite, whereas clasts from the volcanoclastic breccia are alkali basalt with high K<sub>2</sub>O (1.08–2.67 wt%) and TiO<sub>2</sub> (2.10–3.13 wt%), probably sourced from the nearby seamounts (Figs. [F12](#), [F13](#)).

A total of 105 whole-round samples (5–10 cm long) were collected for microbiological studies from Site U1431. These samples were typically taken adjacent to interstitial water whole-round samples for comparison to interstitial water chemistry when possible. These samples will be analyzed for microbial content based on DNA and lipid properties of the cells present. Subsamples were prepared for fluorescent in situ hybridization and single cell genomics. DNA and lipid samples were preserved at  $-80^{\circ}\text{C}$ , whereas fluorescent in situ hybridization samples were preserved at  $-20^{\circ}\text{C}$ . Four basalt whole-round samples were selected for cultivation-based studies, with sampled material inoculated into a seawater-based medium containing olivine as a source of energy. An additional 76 samples were collected and prepared for investigation of the microbiology of interfaces using lipid and nucleic acid analyses. These samples were collected mostly in the upper 200 m of Hole U1431D from specific interfaces, including five ash/clay interfaces and ten turbidite/clay interfaces. Selection of these samples was dependent upon recognition of key intervals by the core description team and occurred through consultation between the microbiologists and sedimentologists or petrologists.

Microbiology contamination testing at Site U1431 included the use of perfluorocarbon tracers (PFTs), fluorescent microspheres, and fluid community tracers (FCTs). PFTs were added to the drilling fluid for all APC coring in Holes U1431B–U1431D, as well as for the first four XCB cores in Hole U1431D. Twelve samples were taken from six sediment cores collected over this interval to measure contamination with the PFTs. Microspheres were added to the core catcher before the core barrel was deployed in Hole U1431E over the interval from 651.8 to 952.6 mbsf. Two microsphere samples were collected from each core, one from scraping of the core surface and one as a subsample from the interior of each whole-round sample. In addition, FCT samples were collected from the drilling fluids on a daily basis (for a total of 14) to track the microbial communities typical of seawater and other drilling mud constituents. Microbial community DNA and lipids from these fluids will be compared to those measurements made on the core samples to determine if there are microbes that can be recognized as contaminant taxa.

Variations in the natural remanent magnetization (NRM) intensity at Site U1431 are generally correlated with lithology. Paleomagnetic measurements indicate that the silty clay and clayey silt in Unit I (0–101.16 mbsf) have a mean NRM intensity on the order of  $3 \times 10^{-2}$  A/m, whereas the clay with nannofossils in Unit II (101.16–267.82 mbsf) has somewhat higher NRM intensity ( $\sim 6 \times 10^{-2}$  A/m). Many discrete peaks of higher NRM values that appear in some depth intervals in both Units I and II can be

tied directly to the presence of volcanic ash layers. Magnetic susceptibility data also show positive peaks at these intervals. Overall, magnetic susceptibility and NRM intensity variations through the sedimentary units are closely correlated.

Magnetostratigraphic records at Site U1431 indicate the presence of several relatively well defined polarity intervals in the cores. Based on inclination and declination data, the Brunhes/Matuyama Chron boundary (0.781 Ma) is placed at ~46 mbsf in Hole U1431D (Fig. F10). The Matuyama Chron is defined between ~46 and ~135 mbsf. Below ~170 mbsf, the XCB cores are strongly overprinted by a drilling-induced remagnetization that cannot be removed by shipboard thermal demagnetization. The magnetic record improved in the RCB cores of Hole U1431E, allowing tentative correlation of certain parts of the magnetic polarity interval with the geomagnetic polarity timescale in conjunction with biostratigraphic constraints. In particular, the polarity shift from normal to reversed at ~716 mbsf may correspond to the Chron C5n/C5r boundary (11.056 Ma) (Fig. F10).

For basement rock units, the observed paleomagnetic signals cannot be directly linked to the geomagnetic polarity timescale yet because the basalts in lithostratigraphic Units IX and XI were erupted intermittently, and the pelagic clay sediment in lithostratigraphic Units VIII and X may represent a significant time interval. Nevertheless, reliable normal and reversed polarities occur within this interval, which indicates that the eruption of the basalt units may have spanned a significant amount of time on the order of a few thousand to one million years.

Whole-round cores from Holes U1431A–U1431C were measured for *P*-wave velocity, bulk density, magnetic susceptibility, and NGR. For Holes U1431D and U1431E, measurements were also made on whole-round cores, with additional measurements on split cores and discrete samples, including thermal conductivity, porosity, and bulk, dry, and grain densities. In general, the physical properties correlate with lithology, composition, and induration. In Hole U1431D, bulk density, *P*-wave velocity, shear strength, NGR, and thermal conductivity increase gradually with depth over the uppermost 150 mbsf (Fig. F9), whereas porosity measured on discrete samples decreases from 84% to 50% over the same depth range. This indicates that sediment compaction dominates the physical property variations above 150 mbsf. Volcanic ash layers in Unit I (e.g., at 25 and 100 mbsf) show relatively high magnetic susceptibility (300–500 SI) values. Below 150 mbsf, a decrease in shear strength may be associated with higher clay content. NGR counts are relatively high from the seafloor to 500 mbsf, which is consistent with the dominance of clay and silt in Units I–V.

Most physical properties show a significant change at ~550–600 mbsf, near the boundary between Units V and VI (Fig. F9). *P*-wave velocity and porosity increase, whereas NGR values and thermal conductivity are relatively low, a pattern consistent with the dominance of volcanoclastic breccia and sandstone in Unit VI. Layers with higher NGR counts and high magnetic susceptibility values occur at ~660 and ~710 mbsf. These do not correlate with the breccia but correspond to a silt- and/or sandstone probably enriched in magnetic minerals such as magnetite. The basalt units below 889.88 mbsf (Units IX and XI) display the lowest NGR, highest magnetic susceptibility, and largest bulk density values (Fig. F9). The interflow clay (Unit X) between the two basaltic units shows NGR values ~20 times larger than those of the basalt, as well as much lower magnetic susceptibility. Lower magnetic susceptibility and NGR values at the top of the basalt are consistent with higher but still moderate alteration in these basement units.

Two downhole logging tool strings were run in Hole U1431E, the triple combo (NGR, porosity, density, electrical resistivity, and magnetic susceptibility) and the FMS-sonic (NGR, sonic velocity, and electrical resistivity images) tool strings (Fig. F9). The triple combo tool string reached 464 m WSF before a bridge prevented access to the lower part of the borehole. The hole was wider than 17 inches below ~300 m WSF and showed closely spaced variations in borehole width above that depth. These were not ideal conditions for borehole log quality; however, stratigraphic changes are apparent in the NGR and magnetic susceptibility logs. The FMS-sonic tool string reached 444 m WSF, with two passes made above that depth. Downhole temperature measurements of the borehole fluid are consistent with the low geothermal gradient (~15°C/km) established from the advanced piston corer temperature tool (APCT-3) measurements taken on Cores 349-U1431D-4H, 7H, 10H, and 13H (Fig. F14).

## Site U1432

### Background and objectives

Site U1432 (proposed Site SCS-6A) is located ~60 km south of ODP Site 1148 (Wang, Prell, Blum, et al., 2000; Li et al., 2006; Wang and Li, 2009), just south of the northern continent/ocean boundary on the Chinese continental margin (Figs. F6, F8). This part of the basin shows the deepest basement and is likely the oldest among the sub-basins based on magnetic anomalies (Taylor and Hayes, 1980, 1983; Pautot et al., 1986; Briais et al., 1993) (Fig. F4). This site was designed to recover the oldest oceanic crust and the oldest sedimentary rock in the East Subbasin to test the hypothesis that

the onset of seafloor spreading in the SCS occurred here first at ~32 Ma. Magnetic anomaly 11, the oldest anomaly interpreted by Taylor and Hayes (1980) and Briais et al. (1993), passes near this site and hence would allow key calibration between ages estimated from magnetic anomalies and those from biostratigraphy, radiometric dating, and magnetostratigraphy.

The true nature of the continent–ocean transition and oceanic basement at this site is still speculative; there could be volcanic extrusions associated with early continental breakup and the onset of seafloor spreading, exhumed lower crustal materials from preferential lower crust extension, exhumed mantle materials, or even Mesozoic rock. Coring at this site was intended to help pinpoint the exact location and tectonic nature of the continent–ocean transition and address key problems in the early tectonic transition from rifting to drifting and associated paleoenvironmental changes, including

1. The age of basement (presumably the oldest oceanic crust) near the continent/ocean boundary;
2. Petrology and geochemistry of basement rock and their bearing on continental breakup, incipient seafloor spreading, and mantle evolution;
3. Physical properties of basement rock and their implications for interpreting sharp magnetic contrasts between different subbasins; and
4. Sedimentary, paleoceanographic, and ecosystem responses to the opening of the SCS.

As a result of operational challenges (see [“Operations”](#)), the objectives of sampling basement and basal sediment at Site U1432 were not achieved.

## Operations

After a 181 nmi transit from Site U1431 averaging 11.0 kt, the vessel stabilized over Site U1432 at 2337 h (UTC + 8 h) on 16 February 2014. Site U1432 consisted of three holes (Table [T1](#)). The first hole was a planned jet-in test to determine the correct casing depth for the 20 inch casing string. The second hole was to consist of a reentry system with three strings of casing to ~900 mbsf, followed by coring to ~1930 mbsf. Because of poor weather conditions, an additional hole was piston cored while waiting on suitable weather to continue the reentry installation.

Hole U1432A was successfully jetted to 62.0 mbsf. A reentry system was then successfully installed to 787.1 mbsf in Hole U1432B. The final cement job on the last casing

string compromised the reentry system when the drill string became stuck in the cement. The drill string had to be severed, forcing us to abandon Hole U1432B. Hole U1432C was successfully cored to 110.0 mbsf with the APC. Four downhole temperature measurements were taken in Hole U1432C with the APCT-3. A total of 12 APC cores were collected at this site, recovering 88.74 m of core over 110.0 m of penetration (81% recovery). The total time spent on Site U1432 was 492 h (17.9 days).

### Principal results

Hole U1432C consists of 12 cores (Cores 349-U1432C-1H through 12H) that penetrated to 110.0 mbsf. The lithology is dominated by a sequence of dark greenish gray clay and clay with silt, assigned to lithostratigraphic Unit I (Fig. F15). Clay layers are interbedded with very thin bedded (centimeter scale) or laminated silty layers. These layers mostly fine upward and have sharp erosive bases. These graded sequences are generally 10–20 cm thick and are interpreted as distal turbidites. A 2.4 m thick unconsolidated sand layer occurs in the middle of the drilled section. The sand and silt layers represent <5% of the total recovered core and can usually be identified using magnetic susceptibility measurements, as they typically exhibit lower values than the clays. Thin volcanic ash layers (0.5–2.0 cm thick) occur occasionally in some cores.

The age of the sedimentary sequence recovered in Hole U1432C is <0.91 Ma (Middle–Late Pleistocene) based on planktonic foraminifer and calcareous nannofossil biostratigraphy (Fig. F16). Radiolarians are abundant and moderately to poorly preserved in the upper 15 m of the hole but become progressively rarer and more poorly preserved downhole and comprise a Pleistocene–Holocene assemblage. Nannofossil preservation is moderate to good throughout the hole, with considerable reworking of Pliocene and Miocene species above ~50 mbsf. Preservation of planktonic foraminifers is also moderate to good, with evidence of moderate dissolution, as indicated by frequent fragmentation. Planktonic foraminifers are more dominant in sandy intervals that also contain reworked Pliocene species and shallow-water benthic foraminifers.

A total of 16 whole-round samples (5 cm in length) were taken for interstitial water measurements in Hole U1432C. Geochemical analysis shows that sulfate is completely consumed at ~90 mbsf, coincident with maximum methane concentrations between 4650 and 4750 ppmv just below this depth. The absence of higher hydrocarbons suggests that the methane is primarily microbial in origin. TOC in the hole varies from 0.34 to 0.99 wt%, whereas CaCO<sub>3</sub> concentrations are generally low (<12 wt%).

Five whole-round samples and five interface samples were collected from Hole U1432C for DNA and lipid analysis. The five whole-round samples were also used to inoculate several types of microbiological media to test whether autotrophic and heterotrophic microbes can be grown. For heterotrophic culture enrichments, glucose, acetate, fumarate, and formate were used as sources of carbon and energy. For autotrophic culture enrichments, sodium bicarbonate and hydrogen were used as sources of carbon and energy, respectively. We also collected and preserved 200 mL of drilling fluid for FCT analysis. The microbial communities present in these samples will be compared to those present on the inside and outside of the cores to determine whether microbes in the drilling fluid behave as suitable contaminant tracers.

As seen at Site U1431, the NRM of samples from Hole U1432C contains a vertical component generated by the drilling process, which is easily removed by 5–10 mT alternating field (AF) demagnetization. A polarity reversal at ~105 mbsf is defined as the Brunhes/Matuyama Chron boundary (0.781 Ma) (Fig. F16). In the Brunhes Chron, there are two directional anomaly intervals at ~10 mbsf and between 50 and 70 mbsf. These anomalies could represent authentic magnetic excursions or could be caused by postdepositional disturbances. These magnetostratigraphic results, when combined with the biostratigraphy, indicate a higher sedimentation rate (~13.5 cm/k.y.) in Hole U1432C (Fig. F16) than for the same age interval in Hole U1431D (~5.8 cm/k.y.), which is consistent with its location closer to the continental margin.

Physical property measurements made on whole-round core sections were smoothed using a five-point (10 cm) moving average and combined with discrete sample measurements. Bulk density, *P*-wave velocity, magnetic susceptibility, NGR, thermal conductivity, and shear strength decrease with depth in the uppermost 50 m of Hole U1432C (Fig. F15), showing an inverse relationship with porosity. Variations in these records are lower below 50 mbsf. This indicates that the compaction effect dominates the physical properties in the uppermost part of Hole U1432C. The 2.5 m thick sand layer near 50 mbsf is clearly delineated by low NGR, low magnetic susceptibility, and higher *P*-wave velocity (Fig. F15).

Four APCT-3 downhole temperature measurements on Cores 349-U1432C-5H, 7H, 9H, and 11H indicate a geothermal gradient of 85°C/km (Fig. F14). Combining these temperatures with thermal conductivity measurements made on the sediment cores, the preliminary heat flow value at Hole U1432C is 94 mW/m<sup>2</sup>. The geothermal gradient and heat flow values are similar to those at Site 1148, ~60 km to the north-northeast (Wang, Prell, Blum, et al., 2000) (Fig. F14).

## Site U1433

### Background and objectives

As a result of the marked contrast in magnetic anomaly amplitudes between the Southwest and East Subbasins of the South China Sea (Yao, 1995; Jin et al., 2002; Li et al., 2007, 2008), it is questionable whether rifting and drifting within these two subbasins occurred synchronously and how these subbasins evolved in comparison to the Northwest Subbasin. Site U1433 (proposed Site SCS-4B) is located in the Southwest Subbasin near the relict spreading center and magnetic anomaly C5d identified by Briais et al. (1993) (Figs. F4, F8). Together with Site U1431 in the East Subbasin, coring at Site U1433 should help to explain the sharp differences in magnetic amplitude between the East and Southwest Subbasins and test the hypothesis that in the Southwest Subbasin the breakup from continental rifting to seafloor spreading occurred more recently than in the East Subbasin (Pautot et al., 1986). Coring will help determine the age of this subbasin near the end of the spreading and correlate ages from magnetic anomalies with biostratigraphic, magnetostratigraphic, and radiometric ages. The apparent weak magnetization in basement rock (Li et al., 2008) will be examined through petrological and geochemical analyses and by measurements of magnetic susceptibility and remanent magnetization. The specific objectives at this site were to

1. Determine the termination age of spreading in the Southwest Subbasin and correlate it with ages of regional tectonic events;
2. Test the hypothesis that rifting and subsequent seafloor spreading in the Southwest Subbasin occurred later than that in the East Subbasin;
3. Measure magnetization, mineralization, and geochemical compositions of basement rocks to trace how the mantle evolved through time; and
4. Examine the paleoceanographic and sedimentary response to the opening of the South China Sea.

### Operations

After a 334 nmi transit from Site U1432 averaging 11.2 kt, the vessel stabilized over Site U1433 at 0230 h (UTC + 8 h) on 8 March 2014. The original operations plan consisted of drilling one hole to a depth of ~965 mbsf, which included 100 m of basement. This plan was modified during transit in order to eliminate the use of a free-fall funnel and the XCB by coring two holes (Table T1). Hole U1433A was cored using the APC to refusal at 188.3 mbsf. Hole U1433B was drilled to 186.1 mbsf and then cored

using the RCB. The sediment/basement interface was encountered at ~798.5 mbsf, and we advanced the hole by rotary coring into basement to a final depth of 858.5 mbsf. After conditioning the hole for logging, we deployed the modified triple combo tool string and the FMS-sonic tool string to 840 m WSF, with multiple passes made in the basement section of the hole with the latter tool.

A total of 94 cores were collected at this site. The APC was deployed 20 times, recovering 168.79 m of core over 188.3 m of penetration (89.6% recovery). The RCB system drilled one 186.1 m interval and collected 74 cores, recovering 443.04 m of core over 672.4 m of penetration (65.9% recovery). The overall recovery at Site U1433 was 71.1%. The total time spent on Site U1433 was 284.5 h (11.85 days).

## Principal results

The cored section at Site U1433 is divided into four lithostratigraphic units (three sedimentary and one igneous) based on a combination of data from Holes U1433A and U1433B (Fig. F17). Lithostratigraphic Unit I is a 244.15 m thick sequence of Pleistocene dark greenish gray clay, silty clay, and clay with nannofossils. The clay is interbedded with small volumes of generally thin, graded quartzose silt and nannofossil ooze, both interpreted to be turbidite deposits that comprise <5% of the unit. This unit is underlain by middle Miocene to Pleistocene Unit II (244.15–747.93 mbsf), which is divided into two subunits: IIA (244.15–551.32 mbsf) and IIB (551.32–747.93 mbsf). The entire unit is 503.78 m thick and dominated by dark greenish gray clay with frequent graded carbonate interbeds, largely comprising nannofossil ooze and chalk that are characterized by sharp, erosive bases and gradational, bioturbated tops. In Subunit IIB, carbonate beds are sometimes substantially thicker, up to several meters, rather than <1 m and usually <50 cm in Subunit IIA. The carbonates are turbidite deposits with evidence of re-sedimentation from shallow-water regions based on the occurrence of benthic foraminifers that dwell in the photic zone. The lowermost sedimentary sequence, Unit III (747.93–796.67 mbsf), is a 48.74 m thick lower to middle Miocene sequence of claystone and claystone with silt. Most of the unit is reddish brown or yellowish brown massive sediment with common burrowing stained black by diagenetic alteration. As in Units I and II, bioturbation of Unit III is consistent with sedimentation at lower bathyal to abyssal water depths (*Nereites* ichnofacies). Unit III contains sparse, relatively thin calcareous turbidites. There is no evidence for hydrothermal influence on sedimentation or diagenesis despite the fact that it lies directly above the basalt of Unit IV (796.67–857.48 mbsf). Unit III is the product of relatively slow sedimentation in a distal setting at the foot of a continental margin and is sim-

ilar to the basal sediment at Site U1431 and to “red clay” deposits from the central Pacific (Bryant and Bennett, 1988).

Analysis of calcareous nannofossils, planktonic foraminifers, and radiolarians in core catcher samples and additional samples from split cores indicates that the sedimentary succession recovered at Site U1433 spans the lower Miocene to the Pleistocene (Fig. F18). Age control for the lower to lower middle Miocene section is difficult because of very rare occurrences of microfossils in the brown claystone (Unit III) overlying the basement. Nannofossils in sediment preserved in and around basalt pillows are Oligocene to early Miocene in age, but additional postexpedition analyses are required to determine if these assemblages are reworked or in situ.

Calcareous nannofossils are generally common to abundant with good preservation in samples from the Pliocene–Pleistocene section but are rare and heavily overgrown or even barren in some upper Miocene and Pliocene samples, especially those from nannofossil ooze/chalk intervals. Planktonic foraminifers also show considerable variations in both abundance and preservation. They are abundant and well preserved in silty layers with numerous small (<150  $\mu\text{m}$ ) specimens but poorly preserved and very difficult to identify in lithified intervals. Radiolarians are abundant and well preserved in the Upper Pleistocene section in Hole U1433A, but rare or absent in older sediment sections downhole. In Hole U1433B, samples are barren of radiolarians until the brown claystone of Unit III, in which rare and poorly preserved but biostratigraphically significant specimens occur.

Integration of biohorizons and paleomagnetic datums indicates extremely low sedimentation rates (<0.5 cm/k.y.) during the early to middle Miocene. Sedimentation rates varied from ~5 to 9 cm/k.y. from the late Miocene to early Pleistocene, but then increased sharply to ~20 cm/k.y. since 1 Ma (Fig. F18).

We cored 60.81 m into igneous basement below 796.67 mbsf in Hole U1433B, recovering 29.02 m of basalt (47.7% recovery). This short basement succession was divided into 45 igneous lithologic units, which are grouped into lithostratigraphic Unit IV and are immediately overlain by hemipelagic dark reddish brown to yellowish brown claystone (Unit III) (Fig. F19). The basement at Site U1433 is composed of a 37.5 m thick succession of small pillow basalt lava flows in the top (Fig. F20), with a 23.3 m series of massive basalt lava flows toward the bottom.

The igneous basement begins with a sequence of sparsely to highly plagioclase-phyric pillow basalt with a trace of olivine microphenocrysts. Most of the pillow basalts are

nonvesicular to sparsely vesicular, range in grain size from crypto- to microcrystalline, and in many cases have well-preserved glassy chilled margins along both the upper and lower unit boundaries. A few larger lobate flows are present, with flow thicknesses varying from 0.1 to 1.1 m. In two intervals, interpillow hyaloclastite breccia was encountered, with remnants of baked limestone in which Oligocene to early Miocene nannofossils occur. In between these sequences of pillow basalt flows, one 5.2 m thick microcrystalline to fine-grained massive flow was encountered that is sparsely olivine-plagioclase-phyric but has a holocrystalline groundmass with abundant clinopyroxene present in the interstitial spaces. Downhole, the basement is characterized by more massive basalt lava flows as thick as ~12.8 m. These massive flows have similar petrologic characteristics and range from sparsely to highly plagioclase-phyric with minor microphenocrysts of olivine. Toward the interiors of the thickest lava flows the grain size increases to fine grained.

All basalts have a phenocryst phase assemblage of plagioclase  $\pm$  olivine, whereas the more massive flows also have clinopyroxene in their groundmass. This assemblage resembles a typical MORB crystallization assemblage and, in conjunction with geochemical evidence, we conclude that the basement basalt at Site U1433 is typical MORB.

Alteration is also typical of that of MORB. The basalt ranges from mostly fresh/less altered to moderately altered in intensity, typically as halos in association with cracks and veins, and from gray to dark gray-green and yellow to red-brown in color. Basalt glasses are most abundant near the quenched margin of lava flows and are commonly altered to greenish palagonite, which might indicate alteration from more reducing fluids than that of brownish palagonite. Alteration veins are abundant at the top of the basement cores and decrease with depth, indicating limited downwelling fluid flow, which is also consistent with fewer fractures that occur with increasing depth. Vein filling minerals include carbonate, celadonite, Fe oxide/hydroxides, saponite, smectite, quartz, and some blue minerals that are difficult to identify. Typical secondary minerals include saponite, Fe oxides, carbonate, and celadonite, which represent a low-temperature alteration assemblage.

We measured 240 fractures and veins in the basalt of Hole U1433B. Most of the fractures occur along existing veins without either obvious offset or striations on the surfaces, indicative of drilling-induced fractures, whereas natural fractures are quite rare. In general, veins can be separated into four types with different shapes: single linear, triple-junction, branched, and crosscutting. Arched, crosscutting, and triple-junction

veins are usually distributed in pillow basalt layers, whereas single linear, branched, or sinuous veins are usually confined to the massive flows. The highest frequency of veins occurs in the pillow basalts, whereas there are fewer veins within the massive flows. Alteration along fractures and veins produced 1–2 cm wide yellow to brown halos.

At Site U1433, interstitial water sulfate concentration decreases with depth and sulfate is almost completely consumed (<1 mM) below ~30 mbsf. Alkalinity increases with depth, reaching a maximum of 25.8 mM at ~30 mbsf, before gradually decreasing with depth. The depth at which sulfate is consumed and alkalinity reaches its peak corresponds to an increase in methane from ~3 to 1100 ppmv. Below this depth, methane varies between ~22,000 and 93,000 ppmv before it decreases significantly below ~590 mbsf. Ethane and other higher hydrocarbons are also present in low concentrations below ~60 mbsf. This indicates that anaerobic oxidation of methane coupled with sulfate reduction is ongoing in the sediment. Other interstitial water chemistry profiles reflect both lithologic changes and diagenetic processes. TOC varies from 0 to 1.0 wt%, with a general decrease downhole. CaCO<sub>3</sub> content ranges from 0.5 to 77.8 wt%, with the lowest values (generally <15 wt%) in the upper 300 m of the site. Intervals with higher CaCO<sub>3</sub> content below 300 mbsf correspond to carbonate turbidite layers in lithostratigraphic Unit II. Peaks in TOC (1–1.5 wt%) at ~450 mbsf and 540–590 mbsf could reflect an influx of terrestrial organic matter; however, additional shore-based work is needed to confirm this interpretation.

The basalt recovered in Hole U1433B has low LOI values (0.52–2.06 wt%), as well as low K<sub>2</sub>O (0.11–0.29 wt%), moderate TiO<sub>2</sub> (1.01–1.77 wt%), and high SiO<sub>2</sub> (48.5–51.1 wt%). In general, concentrations of major elements vary within narrow ranges. When plotted on the alkali vs. silica diagram of volcanic rock types (Le Maitre et al., 1989) (Fig. F12), the data plot within the tholeiite field. As shown in Figure F13, the data from these rocks overlap with but define a much smaller range than those of Indian Ocean and Pacific MORB and are distinct from the Hainan Island OIB and other SCS seamount basalt data fields (Figs. F12, F13). Thus, the basalt samples from Hole U1433B are tholeiites and considered representative of SCS MORB.

At Site U1433, we collected a total of 50 routine 5 cm whole-round samples for microbiological analysis from the seafloor to 790 mbsf. When possible, these samples were collected adjacent to samples for interstitial water measurements. We also collected 164 samples from split cores to study the microbiology of interfaces or coring-induced disturbance. We obtained these samples between 4 and 154 mbsf in Hole

U1433A and between 187 and 854 mbsf in Hole U1433B. Most of the samples collected at Site U1433 were preserved for shore-based analysis of DNA, RNA, and lipids. Some portions of the whole-round samples were selected for cultivation-based studies designed to enrich for anaerobic autotrophs and heterotrophs.

We used three methods of contamination testing during coring at Site U1433: PFTs, microspheres, and FCTs. PFT samples were acquired from the outside and inside of 16 cores between 140 and 390 mbsf in Holes U1433A and U1433B. PFTs were not detected in most of the samples collected and analyzed for this tracer regardless of whether the samples were taken from the outside or the inside of the core. Microsphere tracers were used with the RCB coring system in Hole U1433B between 709 and 854 mbsf. Two microsphere samples were taken from each core collected between these depths: one from scrapings of the core surface and one as a subsample from the interior of each whole-round sample. Twenty-four FCT samples were collected either from the drilling fluids that drained from the core liners when cores arrived on the catwalk or from a sampling port near the mud pumps on the rig floor during active coring. The fluids collected for FCT samples correspond to cores obtained from depths ranging between 6 and 824 mbsf.

We conducted paleomagnetic studies at Site U1433 on both sediment and basement cores using pass-through magnetometer measurements on all archive-half sections and AF demagnetization on representative discrete samples. Magnetostratigraphic records at Site U1433 suggest the existence of eight short reversed polarity events within the Brunhes normal chron. These short-lived events most likely represent geomagnetic excursions, as both declination and inclination change. The polarity shifts at depths of ~12, 18, 28, 48, 53, 132, and 152 mbsf match well with known excursion events: Mono Lake (33 ka), Laschamp (41 ka), Blake (120 ka), Iceland Basin (180 ka), Pringle Falls (211 ka), Big Lost (560–580 ka), and marine isotope Stage 17 (670 ka). For two directional anomalies at ~78 and 88 mbsf, there are no counterparts from previous studies, and further shore-based work is needed to confirm the origin of these two anomalies. The Brunhes/Matuyama Chron boundary (0.781 Ma) is tentatively placed at ~188 mbsf in Core 349-U1433A-20H, which indicates a higher sedimentation rate (~23.7 cm/k.y.) for the Middle–Late Pleistocene compared to Sites U1431 and U1432 (Fig. F18). Such a high sedimentation rate facilitates preservation of the short-lived polarity excursions mentioned above.

In Hole U1433B, six major normal chrons are recognized and tied to the geomagnetic polarity timescale using constraints from biostratigraphy. The basal boundaries for

the Matuyama Chron (2.581 Ma), Gauss Chron (3.596), and Gilbert Chron (6.066 Ma) are placed at ~350, 420, and 550 mbsf, respectively. The basal age for sediment in Core 349-U1433B-60R is ~11 Ma. Paleomagnetic results for the basalt units show that the upper part of the basement (805–817 mbsf) is dominated by normal polarity. Between ~817 and 830 mbsf, a relatively well defined reversed polarity zone is observed. Below this depth range, the paleomagnetic inclinations display both normal and reversed polarities. Overall, the remanent magnetization of rocks below ~817 mbsf is dominated by reversed polarity. This pattern is similar to that found in the upper part of the basalt units at Site U1431.

Cores from Holes U1433A and U1433B were measured for physical properties on whole-round cores, split cores, and discrete samples. The physical properties correlate well with lithology, composition, and observed lithification. Bulk density, *P*-wave velocity, shear strength, NGR, and thermal conductivity increase gradually with depth over the uppermost 150 m (Fig. F17), whereas the porosity measured on discrete samples decreases from 90% to 50% over the same depth range. This indicates that sediment compaction dominates physical property variations above 150 mbsf. Below 240 mbsf, variability in porosity, magnetic susceptibility, and NGR values reflects interbedding of carbonate and clay layers (Fig. F17). An increase in *P*-wave velocity from ~1700 to ~2000 m/s near 550 mbsf coincides with stronger lithification in the deeper sediment. From 680 to 750 mbsf, *P*-wave velocities measured in the lithified carbonates reach ~2600 m/s, contrasting strongly with those measured in the clay (~2000 m/s) (Fig. F17). The strong reflectors observed in the seismic profile from this site probably result from this contrast in velocity. Magnetic susceptibility gradually increases and NGR decreases in the clays between 750 and 800 mbsf (Fig. F17). The basalts below 800 mbsf display very low NGR and porosity and variable magnetic susceptibility. Some of the fresh, phenocryst-rich basalt has very high magnetic susceptibility and *P*-wave velocities.

The modified triple combo and FMS-sonic tool strings were run in Hole U1433B. Both tool strings reached 840 m WSF, ~18 m short of the bottom of the hole (Fig. F17). Between 100 and 550 m WSF, there are rapid variations in borehole diameter from ~25 to >43 cm. Below 550 m WSF, the hole diameter is mostly in gauge, with fewer washed out zones. Density and sonic velocity increases from the top of the logs at 100 m WSF downhole to 750 m WSF, caused by compaction and cementation with depth. Superimposed on this trend, excursions to higher velocity and photoelectric factor (PEF) and to lower NGR mark the occurrence of carbonate beds (Fig. F17). This information was used to infer lithology in the unrecovered intervals of Hole U1433B. In the red

clay of Unit III, from ~750 to 800 m WSF, high values in the PEF log indicate that hematite and other oxides increase in concentration downhole toward the top of the basalt at ~800 m WSF. Pillow basalt, a massive basalt flow, fractures, and veins are seen in the FMS images in the basement.

## Site U1434

### Background and objectives

Site U1434 (proposed Site SCS-4E) is located about 40 km northwest of Site U1433 and is directly on the uplifted shoulder of the relict spreading center in the Southwest Subbasin (Figs. F7, F8). This site is also located just south of a large seamount that formed near the relict spreading center after the termination of seafloor spreading. During coring at Site U1433, we decided to use some of our remaining time to core at a second site in the Southwest Subbasin to obtain basement samples more proximal to the extinct spreading center. Site U1434 also offered the opportunity to sample volcaniclastic material from the nearby seamount, which can be compared to the seamounts located near Site U1431 in the East Subbasin.

Sites U1434 and U1433 form a short sampling transect in the Southwest Subbasin (Fig. F7), and with age controls from these two sites, the evolution of the Southwest Subbasin can be better understood. Coring at these sites should help to explain the sharp differences in magnetic amplitude between the East and Southwest Subbasins and test the existing opening models for the Southwest Subbasin (e.g., Pautot et al., 1986). Coring will help determine the age of this subbasin near the end of seafloor spreading and correlate ages from magnetic anomalies with biostratigraphic, magnetostratigraphic, and radiometric ages. The apparent weak magnetization in basement rocks (Li et al., 2008) will be examined through petrological and geochemical analyses and by measurements of magnetic susceptibility and remanent magnetization. Rock samples cored here will place constraints on mantle evolution and oceanic crustal accretion, the terminal processes of seafloor spreading, and the timing and episodes of postspreading seamount volcanism in the area of the relict spreading center.

### Operations

After an 18 nmi transit from Site U1433 averaging 10.3 kt, the vessel stabilized over Site U1434 at 0048 h (UTC + 8 h) on 20 March 2014. This site was an alternate site that was originally planned to core from the seafloor with APC/XCB to refusal, drop a free-fall funnel, change to the RCB, and then core 100 m into basement. Because of

time considerations, the plan was modified so that we drilled to ~200 mbsf using the RCB and then cored into basement as deeply as time permitted. Logging would then be considered depending on hole depth and condition. Hole U1434A was drilled to 197.0 mbsf and then cored with the RCB (Table T1). Basement was encountered at ~280 mbsf, and the hole was advanced by rotary coring to a final depth of 312.5 mbsf. The hole was terminated because of poor hole conditions and poor recovery. At this site there was one drilled interval of 197.0 m. The RCB was deployed 14 times, recovering 26.43 m of core over 115.5 m of penetration (22.9% recovery).

### Principal results

The cored section at Site U1434 is divided into four lithostratigraphic units, three sedimentary and one igneous (Fig. F21). Lithostratigraphic Unit I (197.00–235.10 mbsf) is a 38.1 m thick sequence of upper Miocene dark greenish gray claystone interbedded with black volcanoclastic sandstone and occasional breccia. The fine-grained sediment is mottled greenish and light buff brown, with the browner sediment preferentially found in burrows. This unit is marked by strong bioturbation within the claystone intervals that make up ~40% of the total sediment. The trace fossil assemblages seen within the claystone intervals are consistent with sedimentation in deep water (i.e., lower bathyal or abyssal depths; >2500 m), with assemblages dominated by *Chondrites* and *Zoophycos*, although more vertical burrows are also noted. Sandstone beds are typically dark gray or black in color and are composed of volcanoclastic fragments. The volcanoclastic sandstone and breccia are interpreted to be part of the sedimentary apron of a nearby seamount because they contain abundant volcanic glass fragments, scoria, and basalt clasts, as well as isolated crystals of plagioclase, olivine, and biotite.

Lithostratigraphic Unit II (235.10–254.59 mbsf) contains upper Miocene greenish gray nannofossil-rich claystone with very thin claystone with sand interbeds. The color of the sediment varies at the decimeter scale as a result of changes in the carbonate and clay content. The sediment is locally a light greenish gray color, reflecting higher biogenic carbonate content over those intervals. Unit III (254.59–278.27 mbsf) consists of dominantly massive yellowish brown claystone with nannofossil- or foraminifer-rich claystone of latest middle to late Miocene age. This unit is primarily distinguished from Unit II by its color, which tends to be more yellowish or reddish brown compared to the greenish gray tones associated with the overlying unit.

Analysis of calcareous nannofossils and planktonic foraminifers in core catcher samples and additional samples from split cores indicates that the sedimentary succession

recovered at Site U1434 spans the uppermost middle to upper Miocene, with the base of the sequence younger than 11.9 Ma (Fig. F22). Calcareous nannofossils are generally common to abundant but decrease in abundance downhole, and preservation is poor to moderate. Planktonic foraminifers vary from common to absent, with good to poor preservation, but are frequently fragmented. Radiolarians are present in only one sample. Although none of the species present are biostratigraphic index taxa, the radiolarian assemblage is consistent with the late Miocene age inferred from nannofossils and foraminifers. Correlation of microfossil biohorizons and paleomagnetism data suggest a sedimentation rate of ~1.6 cm/k.y. for the sediment sequence recovered at Site U1434 (Fig. F22).

We cored 30.28 m into igneous basement below 278.37 mbsf in Hole U1434A, recovering 3.05 m of basalt (10.1% recovery). This basement succession is divided into seven igneous lithologic units, which are grouped into lithostratigraphic Unit IV (Fig. F23). The basement at Site U1434 comprises a succession of small pillow basalt flows or a thicker autobrecciated pillow lava flow with three occurrences of hyaloclastite breccia. The igneous basement comprises angular to subangular basalt fragments that are aphyric and have glassy to aphanitic groundmasses. The only phenocrystic phase is olivine, which appears as sparse euhedral-subhedral microphenocrysts throughout the core. The groundmass contains abundant plagioclase microlites, growing in spherulitic and variolitic patterns, with the majority of the groundmass consisting of variably altered mesostasis. Clinopyroxene is only observed in a few thin sections, growing in patches and filling the interstitial spaces between plagioclase microlites. Most of the basalt is nonvesicular to sparsely vesicular. The hyaloclastite breccia contains abundant fresh volcanic glass shards in a mostly clay and/or carbonate matrix. All basalts have phase assemblages of olivine ± plagioclase, and some slightly coarser basalt pieces also have clinopyroxene in their groundmass. These resemble typical MORB crystallization assemblages.

Basalt alteration at Site U1434 is typical of that of MORB. The recovered basalt is slightly to moderately altered. Pillow basalt pieces are altered in zones, with alteration color ranging from dark gray in the interior to light yellow-brown in halos along the outer rims. Typical secondary minerals include saponite and other clay minerals, Fe oxides, carbonate, and celadonite, which constitute a low-temperature alteration assemblage. Fresh basalt glass exists near some of the pillow basalt margins and in the clasts of hyaloclastite breccia. Those basalt glasses are partially altered to orange and brown palagonite. Most of the vesicles are empty or only partially filled with Fe oxide,

saponite, celadonite, and/or carbonate. Only two alteration veins were observed in this short basement section.

Most fractures observed in the sedimentary sequence at Site U1434 are drilling induced. One fracture shows some offset that suggests it occurred prior to consolidation of the sediments. Fractures are rare in the small amount of basalt recovered at this site. Several linear veins are present and filled with carbonate or Fe oxide.

We measured alkalinity and pH on five interstitial water samples taken from 207.9–264.8 mbsf in Hole U1434A. Alkalinity increases from 0.5 at 208 mbsf to 3.5 at 257 mbsf and then decreases in the two samples below that depth. The pH decreases from 7.9 at 208 mbsf to 7.2 at 265 mbsf and then increases slightly just above basement. Methane was detected in very low concentrations (<3.1 ppmv) in the headspace gas samples taken at this site. CaCO<sub>3</sub> content is low (<10 wt%) in lithostratigraphic Units I and II. Samples from the base of Unit III are higher in CaCO<sub>3</sub> (15–30 wt%). TOC is also low (<0.5 wt%), with the highest values near the base of the sedimentary section. ICP-AES major and trace element results from Site U1434 indicate that the basalt has somewhat higher K<sub>2</sub>O than those at Sites U1431 and U1433 but is still tholeiitic in composition and similar to MORB (Figs. [F12](#), [F13](#)).

We collected six routine 5 cm whole-round samples for microbiological analysis from depths of 208–275 mbsf in Hole U1434A. These samples were collected adjacent to samples for interstitial water measurements so that microbiological data and water chemistry data are proximal. We also collected and preserved 13 samples from either the split cores on the sampling table or from basement samples shortly after the samples were retrieved from the catwalk to investigate the microbiology of interfaces. The whole-round and split core samples were preserved for shore-based characterization of the microbial communities (i.e., DNA, RNA, lipids, and cultivation-based studies).

We also collected samples for measuring contamination testing tracers, including microspheres and FCTs. Microsphere tracers were used with the RCB coring system in Hole U1434A by adding them to the core catcher for cores collected between 208 and 303 mbsf. Two microsphere samples were collected from each of the cores collected between those depth intervals: one from scrapings of the core surface and one as a subsample from the interior of each whole-round sample. Microscopic counts of the microspheres in these samples will be performed in shore-based laboratories. Six FCT samples were collected from drilling fluids that drained from the core liners when cores arrived on the catwalk or from a sampling port near the mud pumps on the rig

floor during active coring. The fluids collected for FCT samples correspond to cores obtained from depths ranging between 208 and 293 mbsf. Microbial community DNA and lipids from FCT samples will be compared to the same measurements made on the core samples to determine if the drilling fluids contain microbes that can be regularly tracked as recognizable contaminant taxa.

We conducted paleomagnetic studies at Site U1434 on both sediment and basement cores using pass-through magnetometer measurements on archive-half sections. NRM intensity ranges from 0.001 to 0.1 A/m for the sediment units and increases to several A/m for the basalt units, suggesting that the basalt contains more iron oxides than the sediment. Because of the poor recovery at the site, only fragmentary patterns of magnetic polarity are observed. Available biostratigraphic data allow us to tentatively correlate certain parts of the magnetic polarity interval recorded in the sediments with the geomagnetic polarity timescale. Near the base of the sedimentary sequence, biostratigraphy indicates an age <11.9 Ma, which we use to correlate the negative inclinations at ~278 mbsf to Chron C5r (11.056–12.049 Ma). The long, dominantly positive inclinations between ~250 and 270 mbsf may represent the long normal Subchron C5n (9.984–11.06 Ma), the short normal polarity zone between ~235 and 240 mbsf appears to have recorded Chron C4An (8.771–9.015 Ma), and the normal polarity zone between 205 and 210 mbsf can be tentatively assigned to Chron C4n around 7.15 Ma (Fig. F22).

Cores from Hole U1434A were measured for physical properties on whole-round cores, split cores, and discrete samples. In general, the physical properties correlate well with lithology, composition, and the observed lithification. Because of the low recovery rate, measurements of physical properties show significant discontinuities between intervals. In Hole U1434A, the observed range of values for magnetic susceptibility ( $30 \times 10^{-5}$  to  $80 \times 10^{-5}$  SI) and NGR (25–45 cps) in Units I–III are typical for clay material, which dominates the sediment layers (Fig. F21). The low NGR value in Unit IV corresponds to the basalt layer. The magnetic susceptibility values in the basalt ranges from  $10 \times 10^{-5}$  to  $90 \times 10^{-5}$  SI, which is much lower than what is typical for basalt (Fig. F21). The high grain densities in the claystone of Units II and III suggest the presence of heavy minerals, such as hematite. The porosity measured on discrete samples increases from 40% to 60% with depth, which may be correlated to the lithification and composition of the claystone.

## Site U1435

### Background and objectives

Coring at Site U1435 (proposed Site SCS-6C) became a high priority after failing to achieve our basement objectives at Site U1432 when the final cementing operations compromised the reentry system. This site was originally added as an alternate because of the high risk of being unable to reach basement at Site U1432. The site is located on the continental side of the continent/ocean boundary and is fundamentally different from Site U1432 but nonetheless does have the potential to provide information about the breakup process. Site U1435 is located on a structural high at the transition between the extended continental crust and the oceanic crust (Figs. F6, F8). Similar conspicuous structural high features can be found on the continent/ocean boundary in many other seismic profiles crossing the SCS northern margin and therefore appear to represent tectonic structures typical of the area. The formation mechanism and nature of this structural high was still speculative; it could have been a volcanic extrusion associated with continental extension at the onset of seafloor spreading, lower crust material emplaced from preferential lower crust extension, exhumed mantle material, or a structural high composed of older (Mesozoic) sedimentary rock. Coring at this location was designed to help pinpoint the exact nature of this structure and improve our understanding of early continental breakup, the rift-to-drift transition, and seafloor spreading processes.

### Operations

After a 336 nmi transit from Site U1434 averaging 8.5 kt, the vessel stabilized over Site U1435 at 1524 h (UTC + 8 h) on 24 March 2014. Because we anticipated shallow sediment cover (~10 m), we conducted a 3.5 kHz sonar survey to select a location with maximum sediment thickness to help stabilize the drill string when trying to penetrate basement with thin sediment cover in rough weather. After reaching basement, the plan was to core as deeply into basement as time permitted. Sediment thickness was significantly greater than expected based on the seismic interpretation. Hole U1435A was cored with the RCB to a final depth of 300.0 mbsf when time allocated to the expedition expired, never reaching igneous basement (Table T1). The RCB was deployed 32 times, recovering 171.37 m of core over 300.0 m of penetration (57.1%).

### Principal results

The cored section at Site U1435 is divided into three sedimentary lithostratigraphic units (Fig. F24). Unit I (0–77.65 mbsf) is a sequence of Oligocene–Pleistocene greenish

gray nannofossil-rich clay and clayey nannofossil ooze, together with manganese nodules. The unit is divided into Subunits IA and IB based on variations in the nannofossil content of the sediment. Subunit IA (0–36.04 mbsf) is Miocene to Pleistocene in age and consists of manganese nodules underlain by clayey nannofossil ooze. The manganese nodules have a lobate appearance and are typically associated with very low sedimentation rates. The massive clayey nannofossil ooze has a few *Planolites* trace fossils visible on the cut surface of the core. Subunit IB (36.04–77.65 mbsf) is Oligocene in age and consists of mostly greenish gray nannofossil-rich clay and lesser quantities of greenish gray clay. There are interbedded silty clay and clay with silt intervals, but deeper in the section the sediment becomes more calcareous, primarily through an increase in the proportion of nannofossils. The sediment is heavily bioturbated with trace fossils of the *Nereites* ichnofacies.

Unit II (77.65–275.54 mbsf) is a 197.89 m thick sequence of pre-Oligocene thick-bedded and mostly medium-grained dark gray silty sandstone, with very little carbonate and minor sandy siltstone and conglomerate. The sandstone is better cemented than the Unit I nannofossil-rich clay and increases in lithification downhole. Units I and II are separated by a hard carbonate rock that likely represents a hiatus. The sandstone is moderately well sorted and is characterized by dispersed carbon fragments, shell fragments, and current lamination that is largely disrupted by bioturbation, with burrows typical of the *Cruziana* ichnofacies indicative of shallow-marine conditions. Several whole bivalves and gastropods occur in the sandstone. Unit III (275.54–300.00 mbsf) is a 24.46 m thick sequence of dark gray silty sandstone, silty mudstone, and minor conglomerate. The unit is distinguished from Unit II by being generally finer grained.

We analyzed all core catcher samples and additional samples from split cores for calcareous nannofossils, foraminifers, and radiolarians at Site U1435. Based on nine nannofossil and four planktonic foraminifer bioevents, the sedimentary sequence above 77.65 mbsf is assigned an age spanning the early Oligocene (<33.43 Ma) to the Pleistocene (>0.12 Ma), with possible unconformities or condensed sections existing between the upper Oligocene and middle Miocene, between the upper Miocene and lower Pliocene, and between the upper Pliocene and Middle Pleistocene. Based on a limited number of bioevents, sedimentation rates during the Oligocene were ~0.5 cm/k.y. (Fig. F25).

Samples from 77.65 to 300 mbsf are barren of nannofossils, radiolarians, and planktonic foraminifers. A few long-ranging, shallow-water benthic foraminifers occur in

samples from ~200 to 250 mbsf. Although these specimens are not useful for age control, they indicate a depositional environment of brackish water to shallow marine for Unit II, consistent with the deltaic setting inferred from the sedimentology and trace fossil assemblage.

A small number of deformation structures are present in the sedimentary rock of Site U1435. Most of the fractures are drilling induced, and in the black mudstones near the base of the section, these induced fractures developed along the bedding. Two normal fault structures are found in the sandstone, each composed of several fractures that have little offset. No deformation or thickness changes occur in the rock of the hanging walls and footwalls, indicating that these faults occurred at a later stage and did not control sedimentation. One linear white carbonate vein was found in the sandstone. Bedding is generally horizontal or subhorizontal in Unit I, but toward the base of Units II and III the strata are inclined to a significant degree ( $>25^\circ$ ). These dips are not depositional and are interpreted to reflect rotation caused by normal faulting, possibly during formation of the structural high on which the site is located.

Downhole interstitial water concentrations of chloride, bromide, and sodium are variable and slightly higher than modern seawater; however, the Na/Cl ratio is ~0.85 throughout the sampled interval, which indicates that the interstitial water is of typical marine origin. Only very low concentrations ( $<10$  ppmv) of methane and ethane were detected in the headspace gas samples from Hole U1435A.  $\text{CaCO}_3$  content in the upper part of the hole is higher than that of the lower part, which corresponds to the change from nannofossil ooze and nannofossil-rich clay in lithostratigraphic Unit I to sandstone in Unit II. Despite variable TOC with depth, the ratio of TOC to total nitrogen (C/N) suggests that TOC is dominated by a terrestrial organic matter source, with lower input from marine organic matter.

We collected 25 routine 5 cm whole-round samples for microbiological analyses from 37 to 299 mbsf in Hole U1435A. These samples were collected adjacent to samples for interstitial water measurements so that microbiological data and water chemistry data are proximal. The whole-round samples were preserved for shore-based characterization of microbial communities (i.e., DNA, RNA, lipids, and cultivation-based studies).

We also collected samples for measuring contamination testing tracers, including microspheres and FCTs. Microsphere tracers were used with the RCB in Hole U1435A by adding them to the core catcher for Cores 349-U1435-5R through 32R (37–299 mbsf).

Two microsphere samples were taken from each of the cores collected between those depth intervals: one from scrapings of the core surface and one as a subsample from the interior of each whole-round sample. Microscopic counts of the microspheres in these samples will be performed in shore-based laboratories. Five FCT samples were collected from drilling fluids that drained from the core liners when cores arrived on the catwalk or from a sampling port near the mud pumps on the rig floor during active coring. The fluid collected for FCT samples corresponds to cores obtained from between 90 and 273 mbsf. Microbial community DNA and lipids from FCT samples will be compared to the same measurements made on the core samples to determine if the drilling fluids contain microbes that can be regularly tracked as recognizable contaminant taxa.

We performed measurements of NRM on all archive-half cores from Hole U1435A. We subjected these cores to AF demagnetization up to 20 mT in order to establish a reliable magnetostratigraphy at the site and to observe the magnetic properties of the different lithologies recovered. Because of time constraints, we were unable to perform measurements and demagnetization on discrete samples taken from the working halves. Overall, paleomagnetic data at Site U1435 are reasonably robust and provide magnetic information about the recovered sediment. Several relatively well defined polarity intervals are identified in the downhole magnetostratigraphic records, despite some samples showing unstable and ambiguous magnetization. Based on biostratigraphic data, we were able to tentatively correlate certain parts of the magnetic polarity interval recorded in the sediment with the geomagnetic polarity timescale. Assuming no significant hiatus between the marine Oligocene nannofossil-rich clay (Subunit IB) and the sandstone of Unit II, the Chron C16n/C15r boundary (36.05 Ma) is tentatively placed at ~280 mbsf. This interpretation indicates relatively high sedimentation rates for the sandstone of Unit II (~5 cm/k.y.) (Fig. F25).

Cores from Hole U1435A were measured for physical properties on whole-round cores, split cores, and discrete samples. Thermal conductivity was measured with a needle probe in soft sediment and then with a contact probe in the sedimentary rock. The physical properties correlate with lithology and observed lithification. *P*-wave velocity increases gradually with depth over the uppermost 150 m (Fig. F24), whereas porosity measured on discrete samples decreases from 65% to 30% over the same depth range, reflecting sediment compaction. Bulk density, NGR, magnetic susceptibility, and thermal conductivity show a sharp increase near 78 mbsf at the lithostratigraphic Unit I/II boundary between the nannofossil-rich clay and sandstone (Fig. F24). A significant increase in *P*-wave velocity and thermal conductivity is observed

near 170 mbsf, which is associated with stronger lithification of the sandstone. Magnetic susceptibility and NGR values decrease with depth below 270 mbsf, which corresponds to the change from a dominance of sandstone in Unit II to mudstone in Unit III (Fig. F24).

## Expedition synthesis

Operations during Expedition 349 (26 January–30 March 2014) drilled five sites in the central basin of the SCS (Figs. F1, F2, F8). Sites U1431, U1433, and U1434 were cored into the igneous basement near the fossil spreading center where seafloor spreading terminated, whereas Sites U1432 and U1435 are located proximal to the northern continent/ocean boundary where seafloor spreading started. In total, we recovered 1524 m of sediment and sedimentary rock and 78 m of igneous basement and carried out geophysical logging (triple combo and FMS-sonic tool strings) at Sites U1431 and U1433. The materials recovered and data collected were extensively examined and discussed and allow us to draw the following conclusions concerning the opening history of the SCS, the sedimentary and paleoceanographic responses to the formation of this ocean basin, the mantle source and magmatic processes forming the ocean crust basement, and the geodynamic implications for the tectonics of the region.

## Opening history of the South China Sea

Determining the timing of the onset and cessation of seafloor spreading in the SCS were the primary objectives of Expedition 349. At all three sites near the fossil spreading center, we recovered deep-sea claystone near the sediment/igneous basement interface, with interflow claystone between lava flows recovered at Site U1431, and evidence from downhole measurements for an unrecovered interflow sedimentary layer at Site U1433 (Figs. F11, F19, F23). Microfossils within these claystone units provide preliminary age models for the sedimentation history, which in turn helps us to refine the oceanic crustal age models. Relatively unaltered basalt from the ocean crust near the relict spreading center was recovered and will be dated using  $^{40}\text{Ar}/^{39}\text{Ar}$  methods.

The age at which seafloor spreading ceased in the East Subbasin is estimated at ~16.7–17.5 Ma based on microfossils in the interflow claystone (Fig. F10), or even slightly younger because Site U1431 is ~15 km off the ridge axis. At Site U1433, ~50 km away from the relict spreading center in the Southwest Subbasin, we recorded a biostrati-

graphic depositional age range from ~18 to 21 Ma for sediment directly above the basement (Fig. F18). Rare and poorly preserved Oligocene to earliest Miocene calcareous nannofossils were also observed in sediment attached to basalt pieces in the upper part of the basement at Site U1433, which could indicate a substantially older age for the basement; however, it is not clear if the nannofossil assemblages are reworked or in situ.

Located just 35 km north of Site U1433, Site U1434 is on the uplifted shoulder of the relict spreading center and is only ~15 km from the spreading axis in the Southwest Subbasin. Here, biostratigraphic age data indicate that the basal sedimentary sequence, lying just above the basaltic basement, is younger than 12 Ma. The uplifted shoulder forms a topographic high that may have contributed to a depositional hiatus or extremely low sedimentation rates between the emplacement of basalt and the earliest sedimentary deposits. We deduce that the cessation age of seafloor spreading in the Southwest Subbasin is somewhere between ~12 and ~21 Ma. Overall, there does not appear to be a large difference in the ages at which seafloor spreading finished between the two subbasins.

We note here that the recorded biostratigraphic age ranges are likely minimum estimates because evidence from paleomagnetic reversals in the basalt units point to prolonged eruption histories at these sites. Postcruise radiometric dating of basement basalt from these sites, plus calibration with magnetic anomalies and paleomagnetic measurements, will constrain the eruptive history of the igneous basement at these sites in the SCS.

Because of a technical error in cementing the final casing string in Hole U1432B, we were unable to reach the oceanic basement near the continent/ocean boundary at the deepest planned drill site. This prevented us from collecting basement samples to directly date the onset of seafloor spreading. However, we were able to drill into one of the most enigmatic structures in the area, a structural high standing along the continent/ocean boundary at Site U1435. Coring here recovered a sharp unconformity, with sediment above dated to ~33 Ma. The sediment above the unconformity records deep marine facies, with sediment below dominated by sandy lithologies of shallow-marine deltaic or coastal facies. The age of this deeper unit, which is composed mainly of poorly sorted sandstone and thin black silty mudstone that are both relatively rich in organic matter (~0.4–1.3 wt%), awaits further shore-based studies as it is nearly barren of calcareous and siliceous marine microfossils. Immediately above the unconformity, drilling recovered abundant recrystallized calcite and dolomite

grains, which may have been formed by extremely slow sedimentation or diagenesis. Nevertheless, we interpret this sharp unconformity as the break-up unconformity caused by the initial opening of the SCS, which places the onset of seafloor spreading at ~33 Ma.

## Sedimentary and paleoceanographic responses

### Silt and carbonate turbidites

All sites contain deep-marine deposits that likely formed at water depths deeper than 3 km but show significant spatial variations in postspreading sedimentary environment and provenance. Site U1431, in the East Subbasin, records the strongest evidence of hemipelagic, deep-marine gravity flow deposition of material eroded from various (distal) terrestrial sources. Both silt and nannofossil-rich/calcareous turbidites are present, with the former being much more dominant. Silt turbidites are speculated to have been triggered by volcanism and/or earthquake events associated with the Manila subduction zone and/or the Taiwan Orogeny, with sources located to the east and northeast, whereas calcareous turbidites at this site were likely transported from local sources, possibly nearby seamounts topped by carbonate platforms (Fig. F8).

In contrast, Site U1433 in the Southwest Subbasin has nannofossil-rich calcareous turbidites that are more frequent in the cores, with some beds over several meters thick. These turbidites date to the late Miocene. Here the relict spreading center, with well-developed uplifted shoulders and a relatively deep axial trough, likely acted as an effective barrier, preventing terrestrial material from being transported to this site from northerly landmasses such as southern China, the Philippines, or Taiwan. Other possible sources in Borneo or mainland Southeast Asia are more likely. The source of the carbonate turbidites is most likely within the southerly Dangerous Grounds or the Reed Bank area (Fig. F8). Local sources, such as isolated seamounts or abyssal highs, are less likely because they are quite far away from the site or in relatively deep water. Variations in carbonate flux to Site U1433 may reflect subsidence and drowning of the carbonate reefs in the Dangerous Grounds and/or sea level changes.

Variation in the character of the uppermost Pleistocene sediment between Sites U1431 and U1432 also support contrasting provenances in different parts of the basin at that time. The uppermost unit from Site U1431 is dominated by turbidite silt and sand and has frequent ash layers (Fig. F9), whereas the uppermost unit from Site U1432 is mostly clay and shows fewer ash layers over a similar age interval (Fig. F15).

At Site U1433, eight geomagnetic excursions have been identified within the Brunhes Chron due to an extremely high sedimentation rate. Based on our current knowledge, two of the excursions have not been reported in previous studies, and postcruise studies will help determine their origin. A sudden increase in sedimentation rates from 5–9 to ~20 cm/k.y. is recorded at ~1 Ma at Site U1433 (Fig. F18) and may reflect some coupling effects of enhanced terrestrial supply and intensified sea level fluctuations associated with the mid-Pleistocene climate transition.

### **Variations in carbonate compensation depth**

Variations in the carbonate compensation depth (CCD) may have had an effect on the massive deepwater carbonate sediments recovered during the expedition, but the mechanisms are not clear. Sediment at Sites U1431 and U1433 was apparently deposited at depths greater than the modern CCD or, alternatively, may have been strongly diluted by variable clastic flux from the continents. However, at Site U1434, sediment shows much less influence from turbidity currents and is rich in calcareous nannofossils. Here, sediment was deposited at slightly shallower water depths on top of a rifted basement high (Fig. F7). The mid-ocean ridge itself was also likely shallower prior to the postspreading subsidence caused by thermal and isostatic processes, as well as the loading from emplacement of a younger seamount on top of the spreading center. Sediment recovered at Site U1434 must have been deposited above the CCD and its compositional changes may reflect CCD variations after tectonic subsidence corrections.

### **Pelagic brownish to reddish or yellowish brown claystone**

At Sites U1431, U1433, and U1434, we recovered a series of reddish brown to yellowish brown claystone and claystone with silt directly above the basement basalt units. At Site U1431 in the East Subbasin, this lower middle Miocene (~12–14 Ma) unit is only ~5 m thick and is massive and homogeneous in the lower part and laminated with silty claystone in the upper part (Figs. F9, F11). Another similarly colored lower Miocene (~16–18 Ma) claystone ~10 m thick is interbedded within the basalt lava sequence but is less homogeneous, showing evidence for local mass wasting, and is characterized mostly by claystone with minor intraformational breccia or conglomerate containing rare basalt clasts that have well-developed reaction rims.

At Site U1433 (Figs. F17, F19) in the Southwest Subbasin, the yellowish brown claystone and claystone with silt is ~49 m thick and is dated to the middle to late Miocene (~10–18 Ma). Although mostly massive, there are intervals of graded and bioturbated

clayey siltstone and silty claystone. At both Sites U1431 and U1433, only siliceous microfossils (radiolarians) are found in this unit, most likely because calcareous microfossils have been dissolved because of deposition below the CCD. At Site U1434 (Figs. F21, F23), ~24 m of yellowish or reddish brown claystone with variable amounts of nannofossils and foraminifers lies immediately above the basaltic basement. This sequence is dated as latest middle to late Miocene in age (~10–12 Ma) and is massive and structureless, with very little evidence for current influence during sedimentation. In contrast to the other sites, this unit at Site U1434 is characterized by a lack of radiolarians, with abundant foraminifers clearly visible on the core surface.

The reddish brown to yellowish brown claystone units at Sites U1431, U1433, and U1434 were deposited at somewhat different time intervals and water depths but all immediately overlie the basaltic basement. The estimated sedimentation rates are quite low, varying from <0.5 cm/k.y. at Site U1433 (Fig. F18) to <2.0 cm/k.y. at Site U1431 (Fig. F10) and ~1.6 cm/k.y. at Site U1434 (Fig. F22). We interpret the claystone to be largely a product of deep-sea pelagic and hemipelagic sedimentation at very low sedimentation rates. The yellowish brown to dark brown color reflects enhanced oxidation of the clastic components of the sediment, which is a typical feature of regions of slow sedimentation and oxygenated bottom water, such as in many parts of the Pacific, where “red clays” are widespread (Bryant and Bennett, 1988).

Although lacking sedimentary evidence, there may have been some hydrothermal influence on the deposition or later alteration after sedimentation as a result of fluid flow and geochemical exchange. Logging in this unit at Site U1433 showed distinctly high NGR logs of potassium, uranium, and thorium over these intervals (Fig. F17). NGR values decrease slightly, whereas PEF increases with depth toward the claystone/basalt boundary and reaches peaks within the top of the basalt unit. This could reflect an increasing abundance of hematite and other oxides in the claystone. The increased concentration of such oxides could result from hydrothermal processes and fluid flow, as well as chemical exchange between the basalt and overlying sediment.

## Mantle and crustal processes

### Seamount volcanism and terminal processes of the extinct spreading center

Sites U1431 and U1434 are located very close to seamounts developed along and on top of the relict spreading center (Fig. F8). Well-recovered volcanoclastic sandstone and breccia may therefore reveal the history of seamount volcanism following the end of seafloor spreading in the SCS. At Site U1431, we recovered ~280 m of domi-

nantly greenish black volcanoclastic breccia and sandstone, interbedded with minor amounts of claystone (Fig. F9) dated to the late middle Miocene to early late Miocene (~8–13 Ma). This would indicate an approximately 5 m.y. period of extensive seamount volcanic activity that started nearly 4 m.y. after the cessation of seafloor spreading. Volcanoclastic breccia layers comprise much of the section, are generally thicker bedded in the upper parts of this unit, and have normal grading and erosive bases, indicative of deposition by mass wasting either as debris or grain flows.

At Site U1434, volcanoclastic sandstone and minor breccia encountered at the top of the cored interval of the hole show coarse grain sizes and poor sorting (Fig. F21) and are indicative of a relatively local provenance, most likely the adjacent seamount ~15 km to the north (Fig. F8). The age of this unit is late Miocene (younger than 9 Ma). Its upper boundary was not cored, but the penetration rates during drilling of the interval above suggest well-lithified volcanoclastic breccia and sandstone at shallower depths (<200 mbsf). Volcanoclastic material is absent from the sediment deposited between ~12 and 9 Ma in the yellowish brown claystone unit directly overlying the basement basalt. This indicates that this seamount volcanism was not active until ~9 Ma but then was active for at least 2 m.y. based on the cored section. This also puts a time period of ~7 m.y. between the cessation of the seafloor spreading and the initiation of seamount activities in the Southwest Subbasin. This is comparable to late Miocene and Pliocene seamount volcanism found in the extreme southwest of the oceanic basin (Li et al., 2013). Further postcruise sedimentological and geochemical studies will refine the ages and nature of these seamount activities and reveal how magma sources at the dying spreading center evolved through time.

### **Mantle evolution and magma processes revealed by oceanic basalt**

We successfully cored into oceanic basement in the SCS for the first time and recovered basalt at Sites U1431, U1433, and U1434 (Figs. F11, F19, and F23). This allows for the study of the mantle evolution and magmatic processes in this young ocean basin. Despite their apparent differences in groundmass grain sizes, all basalts have variable phase assemblages of plagioclase, olivine, and clinopyroxene, typical of MORB. This interpretation is also supported by geochemical evidence (Figs. F12, F13). Coring at Site U1431 recovered massive basalt lava flows with limited evidence for pillow basalt fragments on top of the section (Fig. F11). Most basalt is aphyric and ranges in grain size from microcrystalline to fine grained, with some medium- to coarse-grained intervals occurring in the interiors of the thickest massive lava flows. These basalts were altered in a low-temperature and oxidative environment, with long in-

tervals only slight affected, providing ample material for postcruise radiometric age dating.

The Site U1433 basement section shows more abundant, small pillow basalt lava flows at the top and a few massive basalt lava flows toward the bottom of the hole (Fig. F19). This basalt ranges from sparsely to highly plagioclase-phyric. Alteration of the basalt at this site is low in intensity and typical secondary minerals represent a low-temperature and both oxidative and nonoxidative alteration assemblage. The contrast in alteration style is interpreted to indicate less active fluid activities at Site U1433 compared to the other sites, possibly caused by the cover of clayey sediment with low permeability.

The basement unit at Site U1434 is comprised of a succession of small pillow lava flows, or a thicker autobrecciated pillow lava flow, with three occurrences of hyaloclastite breccia (Fig. F23). The basalts are aphyric with glassy to microcrystalline groundmasses. The phenocrysts observed are olivine and plagioclase. The secondary mineral assemblage indicates slight to moderate alteration under low temperature, limited fluid flow, and oxidative conditions.

A total of 34 basement basalt samples were analyzed for concentrations of major and trace elements from the three sites. Almost all samples are tholeiitic basalt (Fig. F12) with extremely low  $K_2O$  (<0.3 wt%), in contrast to the much higher  $K_2O$  contents (>1.0 wt%) in the alkali basalt clasts in the younger volcanoclastic breccia. Overall, all concentrations of major elements in the basalt overlap with, but define a much smaller range than those known from compilations of Indian Ocean and Pacific Ocean MORB data, and are distinct from the OIB data fields from nearby Hainan Island and other seamounts in the SCS (Figs. F12, F13). Further postcruise geochemical studies will trace the mantle source and magmatic processes involved during and after opening of the SCS in detail.

## Geophysical constraints and geodynamic implications

During the expedition, a suite of physical property measurements and color spectra scanning was completed on whole-round cores, split cores, and discrete samples. Downhole logging at the two deepest sites provided in situ constraints on the sediments and rocks, which is particularly important over unrecovered intervals. These data will aid in future geophysical interpretations of geophysical data from the SCS.

Compaction and consolidation are controlling factors for physical property variations in the sediment, as measured porosity often has good inverse correlation with other measurements, such as bulk density, *P*-wave velocity, shear strength, NGR, and thermal conductivity. Increased compaction and lithification also lead to sharp velocity contrasts and differentiate velocities of different lithologies that would otherwise be similar. These observations explain the strong seismic reflectivity of strata in the bottom unit of the sedimentary cover at Site U1433, where lithified carbonates show much higher velocities than interbedded claystone (Fig. F17).

NGR downhole logging in the igneous basement at Site U1433 helped define two interflow sedimentary layers between lava units through identification of high peaks in NGR (Fig. F17). This was particularly useful because coring did not fully recover these layers. Cores show only traces of sediment attached to basalt pieces. Gamma ray logging also helped constrain the alternating nature of carbonate with low NGR values and clay layers with high NGR values and is therefore valuable in delineating turbidites.

Magnetic susceptibility was measured on both whole-round cores and the split archive halves. In addition, remanent magnetization, which is proportional to the magnetic susceptibility, was measured with the pass-through magnetometer on all archive halves and on representative discrete samples from the working halves. We found that magnetic susceptibility of the basalt varies from  $\sim 10 \times 10^{-5}$  to  $2000 \times 10^{-5}$  SI (Figs. F9, F17, F21). The values are much higher in relatively unaltered intervals within the more massive basalt flows compared to small lava flow units that are typically more prone to alteration. For now it remains uncertain how the entire basaltic layer of the oceanic crust behaves with respect to magnetic susceptibility, since we only recovered its very top. Overall, we did not observe major differences in the measured magnetic susceptibilities between the East and Southwest Subbasins, whereas differences in magnetic susceptibilities have been previously predicted or suspected by the contrast in surface magnetic anomalies (Li et al., 2008). Therefore, other mechanisms such as spreading rate, thermal disturbance, compositional variation, and posteruption alteration are needed to further explain the observed surface magnetic contrast.

## **Interplay between microbiology, fluid flow, geochemistry, and tectonics**

A suite of samples collected at all of the Expedition 349 sites for microbiological analysis will allow examination of how microbial community features are linked to large-scale geological processes characteristic of the SCS that are representative of subsea-

floor settings worldwide. Samples were collected to examine the importance of ammonia-oxidizing archaea in the sediment in which archaeal biomarkers are preserved, what these archaea indicate about paleoceanographic conditions, and whether *Bdellovibrio* and similar organisms (bacterial predators) exist in the seafloor under contrasting fluid flow and heat flow conditions. These microbiological samples were collected proximal to samples for interstitial water chemistry analysis to help us reconstruct the environmental conditions where these cells are present.

We collected samples allowing us to test the hypothesis that the habitats at key interfaces, such as where volcanic ashes or turbidites overlie fine-grained sediment, provide optimum conditions for microbial colonization and survival. In addition to helping to explain the explicit conditions under which microbial life in the deep seafloor may thrive, these sites provide several different environments that link to large-scale processes such as volcanism, tectonism, and turbidity flows. There is the potential to assess how regional and continental scale events related to erosion, seafloor spreading, and subduction zones can dictate life at the smallest scale.

Samples from most sites drilled during Expedition 349 show low levels of hydrocarbon gases; however, at Sites U1432 and U1433, sediment samples showed evidence of moderately high concentrations of methane. Ethane and propane concentrations increased with depth at these sites. Evidence of higher hydrocarbon contents in this deep-sea sediment is worth additional study, and their presence suggests factors that should be considered regarding the biogeochemistry of these deep seafloor systems and how they respond to regional tectonics and depositional settings.

## Preliminary scientific assessment

Expedition 349 achieved the vast majority of its scientific objectives as outlined in the *Scientific Prospectus* (Li et al., 2013). The expedition also obtained several unexpected findings that bear significant science implications. We set out with five broadly defined objectives, each of which has been addressed as follows at the five sites drilled, cored, and logged during this expedition:

1. Date the timing of the opening of different subbasins of the SCS and correlate the ages from magnetic anomalies to biostratigraphic, magnetostratigraphic, and radiometric ages.
  - a. All of the five drill sites were designed to address this objective, although only at Sites U1431, U1433, and U1434 we were able to penetrate into igneous

basement. Site U1432 was designed to determine the onset age of seafloor spreading in the East Subbasin through coring the lower half of sediment layers and the uppermost 100 m of igneous basement. Hole U1432B was drilled to 800 mbsf with casing successfully installed to address this objective; however, a technical error during the final cementing operation forced us to abandon Hole U1432B. This prevented us from coring the oldest sediment and oceanic crust to determine the initiation age of seafloor spreading in the SCS. We urge the science community to work together toward a future IODP expedition to return to Site U1432.

- b. To determine the age of termination of seafloor spreading in the East Subbasin, we drilled Site U1431 and successfully obtained continuous sediment records and relatively fresh basaltic samples in the basement. Preliminary results for the sediment ages were obtained during the expedition through biostratigraphic and paleomagnetic analyses. Radiometric dating of basalt samples will be conducted during shore-based investigation.
  - c. At Sites U1433 and U1434 we successfully obtained sediment and basalt cores that will allow us to determine the termination age of seafloor spreading in the Southwest Subbasin and compare it to the Site U1431 termination age in the East Subbasin. Preliminary biostratigraphic and paleomagnetic dating was conducted during the expedition, whereas shore-based analysis will provide radiometric ages for the basalts.
  - d. At Site U1435, which is on a structural high near the ocean/continent boundary at the northern edge of the East Subbasin, we successfully obtained cores of Oligocene sediment above and pre-Oligocene sandstone below an unconformity. The obtained samples will provide us an opportunity to investigate the transition from rifting to seafloor spreading in the SCS.
2. Measure the magnetization, mineralization, and geochemical compositions of basement rock to understand the causes of the sharp magnetic contrast between different subbasins.
- a. We successfully obtained igneous basement rock in the East Subbasin (Site U1431) and the Southwest Subbasin (Sites U1433 and U1434), allowing us to measure and fully characterize the magnetization, mineralization, and geochemical compositions of basement rock.
  - b. The results of shipboard physical property measurements and shore-based analyses of the rock samples, integrated with regional geophysical and geological studies, will advance our understanding of the causes of the sharp magnetic contrast between the two subbasins.

3. Evaluate the origin and source evolution of SCS basement rocks to better understand the formation of SCS oceanic crust and the deep mantle processes driving this formation.
  - a. We successfully obtained basalt samples near the relict seafloor spreading centers in the East Subbasin (Site U1431) and the Southwest Subbasin (Sites U1433 and U1434). Preliminary petrological and geochemical studies were made during the expedition, and shore-based geochemical and petrological studies have already been coordinated and will be carried out by multiple laboratories. These studies will help to characterize geochemical compositions of the basement rocks to evaluate the origin and source evolution of the SCS oceanic crust and mantle.
  - b. A surprising finding from the expedition is that we obtained abundant samples of volcanoclastic materials in sedimentary sections at sites near the relict spreading centers of the East and Southwest Subbasins. Shore-based analyses of these volcanoclastics will allow us to date both their eruption and sedimentation ages, as well as to characterize their geochemical compositions. Results will allow us to investigate the combined source evolution of the SCS spreading centers and the nearby seamounts, and how they interacted.
4. Evaluate the paleoceanographic and climatic responses to the opening of the SCS and develop a 3-D sedimentation and subsidence model.
  - a. We obtained several surprising results that were previously unknown to the SCS research community. For example, the sediments reveal abundant turbidite sequences at Sites U1431, U1432, and U1433, suggesting a history of turbulent sedimentary deposition events that were previously unknown.
  - b. Thick carbonate turbidites in the form of deepwater carbonates and chinks found in the Southwest Subbasin (Site U1433) are indicators of provenance, and changes in the supply of these sediments to the site has implications for the paleoceanographic and paleoclimatic evolution in that region.
  - c. We have obtained complete records of the sedimentary seamount aprons, which contain valuable information on the history of seamount eruption and associated volcanoclastic deposits in both the East Subbasin (Site U1431) and the Southwest Subbasin (Sites U1433 and U1434).
  - d. Reddish brown to yellowish brown deep-sea claystone sequences were encountered immediately above the basement at Sites U1431, U1433, and U1434. The scientific implications of these sediment layers were debated and will become clearer after shore-based investigation.

- e. Preliminary ages were obtained through biostratigraphic and paleomagnetic analyses during the expedition. The results revealed a surprisingly wide range of sedimentation rates within individual holes and between different sites. Shore-based investigation will further improve the sedimentation models, identify potential hiatuses in the sedimentary records, and determine the provenance sources of the sediments.
5. Obtain downhole geophysical logs to reveal physical properties of the sediment and the top oceanic basement and to provide a record of unrecovered intervals.
- a. We successfully conducted downhole geophysical logging in the East Subbasin (Hole U1431E) and the Southwest Subbasin (Hole U1433B). These were the first downhole geophysical data obtained in the deep basins of the SCS.
  - b. In the Southwest Subbasin, downhole logging at Hole U1433B was accomplished using the triple combo and FMS-sonic tool strings. We successfully logged a significant proportion of the basement, revealing pillow basalt flow sequences. The downhole logging results provide a record of unrecovered intervals in both the sediment and basement cores, including two possible interbedded sedimentary layers up to 1.5 m thick in the pillow basalt sequence of Hole U1433B.
  - c. In the East Subbasin, downhole logging at Hole U1431E was also accomplished using the triple combo and FMS-sonic tool strings. At this site, the downhole logging tools reached a significant depth of the sediment layers, also providing a record of unrecovered intervals in the sediment cores.

## Operations

### Port call

Expedition 349 began with the first line ashore in Hong Kong at China Merchants Wharf at 0848 h (UTC + 8 h) on 26 January 2014. The science party and technical staff boarded on the day of arrival. The majority of incoming cargo and off-going cargo was loaded and unloaded on 26 January. The following day, the Siem Offshore crew change was completed. All main port call activities, including preparation of the passage plan were completed. Public relation tours were given on all three days of the port call. After taking on 2200 metric tons of marine gas oil, the vessel was secured for sea with the final maintenance checks performed prior to departure.

On the morning of 29 January, two tugs and the harbor pilot arrived at our location. The last line was released from shore at 1238 h, beginning the 463 nmi voyage to Site U1431 (proposed site SCS-3G). The pilot departed the vessel at 1326 h, and the vessel began the sea passage to the first site.

## Site U1431

After a 463 nmi transit from Hong Kong averaging 11.0 kt, the vessel arrived at the first expedition site. A prespud meeting was held prior to arrival to review operations at the first site. The vessel stabilized and switched from cruise mode to dynamic positioning over Site U1431 at 0640 h on 31 January 2014. The positioning beacon was then deployed at 0712 h.

The bottom-hole assembly (BHA) was picked up and assembled and then run in the hole with drill pipe to 4165.25 meters below rig floor (mbrf). All drill pipe was measured (strapped) and the internal diameter verified (drifted) during the pipe trip. There were no operational problems running the drill string into the hole. The top drive was picked up, the drill string circulated out, and a pig was pumped to remove any debris that might have accumulated in the string. The calculated precision depth recorder (PDR) depth for the site was 4252.1 mbrf, and after some consideration 4248 mbrf was selected as the shoot depth for the first core. The bit was spaced out to 4248 mbrf and the APC barrel was run in the hole with wireline and landed. Hole U1431A was spudded at 0040 h on 1 February. The mudline core recovered 9.45 m of sediment and the seafloor was calculated to be 4248.1 mbrf (4237.3 meters below sea level [mbsl]). Nonmagnetic core barrels were used for APC coring from Core 349-U1431A-1H through 3H. Hole U1431A was terminated by plan at a final depth of 4276.5 mbrf (28.4 mbsf). At the conclusion of coring, the drill string was pulled from the hole. The seafloor was cleared at 0345 h on 1 February, ending Hole U1431A. Three piston cores were taken over a 28.4 m interval, with a total recovery of 28.39 m of core. Overall core recovery for Hole U1431A was 100.0%. The total time spent on Hole U1431A was 21.0 h.

After the bit cleared the seafloor, the vessel was offset 20 m east of Hole U1431A. As part of the planned microbiological analyses, the PFT pump was turned on and the drill string displaced with contamination testing fluid. The pump remained on for the remainder of coring operations in Hole U1431B. The bit was spaced out to 4245.5 mbrf in an attempt to recover ~7.0 m on the mudline core. The mudline core recovery was 7.5 m. The seafloor depth was calculated to be 4247.5 mbrf (4236.7 mbsl). Hole

U1431B was spudded at 0420 h on 1 February. Nonmagnetic core barrels were used for APC coring from Core 349-U1431B-1H through 2H to a final depth of 17.0 mbsf. At the conclusion of coring, the drill string was pulled from the hole. The bit cleared the seafloor at 0620 h, ending Hole U1431B. Two piston cores were taken over a 17.0 m interval in Hole U1431B, with a total recovery of 17.16 m of core (100.9%). The total time spent on Hole U1431B was 2.58 h.

After the bit cleared the seafloor, the vessel was offset 20 m south of Hole U1431B. The bit was spaced out to 4245.5 mbrf. The mudline core recovery was 4.7 m, but the core liner was split. The seafloor depth was calculated to be 4250.3 mbrf (4239.5 mbsl). Hole U1431C was spudded at 0700 h on 1 February. Nonmagnetic core barrels were used for APC coring from Core 349-U1431C-1H through 2H to a final depth of 14.2 mbsf. The PFT pump remained running during coring in Hole U1431C. Hole U1431C was terminated when we determined that the mudline core would not meet sampling requirements. At the conclusion of coring, the drill string was pulled from the hole. The bit cleared the seafloor at 0852 h on 1 February, ending Hole U1431C. A total of two piston cores were taken over a 14.2 m interval in Hole U1431C, with a total recovery of 14.45 m of core (101.8%). The total time spent on Hole U1431C was 2.42 h.

After the bit cleared the seafloor, the vessel was offset 20 m west of Hole U1431C. The bit was spaced out to 4245.0 mbrf. The mudline core recovery was 3.22 m. The seafloor depth was calculated to be 4251.3 mbrf (4240.5 mbsl). Hole U1431D was spudded at 0925 h on 1 February. Nonmagnetic core barrels were used for APC coring from Core 349-U1431D-1H through 19H to a depth of 168.9 mbsf. Temperature measurements were taken with the APCT-3 on Cores 4H, 7H, 10H, and 13H with good results. After six partial strokes of the APC, the coring system was switched over to the XCB. XCB coring continued from Core 20X through 67X at a final depth of 4868.3 mbrf (617.0 mbsf). The PFT pumps remained on through Core 23X. While cutting Core 67X, the rate of penetration dropped severely and the core barrel was retrieved after a 2.7 m advance. While recovering the core barrel at the surface, we discovered that the cutting shoe, core catcher sub assembly, and the break off sub were missing from the XCB coring assembly. With ~1 m of junk metal remaining in the hole, we decided to pull out of the hole, offset, and begin a new hole with the RCB coring system. The top drive was then set back and the bit tripped from the hole, clearing the seafloor at 0355 h on 6 February. The bit was then tripped to the surface and cleared the rig floor at 1415 h, ending Hole U1431D. A total of 19 APC cores were taken over a 168.9 m interval in Hole U1431D, with a total recovery of 165.61 m of core. The XCB was used

48 times over an interval of 448.1 m, recovering 236.50 m of core. Overall core recovery for Hole U1431D was 402.11 m over an interval of 617.0 m (65.2%). The total time spent on Hole U1431D was 125.5 h.

After offsetting the vessel 20 m west of Hole U1431D, an RCB BHA was assembled with a new RCB C-4 bit. The BHA was run in the hole to 4163.22 mbrf, and the rig crew performed a slip and cut of 115 ft of drilling line. The remainder of the drill pipe was then run in the hole, and at 4221.46 mbrf, the top drive was picked up and then spaced out to spud Hole U1431E. A center bit was dropped and pumped to land out in the bit. Hole U1431E was spudded at 0650 h on 7 February. The seafloor depth for the hole was determined to be 4251.3 mbrf, calculated using an offset depth from Hole U1431D. Hole U1431E was advanced by drilling without coring from the seafloor to 507.0 mbsf. The center bit was pulled from the BHA by wireline and a core barrel was dropped to take a spot core (349-U1431E-2R) from 507.0 mbsf. After cutting the core without recovery, the center bit was dropped and drilling continued from 516.7 to 575.0 mbsf. The center bit was then retrieved by wireline, a core barrel dropped, and continuous coring started with Core 349-U1431E-4R from 575.0 mbsf. The next three cores (4R to 6R [575.0–603.3 mbsf]) did not recover any material. Coring continued with good recovery from Core 7R through 36R (603.3–894.3 mbsf). Core 36R was the first to recover basalt, with several small pieces present in the core catcher. Coring then continued into acoustic basement from Core 37R to 47R (894.3–991.4 mbsf). Penetration rates varied from 1.62 to 4.66 m/h over this interval, except for a sediment section in Core 45R that cored more quickly than the basalt. Microspheres were deployed in the RCB core catcher for Cores 12R through 43R.

With torque becoming higher and erratic, we decided to make a wiper trip to allow any debris collecting around the drill collars to fall into the hole. After pumping a sweep from the bottom of the hole, the drill string was pulled back to 862.95 mbsf. The bit was then run back to bottom, tagging fill material at 972.65 mbsf. With 18.75 m of fill in the bottom of the hole, a core barrel was dropped and the bit worked back to bottom with circulation and rotation without difficulty. The core barrel was retrieved with 0.65 m of material that was curated as ghost Core 48G. Another 50 bbl high-viscosity mud sweep was pumped after reaching 991.4 mbsf, and then another core barrel dropped. Coring continued from 991.4 mbsf to the final depth of 1008.8 mbsf (Cores 49R and 50R). Just prior to finishing coring, a 50 bbl high-viscosity mud sweep was pumped to clean and condition the hole for logging. The total depth of Hole U1431E was reached at 0740 h on 14 February. After reaching total depth, the final core was pulled to the surface and laid out. A total of 47 RCB cores were collected

in Hole U1431E over a 443.5 m interval, with a total recovery of 242.35 m of core (54.8% recovery, excluding the single 0.65 m long ghost core).

At the completion of coring, the rotary shifting tool (RST) was deployed to activate the mechanical bit release and the bit was dropped in the bottom of the hole. The RST was retrieved, and the other RST run in the hole to shift the sleeve back into the closed position. The end of the drill pipe was then raised to a depth of 4900.08 mbrf (648.78 mbsf) with the top drive in place. The hole was displaced from 648 mbsf to the seafloor with 11.4 ppg high-viscosity mud designed to improve logging conditions. The top drive was set back and the end of the pipe raised to 4400.9 mbrf (149.62 mbsf) for logging operations. After holding a logging safety meeting for rig floor personnel, the triple combo tool string was rigged up and run in the hole, reaching 463.7 m WSF on 15 February. The hole was then logged up, a short repeat pass recorded, and the tool string was then pulled to surface and rigged down. After rigging down the triple combo tool string, the FMS-sonic tool string was rigged up and deployed to 444 m WSF. Two full passes were made with the tool string, and then the tool string was pulled to the surface and rigged down at 1915 h on 15 February. The drill string was then tripped out of the hole from 4900.9 mbrf (149.6 mbsf) and cleared the seafloor at 2010 h. While pulling out of the hole with the drill string, the starboard conveyor on the pipe racker had a hydraulic failure. The hydraulic block in the derrickman's control booth was repaired, but 1.5 h was recorded as operational downtime. The rest of the trip out of the hole was uneventful and the bit cleared the rig floor at 0555 h. The rig floor was secured for transit at 0600 h on 16 February, ending operations at Site U1431. Total time spent in Hole U1431E was 231.75 h.

## Site U1432

The vessel arrived at Site U1432 (proposed Site SCS-6A) at 2337 h on 16 February 2014 after a 181 nmi transit at an average speed of 10.3 kt. An acoustic positioning beacon was deployed at 2352 h.

The primary objectives at this site required deep penetration, so the plan was to install a reentry cone and casing system, with the first step in this process to conduct a jet-in test to determine the length of 20 inch casing that should be attached to the reentry cone. The BHA for the jet-in test was assembled with an 18½ inch tricore bit and run to just above the seafloor. The vessel was offset 20 m south of the original coordinates for Site U1432 when the acoustic beacon landed within 6 m of the coordinates. The subsea camera and frame (VIT) was deployed to observe the bit tag the

seafloor (3840.0 mbrf). After picking up the top drive and spacing out the bit, Hole U1432A was spudded at 1525 h on 17 February. The BHA with the 18½ inch tricone bit was jetted into the formation 62.0 m over a 3 h period. The drill string was then pulled clear of the seafloor and the top drive set back. The remainder of the drill string was tripped out of the hole and the bit cleared the rotary table at 0205 h on 18 February, ending Hole U1432A. The total time spent in Hole U1432A was 26.5 h.

Based on the results from the jet-in test, a five-joint, 57.12 m long 20 inch casing string was selected. The 20 inch casing shoe joint was cut off to length and a Texas Pattern casing shoe welded on the end of the shoe joint. The remainder of the reentry cone and base were put together, moved into the moonpool, and positioned underneath the rotary table. The casing was run through the rotary table and the reentry cone in the moonpool. Each casing connection was tack welded to prevent the casing from backing out. The third joint of casing had to be replaced because of a damaged thread on the pin. The casing hanger and casing pup joint were picked up and attached to the top of the casing string. The Dril-Quip CADA (casing) running tool was made up into the casing hanger on the rig floor. The casing was then lowered through the rig floor, into the moonpool, and through the reentry cone. The casing hanger was landed into the landing ring inside the reentry cone and snapped into place inside the cone. The landing joint was lowered to release the weight of the casing. The casing running tool was rotated 3.75 turns to the right and the casing released. A BHA (casing stinger) with an 18½ inch bit, bit sub, and six drill collars was lowered into the reentry cone and casing. The casing running tool was inserted into this BHA and latched into the casing hanger in the reentry cone and secured by rotating the upper BHA 3.75 turns to the left. The moonpool doors were opened and the reentry system with the 20 inch casing was lowered through the moonpool to 3819 mbrf. The top drive was picked up and spaced out to jet-in the 20 inch casing. Hole U1432B was spudded at 0635 h on 19 February. Jetting continued as the casing was slowly lowered. Seven hours later the reentry system landed on the seafloor. The subsea camera was lowered to assist in releasing the casing. After attempting to release the casing for 2.5 h, the casing tool finally released after the vessel was offset from the original position in order to get the casing running tool to rotate. The rotation required to release the tool was observed clearly on the new subsea camera system. The camera was then pulled back to the surface and secured. The drill string was tripped back to the surface, and the BHA was set back in the derrick. During the trip out of the hole, the rig was secured to slip and cut 115 ft of drilling line as per the slip and cut program.

An HOC underreamer with an 11<sup>3</sup>/<sub>4</sub> inch closed diameter was made up to the 18<sup>1</sup>/<sub>2</sub> inch tricone bit and bit sub. The underreamer was set to open up the 18<sup>1</sup>/<sub>2</sub> inch hole to 22 inches in diameter. The underreamer and bit were lowered into the moonpool, the top drive picked up, and the underreamer function tested. The top drive was then set back, and the remainder of the BHA assembled and run in the hole to 3828.7 mbrf. During the trip, the subsea camera system was deployed. The bit was spaced out for reentry and the vessel was positioned using the subsea camera system. Hole U1432B was reentered at 2005 h on 20 February. After reentering the hole, the top drive was picked up and the drill string washed down to the casing shoe at 57.1 mbsf. After carefully washing down below the casing shoe so that the underreamer was below the base of the 20 inch casing, the pump rate and speed (rotations per minute [rpm]) were optimized for drilling a 22 inch hole below the 20 inch casing. Drilling continued to 4000.0 mbrf (160.0 mbsf). Drilling was suspended at 0610 h on 21 February when weather conditions worsened and the high heave of the vessel began to severely affect the weight on the bit and underreamer. The bit was tripped back inside the 20 inch casing and the top drive set back. The drill string was then tripped back to the surface, clearing the seafloor at 0835 h on 21 February, and finally clearing the rig floor at 1620 h. The underreamer and bit were inspected and laid out, and the BHA racked back into the derrick. While waiting on the weather to subside, the vessel offset 40 m south to be well away from the reentry cone for Hole U1432B. An APC hole (U1432C) was cored and, after coring to 110.0 mbsf, the weather appeared to have subsided sufficiently for another attempt at drilling out the 22 inch hole for the 16 inch casing.

After pulling out of Hole U1432B, the upper guide horn was picked up from the drill collar rack, lifted to the rig floor, and reinstalled below the rotary table. An APC/XCB BHA was made up while the vessel was offset 40 m south of Hole U1432B. The drill string was then tripped toward the seafloor. After completing the pipe trip to just above the seafloor, the top drive was picked up and spaced out, and Hole U1432C was spudded at 0555 h on 22 February. The first coring attempt with the bit at 3835 mbrf did not recover any core. The bit was then lowered to 3838.5 mbrf and the next coring attempt recovered a mudline core of 7.95 m of sediment. This core length was used to calculate the seafloor depth at 3840.1 mbrf (3829.1 mbsl). Nonmagnetic core barrels were used for the APC from Core 329-U1432C-1H through 12H to a final depth of 110.0 mbsf. PFT fluid was displaced into the drill string prior to spudding the hole and was pumped continuously during Hole U1432C. Temperature measurements were taken with the APCT-3 on Cores 5H, 7H, 9H, and 11H with good results. The hole was terminated when weather conditions improved sufficiently to return to Hole U1432B. The bit was tripped to the surface and cleared the rig floor at 0735 h, ending

Hole U1432C. A total of 12 APC cores were taken over a 110.0 m interval in Hole U1432C, recovering 88.74 m of core (80.7% recovery). The total time spent in Hole U1432C was 39.25 h.

After tripping out of Hole U1432C, the BHA was set back in the derrick and the upper guide horn removed and laid out on the drill collar racks. We then returned to Hole U1432B to continue drilling the 22 inch hole for the 16 inch casing. As before, an HOC underreamer with an 11¾ inch closed diameter was made up to the 18½ inch tricone bit and bit sub. The underreamer was set to open up the 18½ inch hole to a 22 inch diameter. The underreamer and bit were lowered into the moonpool, the top drive picked up, and the underreamer function tested. The top drive was set back, and the remainder of the BHA assembled and run in the hole to 3828.7 mbrf. During the trip, the subsea camera system was deployed. The bit was spaced out for reentry and Hole U1432B reentered at 1944 h on 23 February. The subsea camera system was pulled back to surface while the top drive was picked up. The bit and underreamer were run in the hole to 160.0 mbsf and drilling continued from 4000 to 4090.0 mbrf (160.0–250.0 mbsf). The depth of Hole U1432B reached 250 mbsf at 0640 h on 24 February. The hole was conditioned and displaced with 379 bbl of 10.5 ppg mud. The drill string was tripped back to the surface and cleared the rig floor at 2120 h. During the trip out of the hole, the rig was secured to slip and cut 115 ft of drilling line as per the slip and cut program.

The drill floor was rigged up to run 16 inch casing. We assembled 240.85 m of 16 inch casing, including a Dril-Quip casing hanger. The casing was landed on the moonpool doors with the casing running tool, which was then released and pulled back through the rig floor. The 240.77 m casing stinger was made up to the bottom of the casing hanger running tool and lowered through the 16 inch casing in the moonpool. The casing hanger running tool with the casing stinger below was latched into the 16 inch casing hanger, with two control length drill collars and a tapered drill collar above the casing running tool. The entire casing string plus running tools were lowered to 3827.4 mbrf while filling the drill pipe with water every 20 stands. The subsea camera system was installed and lowered to reenter Hole U1432B. After 15 min of maneuvering the vessel, we reentered Hole U1432B at 0500 h on 26 February. The camera system was pulled back to the surface while the top drive was picked up. The casing was lowered into the 22 inch hole and washed down to ~200 mbsf. The subsea camera system was again lowered to assist in releasing the casing running tool from the casing. As the camera system neared the seafloor, the video feed from the subsea camera was lost. The camera system was pulled back to the surface for repair (water had intruded

the pan and tilt unit, causing a power overload in the system). The casing was washed in to 240.9 mbsf and landed in the reentry cone. The casing running tool was rotated clockwise 3.75 turns and released from the casing hanger. The BHA, including the internal casing stinger, was pulled back ~11 m and the top drive set back. The cementing assembly was rigged up, the lines were pressure tested, and ~20 bbl of cement mixed to 15 ppg was pumped downhole. The cement was displaced with seawater and positioned to balance at the casing shoe to an estimated height of 17 m above the casing shoe (both inside and outside the casing). The cementing equipment was rigged down and the drill string pulled back to 161.9 mbsf. The circulating head was connected and the drill string flushed with twice the drill string capacity with seawater. The remainder of the drill string was pulled from the hole, clearing the seafloor at 2140 h on 26 February and finally clearing the rig floor at 0400 h on 27 February. The BHA components were secured and the running tool was detorqued.

A new 14 $\frac{3}{4}$  inch bit and four stands of drill collars were made up and run in the hole with drill pipe while filling with water at 20-stand intervals. When the bit was at 3823.3 mbrf, the subsea camera system was lowered to allow reentry. Hole U1432B was reentered at 1655 h on 27 February, and the camera pulled back to the surface. After securing the camera system, the drill string was run in the hole until the top of the cement was tagged at 4069.0 mbrf (229 mbsf). The cement was drilled out from 4069.0 to 4083.0 mbrf (229.0–243.0 mbsf). After washing down to total depth (250.0 mbsf), new 14 $\frac{3}{4}$  inch hole was drilled from 4090.0 to 4640.0 mbrf (250.0–800.0 mbsf). After reaching 800.0 mbsf, the hole was swept clean with high-viscosity mud. After setting back the top drive, the drill string was pulled back to the surface. The bit cleared the rotary table at 1120 h on 1 March. The 10 $\frac{3}{4}$  inch casing stinger components were made up and the underreamer arms were set to 12 $\frac{3}{4}$  inches. The top drive was then picked up and the mud motor and underreamer tested. After the test was successfully completed, they were racked back in the derrick. After assembling all the casing stinger components, a slip and cut of the drilling line was completed.

The rig floor was then prepared for running 10 $\frac{3}{4}$  inch casing, and 787.06 m of casing with a 10 $\frac{3}{4}$  inch casing hanger were made up. The casing was lowered into the moon-pool and secured with a casing elevator on the prepared landing platform. The buoyant weight of the casing string was 70,000 lb. The running tool was released from the casing and pulled back to the rig floor. It was then made up to the bottom of a drill collar stand and racked back in the derrick. The casing stinger with the bit, underreamer, and mud motor were then run inside the casing. Also included in the stinger were three stands of drill collars and 24 stands of drill pipe. The bit and underreamer

were positioned just below the bottom of the casing after the running tool was landed and made up to the casing. The casing was run to the seafloor with drill pipe and the subsea camera system deployed to assist with the reentry at the seafloor. Hole U1432B was reentered at 0242 h on 3 March. The camera system was pulled back to the surface and set back into the storage position on the moonpool doors. The casing was run in the hole with drill pipe to 223.5 mbsf. The top drive was picked up and the casing lowered to 244.0 mbsf. The casing was washed to the bottom while pumping 530 gpm. At 530 gpm, the mud motor was turning the bit at 80–85 rpm with the under-reamer arms extended to clear a 12¾ inch hole in front of the casing. The casing was steadily lowered until it was landed and released at 1745 h on 3 March. The top drive was set back and the drill string tripped from the hole, clearing the seafloor at 2045 h, and then clearing the rotary table at 0915 h on 4 March. The casing stinger components were flushed with freshwater and either laid out or, in the case of the drill collars, racked back in the derrick.

After successfully running the 10¾ inch casing, a cementing stinger was assembled. The stinger consisted of a reentry/cleanout bit, a bit sub, a stand of drill collars, 24 stands of 5 inch drill pipe, F-cup tester, another two drill collars, a tapered drill collar, and two stands of 5½ inch transition drill pipe. The entire assembly was made up and run in the hole with drill pipe to just above the seafloor while stopping every 20 stands to fill the drill pipe with water. The subsea camera system was deployed to just above the seafloor and Hole U1432B reentered at 0344 h on 5 March. The camera system was pulled back to the surface and secured. The bit was run in the hole to 767 mbsf, 20 m above the 10¾ inch casing shoe. The F-cup tester was spaced out so that it was at 42 mbsf, inside the 16 inch casing. The circulating head was made up to the top of the drill string and the mud pumps were brought up to 60 spm to verify circulation up the annulus between the hole and the casing. After establishing circulation, the cement pump was used to pump 10 bbl of freshwater ahead of the cement slurry. Fourteen barrels of 15.5 ppg cement were then mixed and pumped downhole, followed by another 10 bbl of freshwater. This was displaced down the drill string with 263 bbl of saltwater using the mud pumps. After displacing the cement, the circulating head was removed and the driller attempted to pull out of the hole. He immediately noticed a steadily increasing overpull as he tried to pull out of the hole. After pulling up enough to remove two singles of drill pipe, we were unable to raise the drill string any further. It now appears that the formation collapsed around the 10¾ inch casing string, preventing circulation up the open hole annulus and outside the casing. Instead, the circulation path was up through the 10¾ casing, bypassing the cup tester. The elevated temperatures at 700 mbsf (~65°–70°C) accelerated the hardening of the

cement. The drill string was worked for the next 9 h using combinations of overpull, torque, and pump pressure in an effort to free the drill string. At that point, we rigged up to sever the drill string. The drill string severing charge was lowered to just above the cup tester, which has a 1.5 inch internal diameter. The charge was detonated at 0430 h on 6 March 2014; however, there was no loss of overpull on the pipe. The wireline was pulled out of the hole and the severing tool cleared the rig floor at 0808 h. The drill pipe was worked with a maximum of 100,000 lb of overpull for ~1 h. The elevators were then lowered back to the elevator stool while the rig was offset 200 m. The top drive was picked up and the drill pipe was picked up slowly while moving the rig back to the original location. The pipe was worked free with a maximum of 400 A of torque and 40,000 lb of overpull. The end of pipe cleared the casing hanger at 1105 h. The top drive was set back and the drill string pulled from the hole. The end of pipe cleared the rotary table at 1830 h. The acoustic positioning beacon was recovered while tripping drill pipe. The upper guide horn was reinstalled, the rig floor secured for transit, and the thrusters raised. The vessel switched to transit mode at 2036 h on 6 March, ending Site U1432. The total time spent on Hole U1432B was 363.25 h (15.1 days).

## Site U1433

After a 334 nmi transit lasting 29.9 h, the vessel arrived at Site U1433 (proposed Site SCS-4B) and switched into dynamic positioning mode at 0230 h on 8 March 2014. At 0255 h, an acoustic positioning beacon was deployed. An APC/XCB BHA was assembled and run in the hole to 800.4 mbrf. At 0520 h, a tool joint parted on the twenty-fourth stand of drill pipe, just after picking up the drill string and just prior to unlatching the lower set of elevators. The load cell weight at the time of the incident was recorded at ~200,000 lb. The entire weight of the drill string dropped ~18 inches and landed in the lower set of elevators, which were resting on top of the dual elevator stool. The pin on the top single of drill pipe had parted, leaving one single hanging from the upper set of elevators and two singles sticking up from on top of the lower set of elevators. The stand was then laid out to the V-door. The broken pipe was visually inspected and photographed. As a precaution, the twenty-third stand was also disassembled and laid out. The bottom set of elevators was removed from use and replaced with a reconditioned set of elevators. After clearing the rig floor, the trip in the hole resumed. When the bit was at 1147.8 mbrf, another tool joint failed when the driller was picking up the thirty-sixth stand from the pipe racker. This time, one single fell back into the trough of the pipe racker still attached to the skate, and a double

remained connected to the elevators on the bales connected to the main block. After the second tool joint failure, we decided to discontinue using any of the 5 inch drill pipe that had been used in the stuck pipe incident at the previous site. Investigations continue into the root cause of the pipe failure. Documentation of the stuck pipe event was collected for analysis. The failed tool joints were prepared with care for shipment to a laboratory for detailed metallurgical analysis and were shipped from Keelung, Taiwan, at the end of the expedition. The drill string was tripped back to the BHA and all suspect drill pipe was removed from use and stored in the port pipe racker. We picked up 201 joints of new 5 inch drill pipe from the riser hold. The new drill pipe was strapped and drifted as it was assembled and lowered toward the sea-floor. After completing assembly of the new pipe, the remaining 37 stands from the starboard 5 inch pipe racker were picked up and run in the hole. The total number of 5 inch pipe stands available was then 104 stands. The remaining 101 stands of suspect drill pipe in the port pipe racker need to be inspected before they can be put back in service.

After running in the hole with 104 stands of 5 inch drill pipe, the 5½ inch drill pipe was picked up until the bit reached 4372.9 mbrf. The trip in the hole was stopped at 3587.0 mbrf to perform a slip and cut of the drilling line. The PDR recorded an estimated depth of 4394.4 mbrf for the seafloor. The top drive was picked up and spaced out to 4390 mbrf. The nonmagnetic core barrels were dressed with liners, the FlexIT core orientation tool was inserted, and a core barrel run down and landed. Hole U1433A was spudded at 1000 h on 9 March. The mudline core recovered 8.9 m of sediment and the seafloor was calculated to be 4390.6 mbrf (4379.4 mbsl). Coring continued without issue through Core 349-U1433A-16H (151.4 mbsf). While running in the hole with a core barrel, the bridge informed the driller that a fishing boat was drifting toward the vessel's location. At 0540 h on 10 March, the Captain ordered the driller to suspend operations. The core barrel was retrieved, and the driller began tripping out of the hole with the top drive. At 99.1 mbsf, the driller was instructed to standby. After the threat disappeared, the drill string was tripped back to bottom and coring continued to Core 20H (188.3 mbsf). After four consecutive partial strokes of the APC, refusal was called at 188.3 mbsf. Orientation was measured on all APC cores. Temperature measurements were taken with the APCT-3 on Cores 4H, 7H, 10H, and 13H with good results. PFT fluid was used on Cores 18H through 20H. The bit was tripped to the surface and cleared the rig floor at 0325 h on 11 March, ending Hole U1433A. A total of 20 APC cores were taken over a 188.3 m interval in Hole U1433A, recovering 168.79 m of core (89.6%). The total time spent on Hole U1433A was 73.0 h.

After offsetting the vessel 20 m east of Hole U1433A, an RCB BHA was assembled with a new RCB C-4 bit. Three additional drill collars had to be picked up from the drill collar racks to replace the ones lost in Hole U1432B. The core barrels were spaced out at the surface and the 172.07 m BHA assembled and run in the hole to 4350.3 mbrf. The top drive was then picked up and spaced out to spud Hole U1433B. A center bit was dropped and pumped to land out in the bit. Hole U1433B was spudded at 1515 h on 11 March. The seafloor depth for the hole was 4390.6 mbrf (4379.4 mbsl), determined by using an offset depth from Hole U1433A. Hole U1433B was advanced by drilling without coring from the seafloor to 186.1 mbsf. The center bit was pulled from the BHA by wireline and a core barrel dropped to start continuous RCB coring from Core 349-U1433B-2R through 75R to a total depth of 5249.1 mbrf (858.5 mbsf). The PFT pumps were turned on during the drilldown period, and PFT fluid was pumped through Core 26R (426.9 mbsf). Microspheres were added to the RCB core catcher for Cores 56R to 75R. Core 65R encountered basalt at 786.3 mbsf. Coring continued into acoustic basement from Core 65R to Core 75R (858.5 mbsf), with half-cores collected from Core 67R to the total depth in an attempt to improve recovery. Penetration rates varied from 0.9 to 3.9 m/h over the basement interval. The total depth of Hole U1433B was reached at 2100 h on 17 March and the final core was pulled to the surface and laid out. At the completion of coring Hole U1433B, 74 RCB cores had been cut over a 672.4 m interval, recovering 443.04 m of core (65.9%).

After pumping a 50 bbl high-viscosity mud sweep, a short wiper trip was made from total depth to just above the basement contact (786.3 mbsf) with the top drive installed. While tripping back to bottom, the hole had to be reamed from 847.4 to 858.5 mbsf. We then pumped another 50 bbl mud sweep to further clean the hole. The RST was then picked up and run into the hole with a coring line to release the bit for logging. An attempt was made to engage the sleeve in the mechanical bit release. After being unable to engage the shifting sleeve, the RST was pulled back to surface. Examination at the surface revealed the RST did not come back with the core line sinker bars. An overshot (fishing tool) was made up and run in the hole to fish for the RST. After securing the RST, the mechanical bit release sleeve was engaged and the bit was dropped from the drill string. The RST also dropped off the fishing tool on release, leaving the RST in the bottom of the hole. The core line was pulled back to surface and the RST to shift the sleeve back into the original position was deployed. With the bit released, the drill string was raised to 5196.3 mbrf (805.7 mbsf) with the top drive. The top drive was then set back and the drill string raised to 5079.7 mbrf (689.1 mbsf). The circulating head was picked up and the hole displaced from 689.1 mbsf to the seafloor with 10.5 ppg high-viscosity mud designed to improve logging conditions. The

drill string was then raised up and spaced out so that the end of the pipe was at 4490.7 mbrf (100.1 mbsf) for logging operations.

After holding a logging safety meeting for rig floor personnel, the triple combo tool string was rigged up and deployed. The tool string reached a total depth of 845.4 m WSF on 18 March. The hole was then logged up and the tool string pulled to surface and rigged down. After rigging down the triple combo tool string, the FMS-sonic tool string was rigged up and deployed to a depth of 842.4 m WSF. The basement section of the hole was logged five times with three passes with the calipers open. On the last pass, the tool become stuck but was eventually worked free. The rest of the open hole was logged up to the end of the drill pipe and the tool string was then pulled to the surface and rigged down. All logging equipment was rigged down by 1300 h on 19 March. The drill string was pulled from the hole and the BHA set back and secured for transit at 2300 h on 19 March, ending Site U1433. Total time spent in Hole U1433B was 211.5 h.

## Site U1434

After an 18 nmi transit lasting 2 h, the vessel arrived at Site U1434 (proposed Site SCS-4E) and switched into dynamic positioning mode at 0048 h on 20 March 2014. At 0110 h, an acoustic positioning beacon was deployed. An RCB BHA was assembled with a new RCB C-7 bit. The core barrels were spaced out at the surface and the 172.07 m BHA assembled. The BHA was lowered to 4000.9 mbrf and the top drive picked up and spaced out to 4020.0 mbrf to spud Hole U1434A. A center bit was dropped and pumped down the drill string to land out in the bit. Hole U1434A was spudded at 1215 h on 20 March. The estimated depth of the seafloor was determined to be 4020.4 mbrf using the PDR. The final seafloor depth for the hole was 4020.4 mbrf (4009.0 mbsl), which was determined by tagging the seafloor with the drill bit. Hole U1434A was advanced by drilling without coring from the seafloor to 4217.4 mbrf (197.0 mbsf) over a 10 h period. The center bit was pulled and a core barrel dropped to start continuous RCB coring from Core 349-U1434A-2R. Coring continued through Core 15R to a depth of 4332.9 mbrf (312.5 mbsf). Microspheres were deployed in each RCB core catcher for the duration of RCB coring. We encountered the sediment/basement interface in Core 10R, with the formation change at ~280 mbsf. Coring continued into acoustic basement from Core 10R through 15R to a total depth of 4332.9 mbrf (312.5 mbsf). Half cores were started with Core 12R and continued to total depth. Penetration rates varied from 1.57 to 5.76 m/h over the basement interval. Coring was finally halted because of poor core recovery coupled with high torque and poor

coring conditions. The total depth of Hole U1434A was reached at 0925 h on 22 March. After reaching total depth, the final core was pulled to the surface and laid out. At the completion of coring Hole U1434A, 14 RCB cores had been cut over a 115.5 m interval, recovering 26.43 m of core (22.9%).

After retrieving the final core, we attempted to pull the drill string from the hole; however, the high torque and high overpull made this impossible. After 1.5 h of working the pipe with a combination of high torque (900 A), overpull, and constant pumping action, the drill string came free and was pulled out of the hole with the top drive to 4117.4 mbrf (97.0 mbsf). The top drive was then set back and the drill string was tripped to the surface. The bit cleared the seafloor at 1500 h, and then cleared the rotary table at 2300 h. After securing the rig floor for transit and pulling the hydrophones and thrusters, the vessel switched to cruise mode and began the transit to Site U1435 at 2348 h on 22 March. Total time spent on Hole U1434A was 71.0 h.

## Site U1435

After a 336 nmi transit lasting 39.65 h, the vessel arrived at Site U1435 (proposed Site SCS-6C) and switched into dynamic positioning mode at 1524 h on 24 March 2014. At 2045 h, an acoustic positioning beacon was deployed. An RCB BHA was assembled with a new RCB C-7 bit. The core barrels were spaced out at the surface and the 172.07 m BHA assembled. The BHA was then run in the hole to 3214.9 mbrf and the top drive picked up and spaced out to 3261.6 mbrf to spud Hole U1435A. While lowering the drill pipe, we conducted a sonar survey with the 3.5 kHz array sonar to select a hole location to maximize sediment thickness. Hole U1435A was spudded at 0035 h on 25 March. The estimated depth of the seafloor was 3261.6 mbrf using the PDR. The final seafloor depth for the hole was 3264.0 mbrf (3252.5 mbsl), which was determined by tagging the seafloor with the drill bit. We advanced Hole U1435A by coring from the seafloor to 3564.0 mbrf (300.0 mbsf). Microspheres were deployed in each RCB core catcher from Core 349-U1435A-5R to the total depth of the hole. Coring continued to Core 349-U1435A-32R (300 mbsf), when operational time for the expedition expired. Penetration rates varied from 2.8 to 58.2 m/h over the cored interval. The total depth of Hole U1435A was reached at 0730 h on 27 March. After reaching total depth, the final core was pulled to the surface and laid out. At the completion of coring Hole U1435A, 32 RCB cores had been cut over a 300.0 m interval, recovering 171.37 m of core (57.1%).

After reaching total depth and laying out the last core, the drill string was pulled out of the hole with the top drive to 3535.1 mbrf (271.1 mbsf). The drilling knobbies were laid out, the top drive set back, and the drill string tripped to the surface. The bit cleared the seafloor at 1020 h, and then cleared the rotary table at 1835 h. After securing the rig floor for transit and pulling the hydrophones and thrusters, the vessel switched to cruise mode and began the transit to Keelung, Taiwan, at 1900 h on 27 March. Total time spent on Hole U1435A was 75.5 h. Expedition 349 officially ended with the first line ashore in Keelung at 0710 h on 30 March.

## References

- Barckhausen, U., Engels, M., Franke, D., Ladage, S., and Pubellier, M., in press. Evolution of the South China Sea: revised ages for breakup and seafloor spreading. *Marine and Petroleum Geology*. <http://dx.doi.org/10.1016/j.marpetgeo.2014.02.022>
- Barckhausen, U., and Roeser, H.A., 2004. Seafloor spreading anomalies in the South China Sea revisited. In Clift, P., Wang, P., Kuhnt, W., and Hayes, D. (Eds.), *Continent-Ocean Interactions within East Asian Marginal Seas*. Geophysical Monograph, 149:121–125. <http://dx.doi.org/10.1029/149GM07>
- Bleil, U., and Petersen, N., 1983. Variations in magnetization intensity and low-temperature titanomagnetite oxidation of ocean floor basalts. *Nature*, 301(5899):384–388. <http://dx.doi.org/10.1038/301384a0>
- Braitenberg, C., Wienecke, S., and Wang, Y., 2006. Basement structures from satellite-derived gravity field: South China Sea ridge. *Journal of Geophysical Research: Solid Earth*, 111(B5):B05407. <http://dx.doi.org/10.1029/2005JB003938>
- Briaux, A., Patriat, P., and Tapponnier, P., 1993. Updated interpretation of magnetic anomalies and seafloor spreading stages in the South China Sea: implications for the Tertiary tectonics of Southeast Asia. *Journal of Geophysical Research: Solid Earth*, 98(B4):6299–6328. <http://dx.doi.org/10.1029/92JB02280>
- Bryant, W.R., and Bennett, R.H., 1988. Origin, physical, and mineralogical nature of red clays: the Pacific Ocean Basin as a model. *Geo-Marine Letters*, 8(4):189–249. [doi:10.1007/BF02281640](http://dx.doi.org/10.1007/BF02281640)
- Castillo, P.R., Carlson, R.W., and Batiza, R., 1991. Origin of Nauru Basin igneous complex: Sr, Nd, and Pb isotope and REE constraints. *Earth and Planetary Science Letters*, 103(1–4):200–213. [http://dx.doi.org/10.1016/0012-821X\(91\)90161-A](http://dx.doi.org/10.1016/0012-821X(91)90161-A)
- Chung, S.-L., Sun, S., Tu, K., Chen, C.-H., and Lee, C., 1994. Late Cenozoic basaltic volcanism around the Taiwan Strait, SE China: product of lithosphere-asthenosphere interaction during continental extension. *Chemical Geology*, 112(1–2):1–20. [http://dx.doi.org/10.1016/0009-2541\(94\)90101-5](http://dx.doi.org/10.1016/0009-2541(94)90101-5)
- Clift, P., Lee, G.H., Duc, N.A., Barckhausen, U., Long, H.V., and Zhen, S., 2008. Seismic reflection evidence for a Dangerous Grounds miniplate: no extrusion origin for the South China Sea. *Tectonics*, 27(3):TC3008. <http://dx.doi.org/10.1029/2007TC002216>
- Clift, P.D., and Sun, Z., 2006. The sedimentary and tectonic evolution of the Yinggehai-Song Hong Basin and the southern Hainan margin, South China Sea: implications for Tibetan

- uplift and monsoon intensification. *Journal of Geophysical Research: Solid Earth*, 111(B6):B06405. <http://dx.doi.org/10.1029/2005JB004048>
- Cullen, A., Reemst, P., Henstra, G., Gozzard, S., and Ray A., 2010. Rifting of the South China Sea: new perspectives. *Petroleum Geoscience*, 16(3):273–282. <http://dx.doi.org/10.1144/1354-079309-908>
- Cullen, A.B., 2010. Transverse segmentation of the Baram-Balabac Basin, NW Borneo: refining the model of Borneo's tectonic evolution. *Petroleum Geoscience*, 16(1):3–29. <http://dx.doi.org/10.1144/1354-079309-828>
- Dyment, J., and Arkani-Hamed, J., 1995. Spreading-rate-dependent magnetization of the oceanic lithosphere inferred from the anomalous skewness of marine magnetic anomalies. *Geophysical Journal International*, 121(3):789–804. <http://dx.doi.org/10.1111/j.1365-246X.1995.tb06439.x>
- Dyment, J., Arkani-Hamed, J., and Ghods, A., 1997. Contribution of serpentinized ultramafics to marine magnetic anomalies at slow and intermediate spreading centres: insights from the shape of the anomalies. *Geophysical Journal International*, 129(3):691–701. <http://dx.doi.org/10.1111/j.1365-246X.1997.tb04504.x>
- Fan, W., and Menzies, M., 1992. Destruction of aged lower lithosphere and accretion of asthenosphere mantle beneath eastern China. *Geotectonics and Metallogeny*, 16:171–180.
- Fedo, C.M., Sircombe, K.N., and Rainbird, R.H., 2003. Detrital zircon analysis of the sedimentary record. In Hanchar, J.M., and Hoskin, P.W.O. (Eds.), *Zircon*. Reviews in Mineralogy and Geochemistry, 53(1):277–303. <http://dx.doi.org/10.2113/0530277>
- Flower, M.F.J., Russo, R.M., Tamaki, K., and Hoang, N., 2001. Mantle contamination and the Izu-Bonin-Mariana (IBM) “high-tide mark”: evidence for mantle extrusion caused by Tethyan closure. *Tectonophysics*, 333(1–2):9–34. [http://dx.doi.org/10.1016/S0040-1951\(00\)00264-X](http://dx.doi.org/10.1016/S0040-1951(00)00264-X)
- Franke, D., Barckhausen, U., Baristead, N., Engels, M., Ladage, S., Lutz, R., Montano, J., Pellejera, N., Ramos, E.G., and Schnabel, M., 2011. The continent–ocean transition at the southeastern margin of the South China Sea. *Marine and Petroleum Geology*, 28(6):1187–1204. <http://dx.doi.org/10.1016/j.marpetgeo.2011.01.004>
- Gilley, L.D., Harrison, T.M., Leloup, P.H., Ryerson, F.J., Lovera, O.M., and Wang, J.-H., 2003. Direct dating of left-lateral deformation along the Red River shear zone, China and Vietnam. *Journal of Geophysical Research: Solid Earth*, 108(B2):2127. <http://dx.doi.org/10.1029/2001JB001726>
- Goldstein, S.J., 1995. Uranium-series chronology of subsurface basalts, 9°31'N East Pacific Rise. In Batiza, R., Storms, M.A., and Allan, J.F. (Eds.), 1995. *Proceedings of the Ocean Drilling Program, Scientific Results*, 142: College Station, TX (Ocean Drilling Program), 37–39. <http://dx.doi.org/10.2973/odp.proc.sr.142.115.1995>
- Goldstein, S.J., Murrell, M.T., Janecky, D.R., Delaney, J.R., and Clague, D.A., 1991. Geochronology and petrogenesis of MORB from the Juan de Fuca and Gorda Ridges by <sup>238</sup>U–<sup>230</sup>Th disequilibrium. *Earth and Planetary Science Letters*, 107(1):25–41. [http://dx.doi.org/10.1016/0012-821X\(91\)90041-F](http://dx.doi.org/10.1016/0012-821X(91)90041-F)
- Goldstein, S.J., Perfit, M.R., Batiza, R., Fornari, D.J., and Murrell, M.T., 1994. Off-axis volcanism at the East Pacific Rise detected by uranium-series dating of basalts. *Nature*, 367(6459):157–159. <http://dx.doi.org/10.1038/367157a0>
- Grimes, C.B., John, B.E., Kelemen, P.B., Mazdab, F.K., Wooden, J.L., Cheadle, M.J., Hanghøj, K., and Schwartz, J.J., 2007. Trace element chemistry of zircons from oceanic crust: a method for distinguishing detrital zircon provenance. *Geology*, 35(7):643–646. <http://dx.doi.org/10.1130/G23603A.1>

- Haile, N.S., 1973. The recognition of former subduction zones in Southeast Asia. In Tarling, D.H., and Runcorn, S.K., (Eds.), *Implications of Continental Drift to the Earth Sciences*, Vol. 2: London (Academic Press), 885–892.
- Hall, R., 1996. Reconstructing Cenozoic SE Asia. In Hall, R., and Blundell, D.J. (Eds.), *Tectonic Evolution of Southeast Asia*. Geological Society Special Publication, 106(1):153–184. <http://dx.doi.org/10.1144/GSL.SP.1996.106.01.11>
- Hall, R., 2002. Cenozoic geological and plate tectonic evolution of SE Asia and the SW Pacific: computer-based reconstructions, model and animations. *Journal of Asian Earth Sciences*, 20(4):353–431. [http://dx.doi.org/10.1016/S1367-9120\(01\)00069-4](http://dx.doi.org/10.1016/S1367-9120(01)00069-4)
- Hall, R., and Morley, C.K., 2004. Sundaland basins. In Clift, P.D., Kuhnt, W., Wang, P., and Hayes, D. (Eds.), *Continent-Ocean Interactions with East Asian Marginal Seas*. Geophysical Monograph, 149:55–85. <http://dx.doi.org/10.1029/149GM04>
- Hamilton, W.B., 1979. Tectonics of the Indonesian Region. *U.S. Geol. Surv. Prof. Pap.*, 1078.
- Hayes, D.E., and Nissen, S.S., 2005. The South China Sea margins: implications for rifting contrasts. *Earth and Planetary Science Letters*, 237(3–4):601–616. <http://dx.doi.org/10.1016/j.epsl.2005.06.017>
- Hayes, D.E., Nissen, S.S., Buhl, P., Diebold, J., Bochu, Y., Weijun, Z., and Yongqin, C., 1995. Throughgoing crustal faults along the northern margin of the South China Sea and their role in crustal extension. *Journal of Geophysical Research: Solid Earth*, 100(B11):22435–22446. <http://dx.doi.org/10.1029/95JB01867>
- Hékinian, R., Bonté, P., Pautot, G., Jacques, D., Labeyrie, L.D., Mikkelsen, N., and Reyss, J.-L., 1989. Volcanics from the South China Sea ridge system. *Oceanologica Acta*, 12(2):101–115.
- Hilde, T., Uyeda, S., and Kroenke, L., 1977. Evolution of the western Pacific and its margin. *Tectonophysics*, 38(1–2):145–165. [http://dx.doi.org/10.1016/0040-1951\(77\)90205-0](http://dx.doi.org/10.1016/0040-1951(77)90205-0)
- Holloway, N.H., 1982. North Palawan Block, Philippines: its relation to the Asian mainland and role in evolution of South China Sea. *AAPG Bulletin*, 66(9):1355–1383. <http://aapg-bull.geoscienceworld.org/content/66/9/1355.abstract>
- Honza, E., 1995. Spreading mode of backarc basins in the western Pacific. *Tectonophysics*, 251(1–4):139–152. [http://dx.doi.org/10.1016/0040-1951\(95\)00054-2](http://dx.doi.org/10.1016/0040-1951(95)00054-2)
- Huang, C.-Y., Xia, K., Yuan, P.B., and Chen, P.-G., 2001. Structural evolution from Paleogene extension to latest Miocene–recent arc-continent collision offshore Taiwan: comparison with on land geology. *Journal of Asian Earth Sciences*, 19(5):619–639. [http://dx.doi.org/10.1016/S1367-9120\(00\)00065-1](http://dx.doi.org/10.1016/S1367-9120(00)00065-1)
- Hutchison, C.S., 1996. The “Rajang accretionary prism” and “Lupar Line” problem of Borneo. In Hall, R., and Blundell, D.J. (Eds.), *Tectonic Evolution of Southeast Asia*. Geological Society Special Publication, 106(1):247–261. <http://dx.doi.org/10.1144/GSL.SP.1996.106.01.16>
- Hutchison, C.S., 2004. Marginal basin evolution: the southern South China Sea. *Marine and Petroleum Geology*, 21(9):1129–1148. <http://dx.doi.org/10.1016/j.marpetgeo.2004.07.002>
- Hutchison, C.S., 2005. *Geology of North-West Borneo*: Amsterdam (Elsevier B.V.). <http://www.sciencedirect.com/science/book/9780444519986>
- Ishihara, T., and Kisimoto, K., 1996. Magnetic anomaly map of East Asia, 1:4,000,000 (CD-ROM version). Geological Survey of Japan, Coordinating Committee for Coastal and Off-shore Geoscience Programs in East and Southeast Asia (CCOP).
- Jahn, B.-M., Chen, P.Y., and Yen, T.P., 1976. Rb-Sr ages of granitic rocks in southeastern China and their tectonic significance. *Geological Society of America Bulletin*, 87(5):763–776. [http://dx.doi.org/10.1130/0016-7606\(1976\)87<763:RAOGRI>2.0.CO;2](http://dx.doi.org/10.1130/0016-7606(1976)87<763:RAOGRI>2.0.CO;2)

- Jin, Z., Xu, S., and Li, Z., 2002. Inversion of heterogeneous magnetism for seamounts in the South China Sea. *Journal of Ocean University of Qingdao* (English Edition), 32:926–934. (in Chinese)
- Koppers, A.A.P., Russell, J.A., Roberts, J., Jackson, M.G., Konter, J.G., Wright, D.J., Staudigel, H., and Hart, S.R., 2011. Age systematics of two young en echelon Samoan volcanic trails. *Geochemistry, Geophysics, Geosystems*, 12(7):Q07025. <http://dx.doi.org/10.1029/2010GC003438>
- Lacassin, R., Maluski, H., Leloup, P.H., Tapponnier, P., Hinthong, C., Siribhakdi, K., Chuaviroj, S., and Charoenravat, A., 1997. Tertiary diachronic extrusion and deformation of western Indochina: structural and  $^{40}\text{Ar}/^{39}\text{Ar}$  evidence from NW Thailand. *Journal of Geophysical Research: Solid Earth*, 102(B5):10013–10037. <http://dx.doi.org/10.1029/96JB03831>
- Lallemand, S., and Jolivet, L., 1986. Japan Sea: a pull apart basin? *Earth and Planetary Science Letters*, 76(3–4):375–389. [http://dx.doi.org/10.1016/0012-821X\(86\)90088-9](http://dx.doi.org/10.1016/0012-821X(86)90088-9)
- Le Maitre, R.W., Bateman, P., Dudek, A., Keller, J., Lameyre, J., Le Bas, M.J., Sabine, P.A., Schmid, R., Sorensen, H., Streckeisen, A., Woolley, A.R., and Zanettin, B., 1989. *A Classification of Igneous Rocks and Glossary of Terms*: Oxford (Blackwell).
- Lee, T.-Y., and Lawver, L.A., 1995. Cenozoic plate reconstruction of Southeast Asia. *Tectonophysics*, 251(1–4): 85–138. [http://dx.doi.org/10.1016/0040-1951\(95\)00023-2](http://dx.doi.org/10.1016/0040-1951(95)00023-2)
- Leloup, P.H., Arnaud, N., Lacassin, R., Kienast, J.R., Harrison, T.M., Trong, T.T.P., Replumaz, A., and Tapponnier, P., 2001. New constraints on the structure, thermochronology, and timing of the Ailao Shan-Red River shear zone, SE Asia. *Journal of Geophysical Research: Solid Earth*, 106(B4):6683–6732. <http://dx.doi.org/10.1029/2000JB900322>
- Li, C.-F., Lin, J., and Kulhanek, D.K., 2013. South China Sea tectonics: opening of the South China Sea and its implications for southeast Asian tectonics, climates, and deep mantle processes since the late Mesozoic. *International Ocean Discovery Program Scientific Prospectus*, 349. <http://dx.doi.org/10.2204/iodp.sp.349.2013>
- Li, C.-F., Shi, X., Zhou, Z., Li, J., Geng, J., and Chen, B., 2010. Depths to the magnetic layer bottom in the South China Sea area and their tectonic implications. *Geophysical Journal International*, 182(3):1229–1247. <http://dx.doi.org/10.1111/j.1365-246X.2010.04702.x>
- Li, C.-F., and Song, T.R., 2012. Magnetic recording of the Cenozoic oceanic crustal accretion and evolution of the South China Sea Basin. *Chinese Science Bulletin*, 57(24):3165–3181. [doi:10.1007/s11434-012-5063-9](https://doi.org/10.1007/s11434-012-5063-9)
- Li, C.-F., Wang, P., Franke, D., Lin, J., and Tian, J., 2012. Unlocking the opening processes of the South China Sea. *Scientific Drilling*, 14:55–59. <http://dx.doi.org/10.2204/iodp.sd.14.07.2012>
- Li, C.-F., Zhou, Z., Hao, H., Chen, H., Wang, J., Chen, B., and Wu, J., 2008a. Late Mesozoic tectonic structure and evolution along the present-day northeastern South China Sea continental margin. *Journal of Asian Earth Sciences*, 31(4–6):546–561. <http://dx.doi.org/10.1016/j.jseaes.2007.09.004>
- Li, C.-F., Zhou, Z., Li, J., Chen, B., and Geng, J., 2008b. Magnetic zoning and seismic structure of the South China Sea ocean basin. *Marine Geophysical Researches*, 29(4):223–238. <http://dx.doi.org/10.1007/s11001-008-9059-4>
- Li, C.-F., Zhou, Z., Li, J., Hao, H., and Geng, J., 2007b. Structures of the northeasternmost South China Sea continental margin and ocean basin: geophysical constraints and tectonic implications. *Marine Geophysical Researches*, 28(1):59–79. <http://dx.doi.org/10.1007/s11001-007-9014-9>

- Li, C.-F., Zhou, Z.Y., Li, J.B., Chen, H.J., Geng, J.H., and Li, H., 2007. Precollisional tectonics and terrain amalgamation offshore southern Taiwan: characterizations from reflection seismic and potential field data. *Science in China, Series D: Earth Sciences*, 50(6):897–908. [doi:10.1007/s11430-007-0025-9](https://doi.org/10.1007/s11430-007-0025-9)
- Li, J.-B., Ding, W.-W., Gao, J.-Y., Wu, Z.-Y., and Zhang, J., 2011. Cenozoic evolution model of the sea-floor spreading in South China Sea: new constraints from high resolution geophysical data. *Chinese Journal of Geophysics*, 54(6):894–906. <http://www.agu.org/wps/ChineseJGeo/54/06/ljb2.pdf>
- Li, Q., Wang, P., Zhao, Q., Shao, L., Zhong, G., Tian, J., Cheng, X., Jian, Z., and Su, X., 2006. A 33 Ma lithostratigraphic record of tectonic and paleoceanographic evolution of the South China Sea. *Marine Geology*, 230(3–4):217–235. <http://dx.doi.org/10.1016/j.mar-geo.2006.05.006>
- Lüdmann, T., and Wong, H.K., 1999. Neotectonic regime on the passive continental margin of the northern South China Sea. *Tectonophysics*, 311(1–4):113–138 [http://dx.doi.org/10.1016/S0040-1951\(99\)00155-9](http://dx.doi.org/10.1016/S0040-1951(99)00155-9)
- Lüdmann, T., Wong, H.K., and Wang, P., 2001. Plio-Quaternary sedimentation processes and neotectonics of the northern continental margin of the South China Sea. *Marine Geology*, 172(3–4):331–358. [http://dx.doi.org/10.1016/S0025-3227\(00\)00129-8](http://dx.doi.org/10.1016/S0025-3227(00)00129-8)
- Macdonald, G.A., 1968. Composition and origin of Hawaiian lavas. In Coats, R.R., Hay, R.L., and Anderson, C.A. (Eds.), *Studies in Volcanology—A Memoir in Honor of Howel Williams*. Memoir - Geological Society of America, 116:477–522.
- Macdonald, G.A., and Katsura, T., 1964. Chemical composition of Hawaiian lavas. *Journal of Petrology*, 5(1):82–133. <http://petrology.oxfordjournals.org/content/5/1/82.abstract>
- Madon, M.B.H., Meng, L.K., and Anuar, A., 1999. Sabah Basin. In Marican, T.S.D.'M.H. (Ed.), *The Petroleum Geology and Resources of Malaysia*. Kuala Lumpur, Malaysia (Petroliam Nasional Berhad), 499–542.
- McIntosh, K.D., Liu, C.-S., and Lee, C.-S., 2012. Introduction to the TAIGER special issue of Marine Geophysical Research. *Marine Geophysical Researches*, 33(4):285–287. <http://dx.doi.org/10.1007/s11001-013-9170-z>
- Morley, C.K., 2002. A tectonic model for the Tertiary evolution of strike-slip faults and rift basins in SE Asia. *Tectonophysics*, 347(4):189–215. [http://dx.doi.org/10.1016/S0040-1951\(02\)00061-6](http://dx.doi.org/10.1016/S0040-1951(02)00061-6)
- Pautot, G., Rangin, C., Briais, A., Tapponnier, P., Beuzart, P., Lericolais, G., Mathieu, X., Wu, J., Han, S., Li, H., Lu, Y., and Zhao, J., 1986. Spreading direction in the central South China Sea. *Nature*, 321(6066):150–154. <http://dx.doi.org/10.1038/321150a0>
- Pubellier, M., Monnier, C., Maury, R., and Tamayo, R., 2004. Plate kinematics, origin and tectonic emplacement of supra-subduction ophiolites in SE Asia. *Tectonophysics*, 392(1–4):9–36. <http://dx.doi.org/10.1016/j.tecto.2004.04.028>
- Rangin, C., Jolivet, L., and Pubellier, M., 1990. A simple model for the tectonic evolution of Southeast Asia and Indonesia regions for the past 43 m.y. *Bulletin de la Société Géologique de France*, 6(6):889–905.
- Rangin, C., Klein, M., Roques, D., Le Pichon, X., and Trong, L.V., 1995. The Red River fault system in the Tonkin Gulf, Vietnam. *Tectonophysics*, 243(3–4):209–222. [http://dx.doi.org/10.1016/0040-1951\(94\)00207-P](http://dx.doi.org/10.1016/0040-1951(94)00207-P)
- Ru, K., and Pigott, J.D., 1986. Episodic rifting and subsidence in the South China Sea. *AAPG Bulletin*, 70(9):1136–1155. <http://aapgbull.geoscienceworld.org/content/70/9/1136.short>

- Schärer, U., Tapponnier, P., Lacassin, R., Leloup, P.H., Dalai, Z., and Ji, S., 1990. Intraplate tectonics in Asia: a precise age for large-scale Miocene movement along the Ailao Shan-Red River shear zone, China. *Earth and Planetary Science Letters*, 97(1–2):65–77. [http://dx.doi.org/10.1016/0012-821X\(90\)90099-J](http://dx.doi.org/10.1016/0012-821X(90)90099-J)
- Schlüter, H.U., Hinz, K., and Block, M., 1996. Tectono-stratigraphic terranes and detachment faulting of the South China Sea and Sulu Sea. *Marine Geology*, 130(1–2):39–78. [http://dx.doi.org/10.1016/0025-3227\(95\)00137-9](http://dx.doi.org/10.1016/0025-3227(95)00137-9)
- Schwartz, J.J., John, B.E., Cheadle, M.J., Miranda, E.A., Grimes, C.B., Wooden, J.L., and Dick, H.J.B., 2005. Dating the growth of oceanic crust at a slow-spreading ridge. *Science*, 310(5748):654–657. <http://dx.doi.org/10.1126/science.1116349>
- Shi, H., and Li, C.-F., 2012. Mesozoic and early Cenozoic tectonic convergence-to-rifting transition prior to opening of the South China Sea. *International Geology Review*, 54(15):1801–1828. <http://dx.doi.org/10.1080/00206814.2012.677136>
- Sibuet, J.-C., Hsu, S.-K., Le Pichon, X., Le Formal, J.-P., Reed, D., Moore, G., and Liu, C.-S., 2002. East Asia plate tectonics since 15 Ma: constraints from the Taiwan region. *Tectonophysics*, 344(1–2):103–134. [http://dx.doi.org/10.1016/S0040-1951\(01\)00202-5](http://dx.doi.org/10.1016/S0040-1951(01)00202-5)
- Smith, W.H.F., and Sandwell, D.T., 1997. Global seafloor topography from satellite altimetry and ship depth soundings. *Science*, 277(5334):1956–1962. <http://dx.doi.org/10.1126/science.277.5334.1956>
- Song, T., and Li, C., 2012. The opening ages and mode of the South China Sea estimated from high-density magnetic tracks. *Progress in Geophysics*, 27(4):1432–1442. <http://dx.doi.org/10.6038/j.issn.1004-2903.2012.04.018>
- Sun, Z., Zhong, Z., Keep, M., Zhou, D., Cai, D., Li, X., Wu, S., and Jiang, J., 2009. 3D analogue modeling of the South China Sea: a discussion on breakup pattern. *Journal of Asian Earth Sciences*, 34(4):544–556. <http://dx.doi.org/10.1016/j.jseaes.2008.09.002>
- Tapponnier, P., Lacassin, R., Leloup, P.H., Shärer, U., Dalai, Z., Haiwei, W., Xiaohan, L., Shaocheng, J., Lianshang, Z., and Jiayou, Z., 1990. The Ailao Shan/Red River metamorphic belt: Tertiary left-lateral shear between Indochina and South China. *Nature*, 343(6257):431–437. <http://dx.doi.org/10.1038/343431a0>
- Tapponnier, P., Peltzer, G., and Armijo, R., 1986. On the mechanics of the collision between India and Asia. In Ramsey, J.G., Coward, M.P., and Ries, A. (Eds.), *Collision Tectonics*. Geological Society Special Publication, 19:115–157. <http://dx.doi.org/10.1144/GSL.SP.1986.019.01.07>
- Tapponnier, P., Peltzer, G., Le Dain, A.Y., Armijo, R., and Cobbold, P., 1982. Propagating extrusion tectonics in Asia: new insights from simple experiments with plasticine. *Geology*, 10(12):611–616. [http://dx.doi.org/10.1130/0091-7613\(1982\)10<611:PETIAN>2.0.CO;2](http://dx.doi.org/10.1130/0091-7613(1982)10<611:PETIAN>2.0.CO;2)
- Taylor, B., and Hayes, D.E., 1980. The tectonic evolution of the South China Basin. In Hayes, D.E. (Ed.), *The Tectonic and Geologic Evolution of Southeast Asian Seas and Islands*. Geophysical Monograph, 23:89–104. <http://dx.doi.org/10.1029/GM023p0089>
- Taylor, B., and Hayes, D.E., 1983. Origin and history of the South China Sea Basin. In Hayes, D.E. (Ed.), *The Tectonic and Geologic Evolution of Southeast Asian Seas and Islands* (Pt. 2). Geophysical Monograph, 27:23–56. <http://dx.doi.org/10.1029/GM027p0023>
- Tejada, M.L.G., Mahoney, J.J., Castillo, P.R., Ingle, S.P., Sheth, H.C., and Weis, D., 2004. Pinpricking the elephant: evidence on the origin of the Ontong Java Plateau from Pb-Sr-Hf-Nd isotopic characteristics of ODP Leg 192 basalts. In Fitton, J.G., Mahoney, J.J., Wallace, P.J., and Saunders, A.D. (Eds.), *Origin and Evolution of the Ontong Java Plateau*. Geological Society Special Publication, 229(1):133–150. <http://dx.doi.org/10.1144/GSL.SP.2004.229.01.09>

- Tominaga, M., Teagle, D.A.H., Alt, J.C., and Umino, S., 2009. Determination of the volcanostratigraphy of the oceanic crust formed at superfast spreading ridge: electrofacies analyses of ODP/IOPD Hole 1256D. *Geochemistry, Geophysics, Geosystems*, 10(1):Q01003. <http://dx.doi.org/10.1029/2008GC002143>
- Tongkul, F., 1994. The geology of northern Sabah, Malaysia: its relationship to the opening of the South China Sea basin. *Tectonophysics*, 235(1–2):131–147. [http://dx.doi.org/10.1016/0040-1951\(94\)90021-3](http://dx.doi.org/10.1016/0040-1951(94)90021-3)
- Tu, K., Flower, M.F.J., Carlson, R.W., Xie, G., Chen, C.-Y., and Zhang, M., 1992. Magmatism in the South China Basin: 1. Isotopic and trace-element evidence for an endogenous Dupal mantle component. *Chemical Geology*, 97(1–2):47–63. [http://dx.doi.org/10.1016/0009-2541\(92\)90135-R](http://dx.doi.org/10.1016/0009-2541(92)90135-R)
- Wang, P., 2012. Tracing the life history of a marginal sea—on “The South China Sea Deep” research program. *Chinese Science Bulletin*, 57(24):3093–3114. <http://dx.doi.org/10.1007/s11434-012-5087-1>
- Wang, P., and Li, Q. (Eds.), 2009. *Developments in Paleoenvironmental Research (Vol. 13): The South China Sea: Paleooceanography and Sedimentology*: Dordrecht (Springer). 13. <http://dx.doi.org/10.1007/978-1-4020-9745-4>
- Wang, P., Prell, W.L., Blum, P., et al., 2000. *Proceedings of the Ocean Drilling Program, Initial Reports*, 184: College Station, TX (Ocean Drilling Program). <http://dx.doi.org/10.2973/odp.proc.ir.184.2000>
- Wang, X.-C., Li, Z.-X., Li, X.-H., Li, J., Liu, Y., Long, W.-G., Zhou, J.-B., and Wang, F., 2012. Temperature, pressure, and composition of the mantle source region of late Cenozoic basalts in Hainan Island, SE Asia: a consequence of a young thermal mantle plume close to subduction zones? *Journal of Petrology*, 53(1):177–233. <http://dx.doi.org/10.1093/petrology/egr061>
- Xiao, G., and Zheng, J., 2004. New opinions about “residual Tethys” in northern South China Sea slope and southern East China Sea. *Geoscience*, 18(1):103–108. (in Chinese)
- Xu, Y., Wei, J., Qiu, H., Zhang, H., and Huang, X., 2012. Opening and evolution of the South China Sea constrained by studies on volcanic rocks: preliminary results and a research design. *Chinese Science Bulletin*, 57(24):3150–3164. <http://dx.doi.org/10.1007/s11434-011-4921-1>
- Yan, P., Zhou, D., and Liu, Z., 2001. A crustal structure profile across the northern continental margin of the South China Sea. *Tectonophysics*, 338(1):1–21. [doi:10.1016/S0040-1951\(01\)00062-2](https://doi.org/10.1016/S0040-1951(01)00062-2)
- Yang, J.Y., and Feng, X.S., 2003. An analysis of middle–late Mesozoic tectonics, paleogeography, and petroleum potential in the northeastern South China Sea. *China Offshore Oil and Gas (Geology)*, 17:89–103. [http://en.cnki.com.cn/Article\\_en/CJFDTOTAL-ZHSD200302002.htm](http://en.cnki.com.cn/Article_en/CJFDTOTAL-ZHSD200302002.htm)
- Yao, B., 1995. Characteristics and tectonic significance of the Zhongnan-Lile fault. *Geological Research of South China Sea, Memoir*, 7:1–14. (in Chinese)
- Yao, B., Zeng, W., Hayes, D.E., and Spangler, S., 1994. *The Geological Memoir of South China Sea Surveyed Jointly by China and USA*: Wuhan (China Univ. Geosci. Press). (in Chinese)
- Zhang, G.-L., Chen, L.-H., and Li, S.-Z., 2013. Mantle dynamics and generation of a geochemical mantle boundary along the East Pacific Rise—Pacific/Antarctic Ridge. *Earth and Planetary Science Letters*, 383:153–163. [doi:10.1016/j.epsl.2013.09.045](https://doi.org/10.1016/j.epsl.2013.09.045)
- Zhang, G., Smith-Duque, C., Tang, S., Li, H., Zirikian, C., D’Hondt, S., Inagaki, F., and IODP Expedition 329 Scientists, 2012a. Geochemistry of basalts from IODP Site U1365: impli-

- cations for magmatism and mantle source signatures of the mid-Cretaceous Osbourn Trough. *Lithos*, 144–145:73–87. doi:10.1016/j.lithos.2012.04.014
- Zhang, G., Zeng, Z., Yin, X., Wang, X., and Chen, D., 2009. Deep fractionation of clinopyroxene in the East Pacific Rise 13°N: evidence from high MgO MORB and melt inclusions. *Acta Geologica Sinica*, 83(2):266–277. <http://dx.doi.org/10.1111/j.1755-6724.2009.00030.x>
- Zhang, G.-L., Zong, C.-L., Yin, X.-B., and Li, H., 2012b. Geochemical constraints on a mixed pyroxenite–peridotite source for East Pacific Rise basalts. *Chemical Geology*, 330–331:176–187. <http://dx.doi.org/10.1016/j.chemgeo.2012.08.033>
- Zhang, L., Zhao, M.H., Wang, J., He, E.Y., Ao, W., Qiu, X.L., Xu, H.L., Wei, X.D., and Zhang, J.Z., 2013. The correction of OBS position and recent advances of 3D seismic exploration in the central sub-basin of South China Sea. *Earth Science—Journal of China University of Earth Geosciences*, 2013(1):33–42. (in Chinese)
- Zhou, D., Ru, K., and Chen, H., 1995. Kinematics of Cenozoic extension on the South China Sea continental margin and its implications for the tectonic evolution of the region. *Tectonophysics*, 251(1–4):161–177. [http://dx.doi.org/10.1016/0040-1951\(95\)00018-6](http://dx.doi.org/10.1016/0040-1951(95)00018-6)
- Zhou, D., Sun, Z., Chen, H., Xu, H., Wang, W., Pang, X., Cai, D., and Hu, D., 2008. Mesozoic paleogeography and tectonic evolution of South China Sea and adjacent areas in the context of Tethyan and Paleo-Pacific interconnections. *Island Arc*, 17(2):186–207. <http://dx.doi.org/10.1111/j.1440-1738.2008.00611.x>
- Zhou, X.M., and Li, W.X., 2000. Origin of late Mesozoic igneous rocks in southeastern China: implications for lithosphere subduction and underplating of mafic magmas. *Tectonophysics*, 326(3–4):269–287. [http://dx.doi.org/10.1016/S0040-1951\(00\)00120-7](http://dx.doi.org/10.1016/S0040-1951(00)00120-7)

Expedition 349 Preliminary Report

**Table T1. Coring summary, Expedition 349.**

Hole	Latitude	Longitude	Water depth (m)	Penetration DSF (m)	Cored interval (m)	Recovered length (m)	Recovery (%)	Drilled interval (m)	Drilled interval (N)	Total cores (N)	APC cores (N)	XCB cores (N)
U1431A	15°22.5491'N	117°00.0009'E	4237.3	28.4	28.4	28.39	100	—	0	3	3	0
U1431B	15°22.5480'N	117°00.0125'E	4236.7	17.0	17.0	17.16	101	—	0	2	2	0
U1431C	15°22.5371'N	117°00.0108'E	4239.5	14.2	14.2	14.45	102	—	0	2	2	0
U1431D	15°22.5379'N	117°00.0022'E	4240.5	617.0	617.0	402.11	65	—	0	67	19	48
U1431E	15°22.5380'N	116°59.9903'E	4240.3	1008.8	443.5	242.35	55	565.3	2	47	0	0
U1432A	18°21.1051'N	116°23.4504'E	3829.0	62.0	—	—	0	62	1	0	0	0
U1432B	18°21.1062'N	116°23.4512'E	3829.0	800.0	—	—	0	800	4	0	0	0
U1432C	18°21.0831'N	116°23.4504'E	3829.0	110.0	110.0	88.74	81	—	0	12	12	0
U1433A	12°55.1380'N	115°02.8345'E	4379.4	188.3	188.3	168.79	90	—	0	20	20	0
U1433B	12°55.1313'N	115°02.8484'E	4379.3	858.5	672.4	443.04	66	186.1	1	74	0	0
U1434A	13°11.5080'N	114°55.4005'E	4009.0	312.5	115.5	26.43	23	197	1	14	0	0
U1435A	18°33.3466'N	116°36.6174'E	3252.5	300.0	300.0	171.37	57	—	0	32	0	0
			Total:		2506.3	1602.83		1810.4	9	273	58	48

APC = advanced piston corer, XCB = extended core barrel, RCB = rotary core barrel. — = no data.

Hole	Latitude	Longitude	RCB cores (N)	Other cores (N)	Date started (UTC)	Date finished (UTC)	Time on hole (days)	Comments
U1431A	15°22.5491'N	117°00.0009'E	0	0	1/30/2014 22:40	1/31/2014 19:45	0.88	
U1431B	15°22.5480'N	117°00.0125'E	0	0	1/31/2014 19:45	1/31/2014 22:20	0.11	
U1431C	15°22.5371'N	117°00.0108'E	0	0	1/31/2014 22:20	2/1/2014 00:52	0.11	Split liner on mud line core
U1431D	15°22.5379'N	117°00.0022'E	0	0	2/1/2014 00:52	2/6/2014 06:15	5.22	
U1431E	15°22.5380'N	116°59.9903'E	47	1	2/6/2014 06:15	2/15/2014 22:00	9.66	
U1432A	18°21.1051'N	116°23.4504'E	0	0	2/16/2014 15:30	2/17/2014 18:05	1.11	Jet-in test
U1432B	18°21.1062'N	116°23.4512'E	0	0	2/17/2014 18:05	3/6/2014 12:36	16.77	Jet-in 20 inch casing
U1432C	18°21.0831'N	116°23.4504'E	0	0	2/21/2014 08:20	2/22/2014 23:35	1.64	APC/XCB coring
U1433A	12°55.1380'N	115°2.8345'E	0	0	3/7/2014 18:30	3/10/2014 07:25	2.54	
U1433B	12°55.1313'N	115°2.8484'E	74	0	3/10/2014 19:25	3/19/2014 15:00	8.82	
U1434A	13°11.5080'N	114°55.4005'E	14	0	3/19/2014 16:48	3/22/2014 15:48	2.96	
U1435A	18°33.3466'N	116°36.6174'E	32	0	3/24/2014 07:24	3/27/2014 11:00	3.15	
Total:			167	1				

**Figure F1.** Regional topography and geodynamic framework of Southeast Asia. Data based on Smith and Sandwell (1997). Solid red lines = regional faults. Red arrows show direction of plate movement and solid red circles mark sites drilled during Expedition 349.

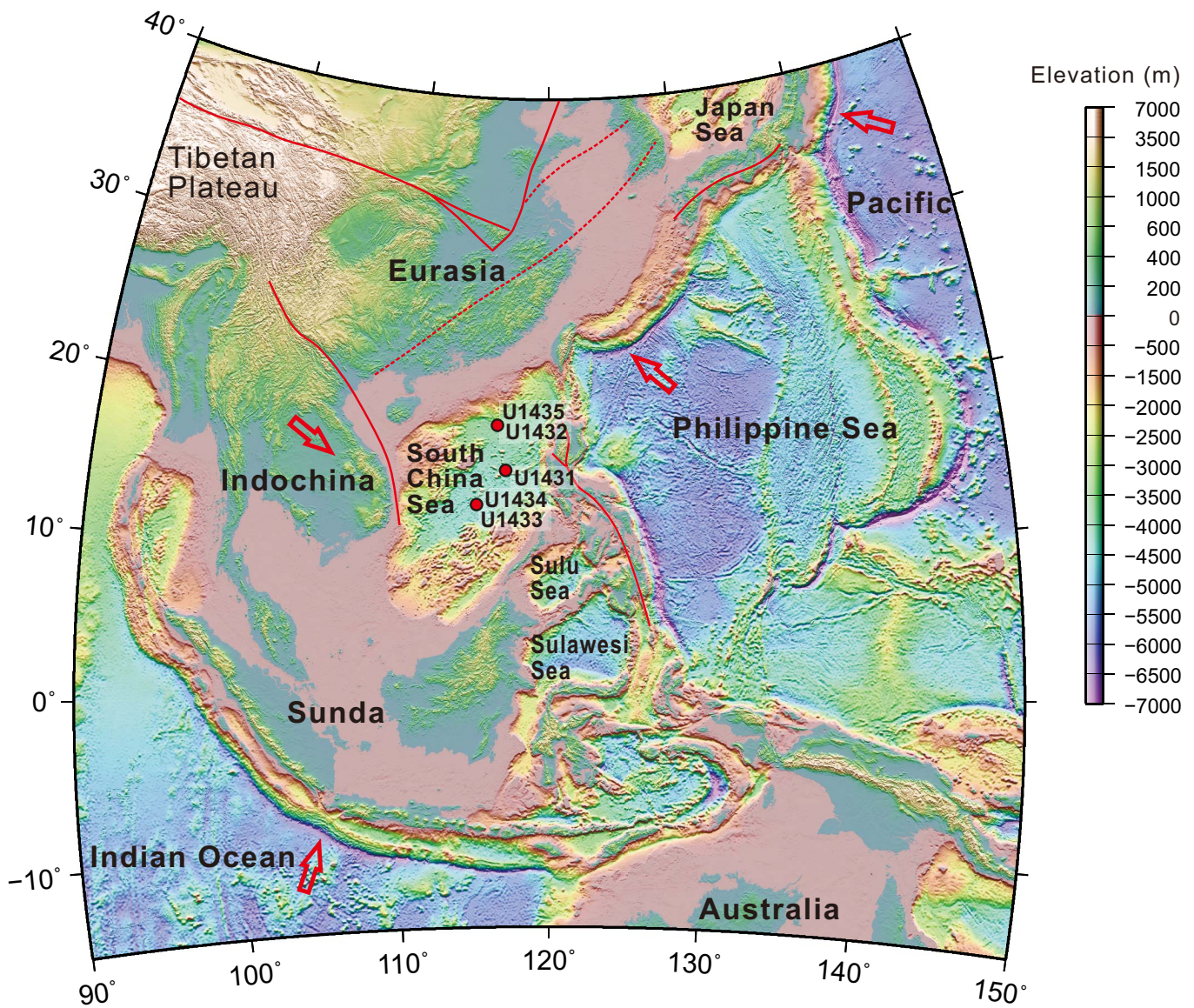


**Figure F2.** Topographic and bathymetric map of the South China Sea and surrounding region. Dashed red line = inferred Zhongnan fault. Solid red circles = sites drilled during Expedition 349. Solid white circle = location of Ocean Drilling Program (ODP) Site 1148. Pink lines = seismic surveys collected during Cruises SO49 (1987) and SO197 (2008) on the R/V *Sonne*. Blue, red, and black lines = seismic data collected by Chinese research institutes and oil companies. Turquoise lines = reflection seismic data acquired in the 1980s from Cruises V3607, V3608, V3613, V3614, and RC2006.

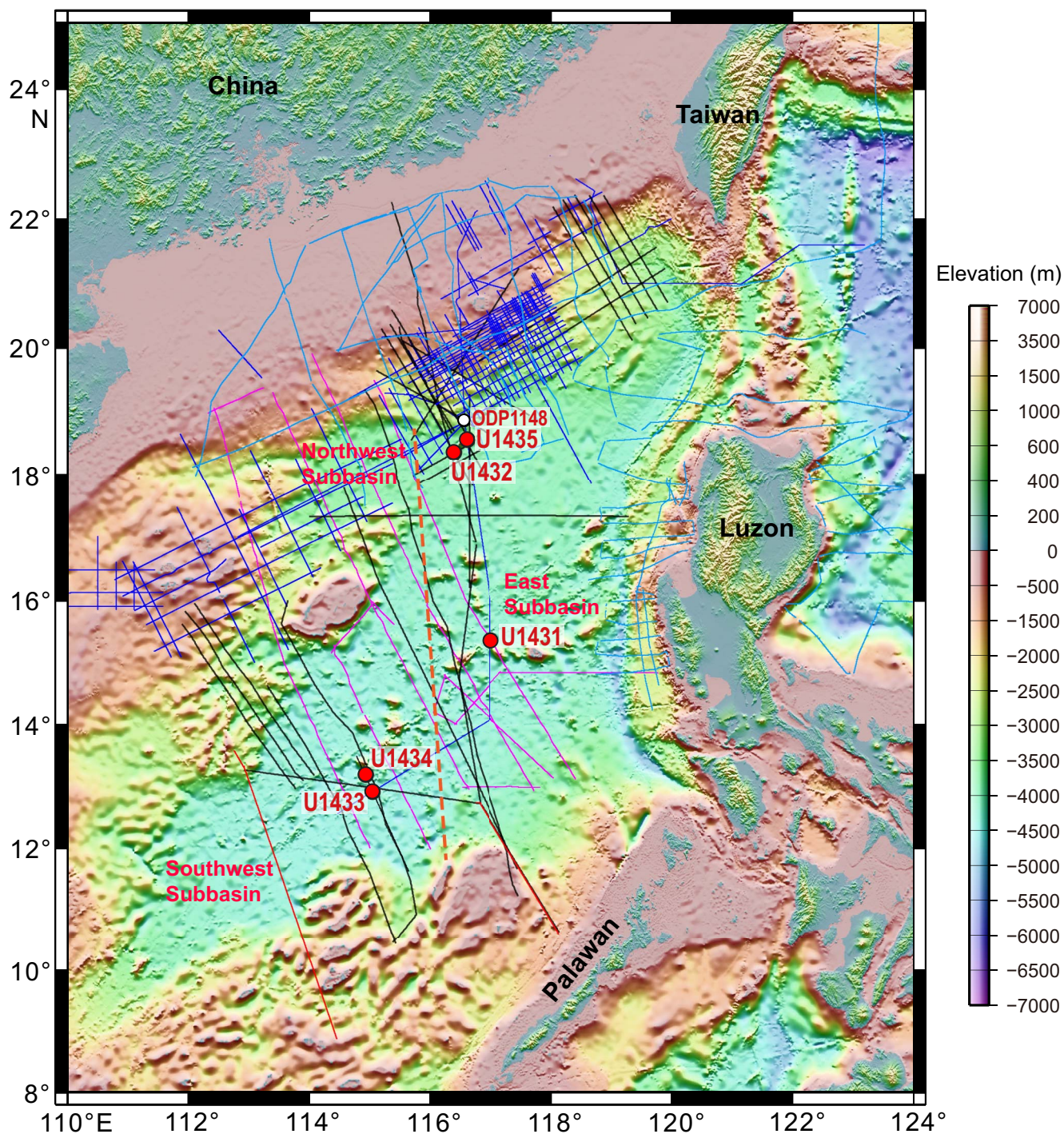


**Figure F3.** Different hypothetical models for the driving mechanisms of the opening of the South China Sea. **A.** Opening induced by India-Eurasia continental collision and consequent tectonic extrusion (Tapponnier et al., 1982, 1990; Briais et al., 1993; Leloup et al., 2001; Flower et al., 2001). **B.** Opening induced by slab pull and subduction of the proto-South China Sea (Taylor and Hayes, 1980, 1983; Holloway, 1982; Hall, 2002). **C.** Opening induced by an upwelling mantle plume (e.g., Fan and Menzies, 1992; Xu et al., 2012). **D.** Opening induced by regional extension related to subduction and retreat of the Pacific plate (Taylor and Hayes, 1980, 1983; Shi and Li, 2012).

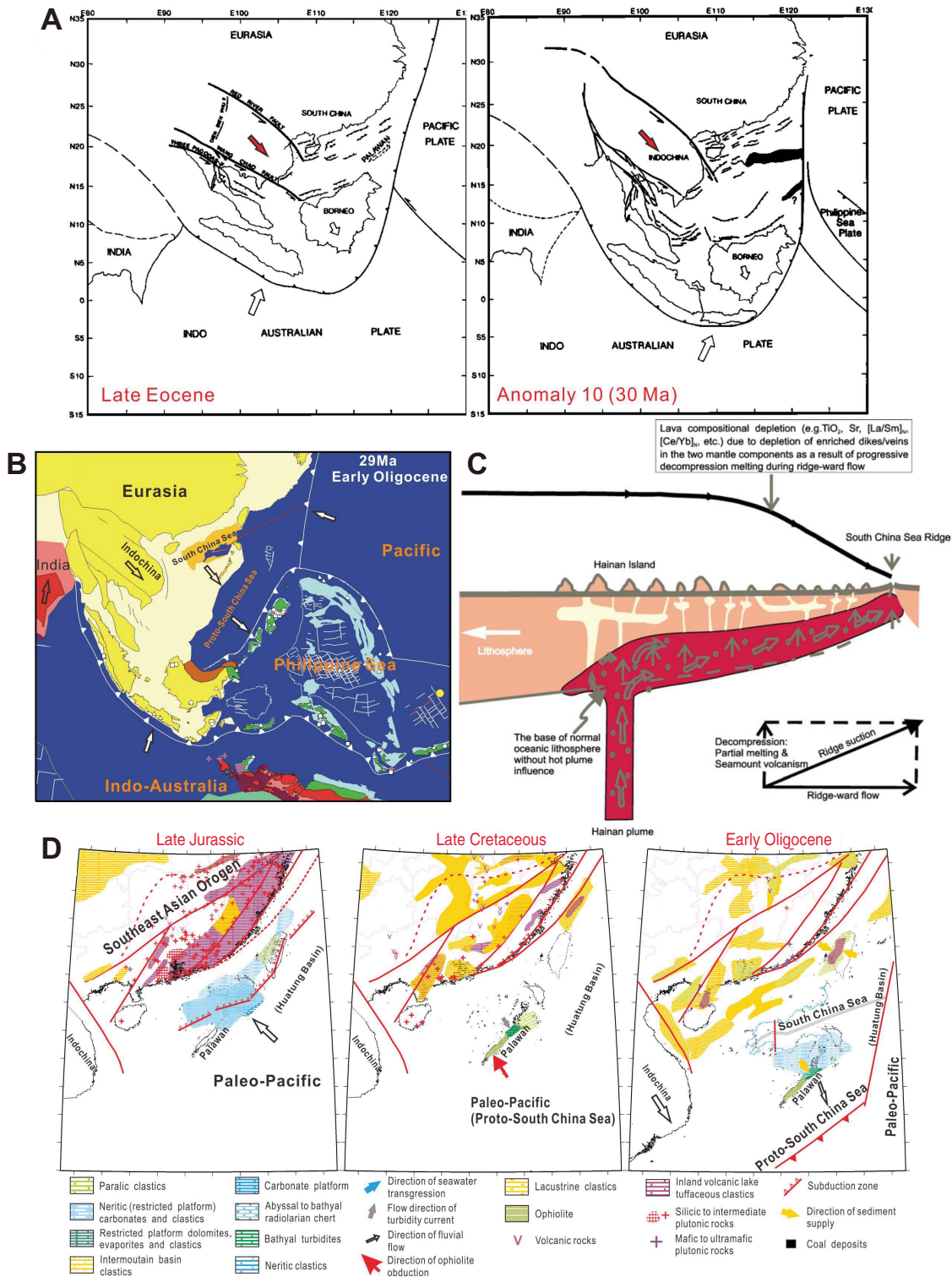


**Figure F4.** Total field magnetic map (based on [globalchange.nasa.gov/r/d/\[GCMD\]GSJ\\_EASTASIA\\_CDROM](http://globalchange.nasa.gov/r/d/[GCMD]GSJ_EASTASIA_CDROM)) showing major magnetic zones (A, B, C1, C1', C2, D, and E). M1 and M2 are two major magnetic anomalies in the East Subbasin. ZNF = Zhongnan fault, L RTPB = Luzon-Ryukyu transform plate boundary, DS = Dongsha Rise; SCMA = offshore south China magnetic anomaly, XS = Xisha, ZB = Macclesfield Bank, LB = Reed Bank, NM = Dangerous Grounds. Red lines = transform faults, solid yellow circles = sites drilled during Expedition 349, solid pink circle = location of Ocean Drilling Program (ODP) Site 1148. After Li et al. (2008b).

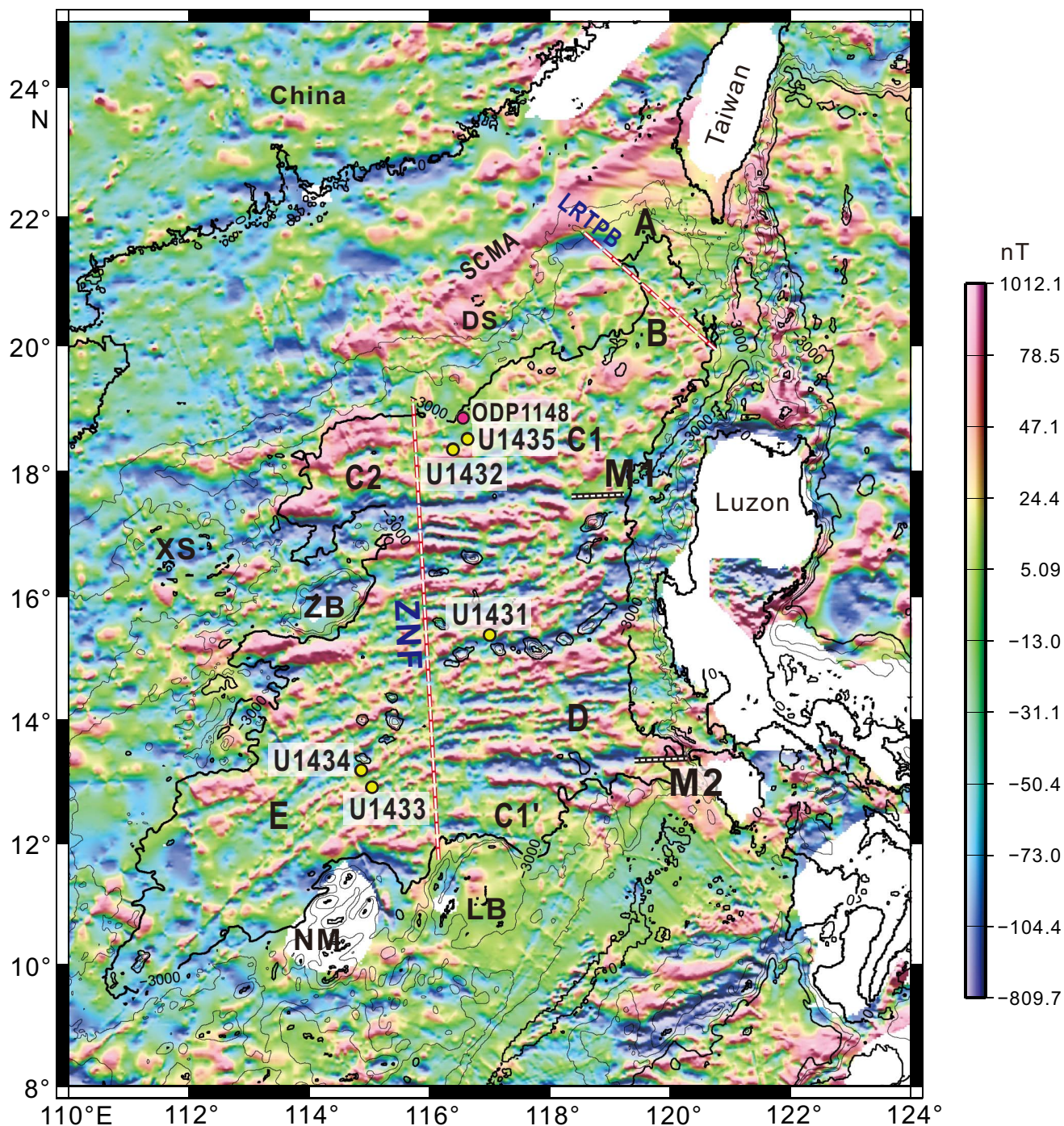


**Figure F5.** Examples of two groups of contrasting tectonic models for the opening phases of the South China Sea. **A.** Multiphase episodic rifting model in which the Southwest Subbasin is the first to open from continental rifting (after Ru and Pigott, 1986). N.P. = Northwest Palawan, S.P. = South Palawan, M.B. = Macclesfield Bank, R.B. = Reed Bank, P.I. = Paracel Islands, F1, F2, and F3 = faults. (Continued on next page.)

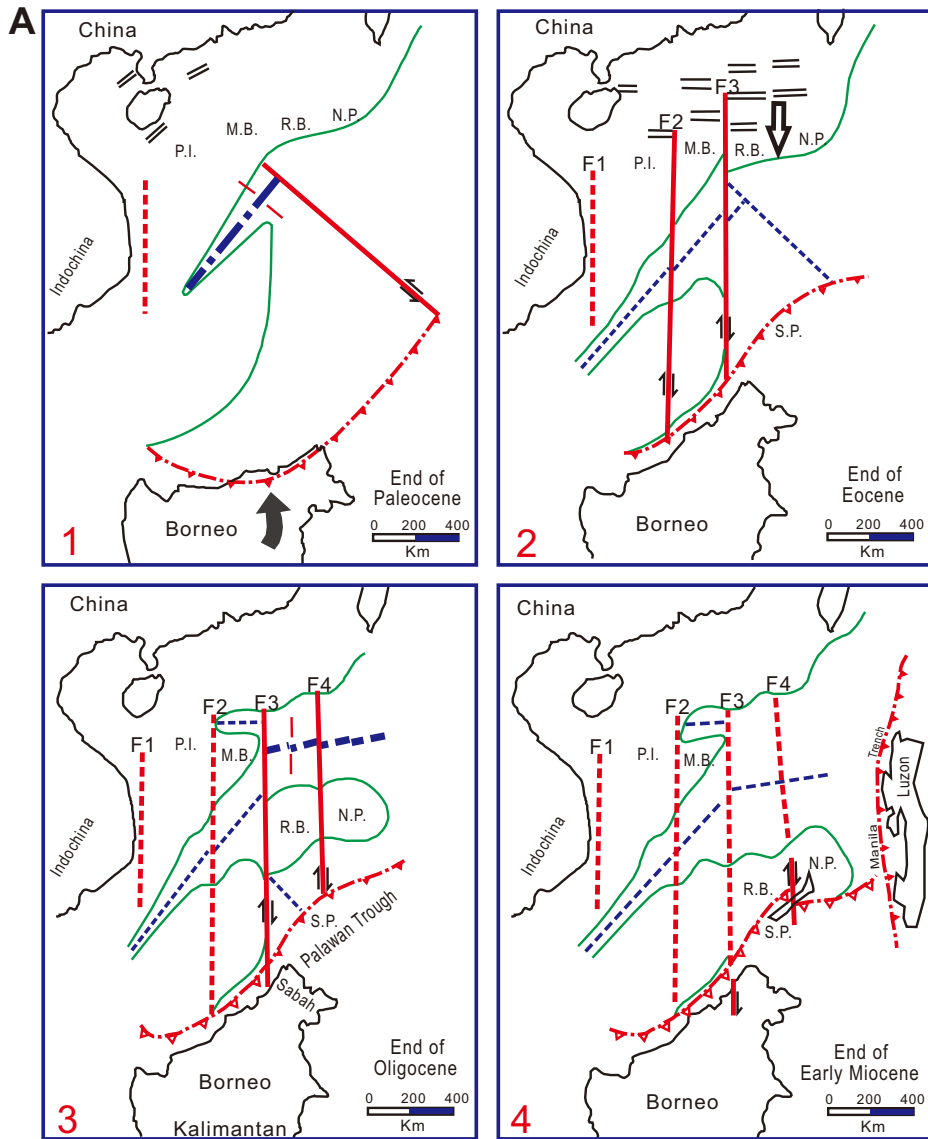
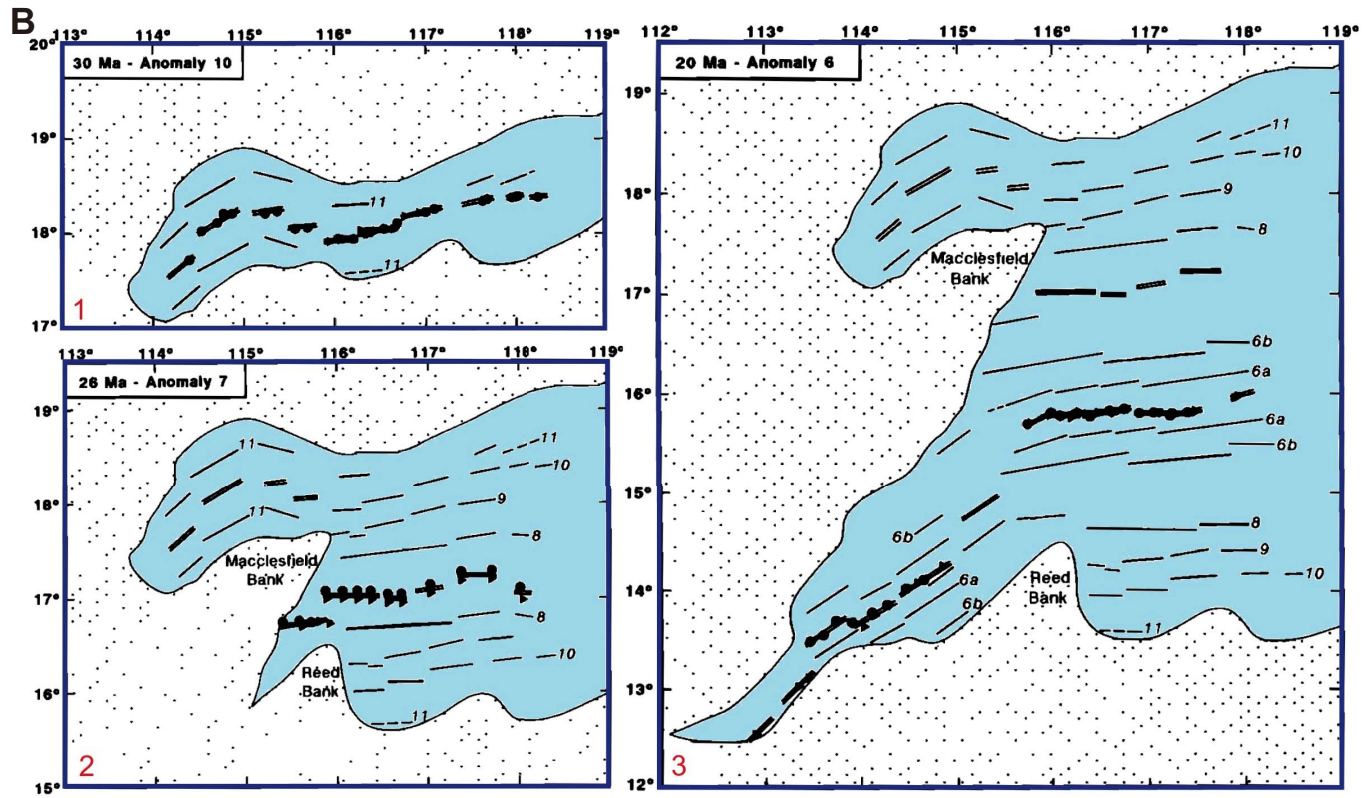
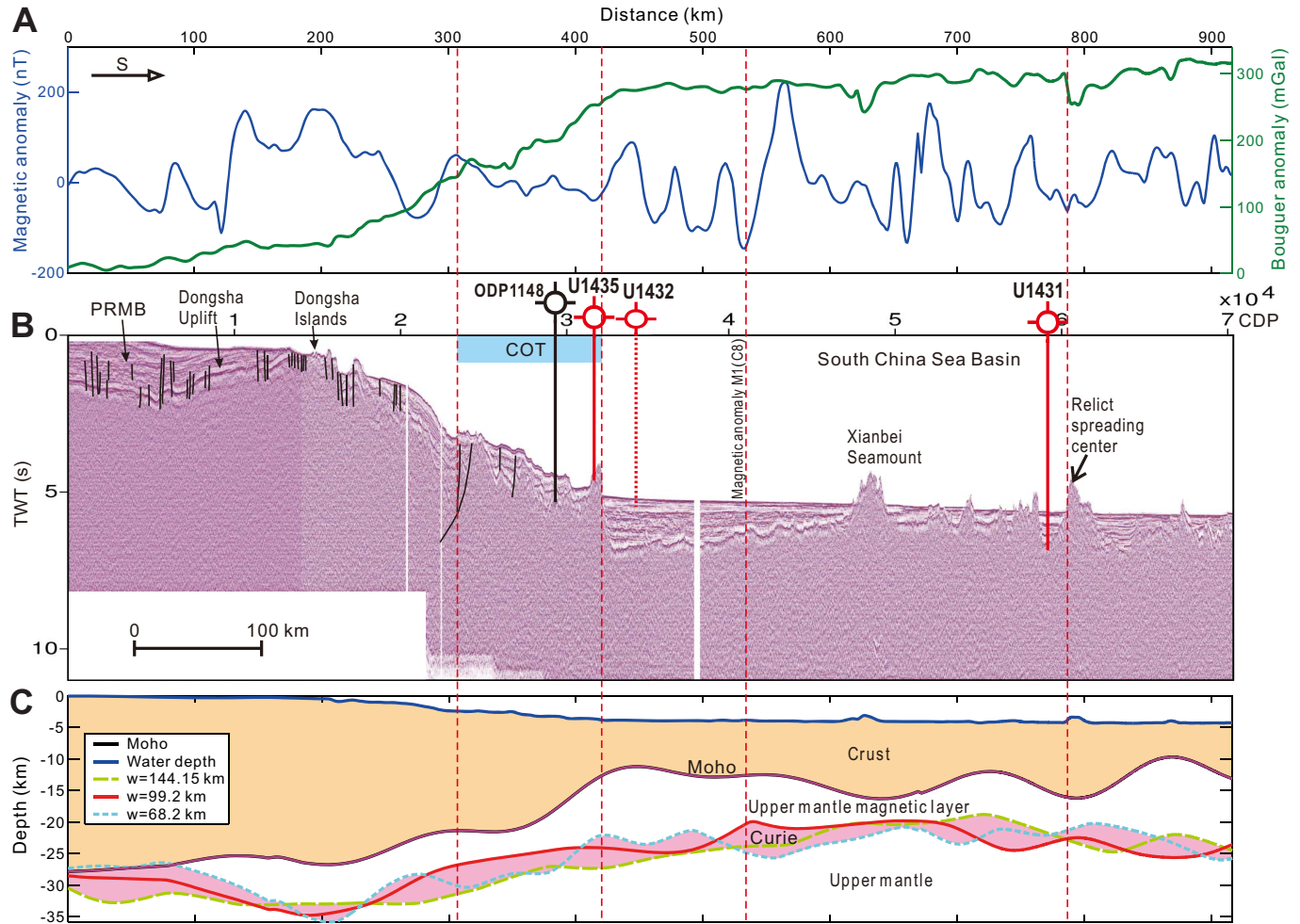


Figure F5 (continued). B. Southwestward continuous propagating model in which the Southwest Subbasin is coeval with the central East Subbasin (after Briais et al., 1993).



**Figure F6.** Proposed sampling transect in the East Subbasin (after Li et al., 2010). **A.** Total field magnetic anomaly and Bouguer anomaly along the seismic line shown in **B**. **B.** Sites U1431, U1432, and U1435 in the East Subbasin and Ocean Drilling Program (ODP) Site 1148 shown on a composite seismic line. Solid lines = sites that fall on the seismic profile, dashed lines = site locations projected onto the line. TWT = two-way traveltime, COT = continent-ocean transition zone, PRMB = Pearl River Mouth Basin, CDP = common depth point. **C.** Depths to the Moho and Curie point estimated from gravity and magnetic anomalies, respectively.  $w$  = width of moving windows.



**Figure F7.** Seismic profile Line NDS3 showing the short sampling transect in the Southwest Subbasin and location of Sites U1433 and U1434. CDP = common depth point.

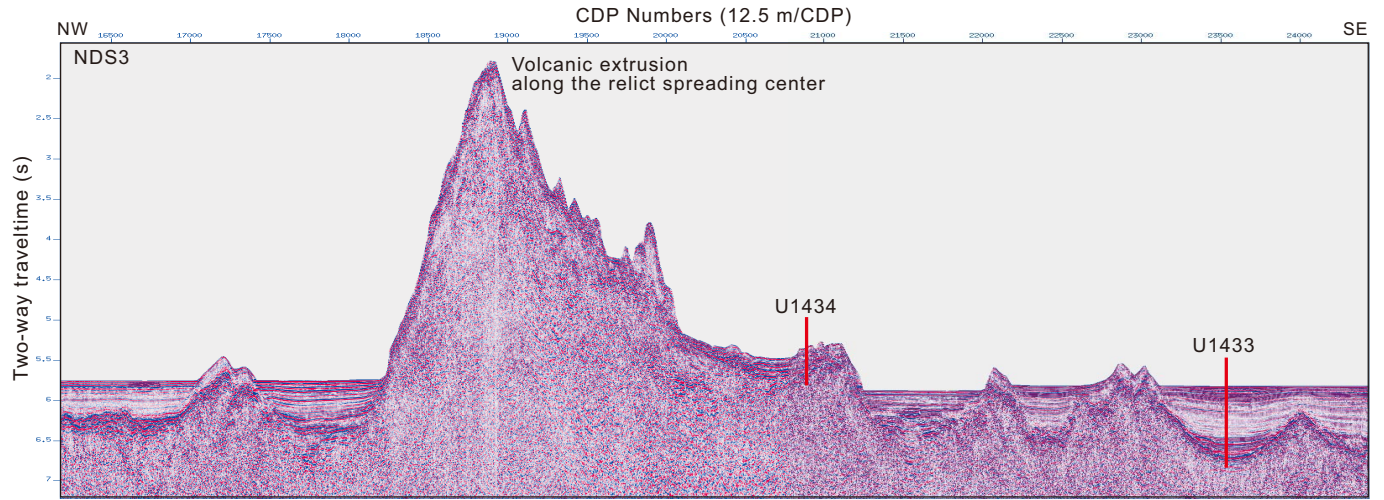


**Figure F8. A.** Bathymetric map of the South China Sea and surrounding region. Yellow circles denote sites drilled during International Ocean Discovery Program (IODP) Expedition 349. Solid pink circles are sites drilled during Ocean Drilling Program (ODP) Leg 184. Yellow dashed line = inferred continent/ocean boundary, blue lines = fossil South China Sea spreading center, white line with triangles = Manila Trench. **B.** Detailed bathymetry around Site U1431 (green box in A) showing nearby bathymetric highs and the Manila Trench. (Continued on next page.)

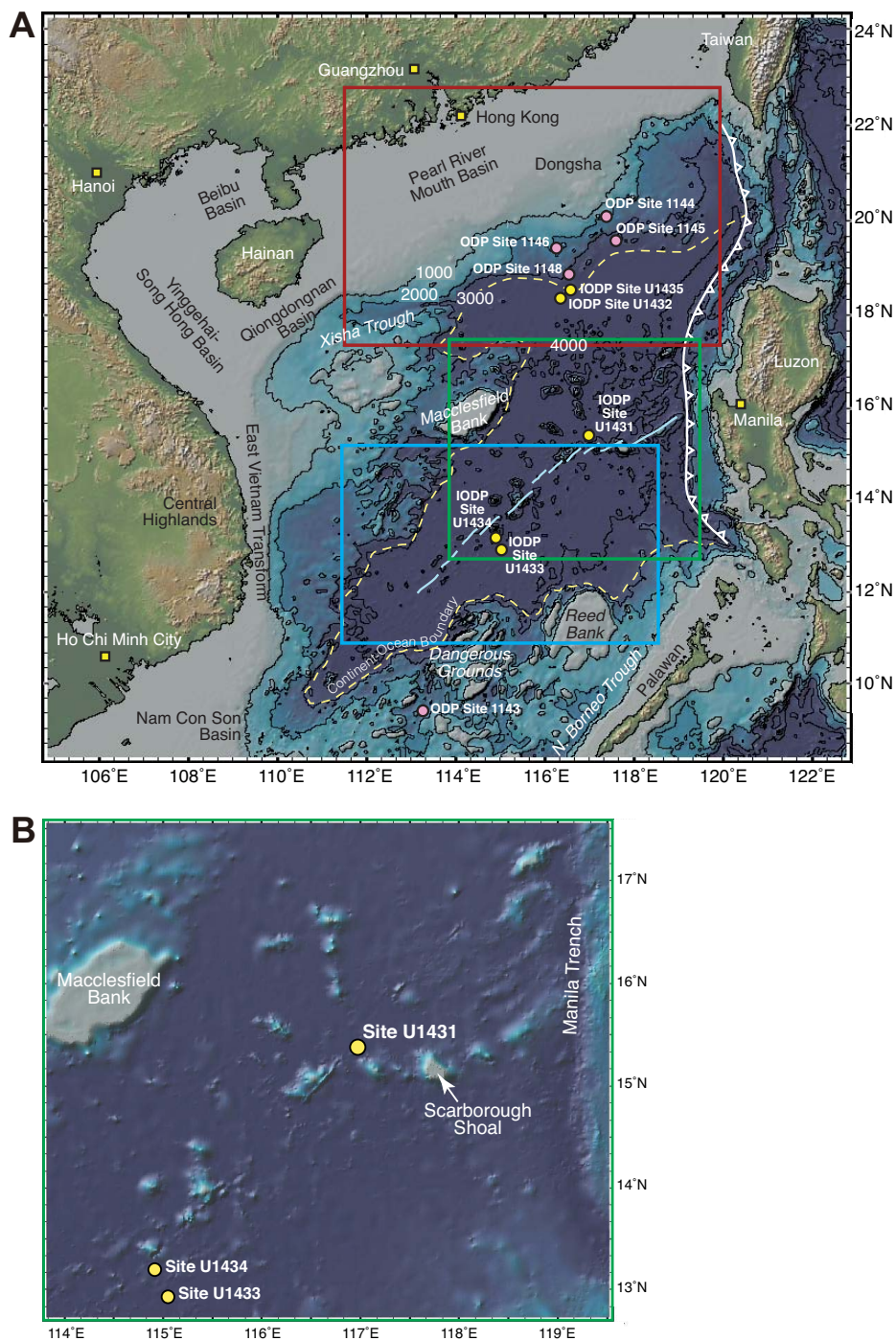


**Figure F8 (continued).** C. Detailed bathymetry around Sites U1432 and U1435 (red box in A) showing nearby continental shelf, the Manila Trench, and inferred continent/ocean boundary. D. Detailed bathymetry around Sites U1433 and U1434 (blue box in A) showing nearby seamount and Dangerous Grounds and Reed Bank to the south.

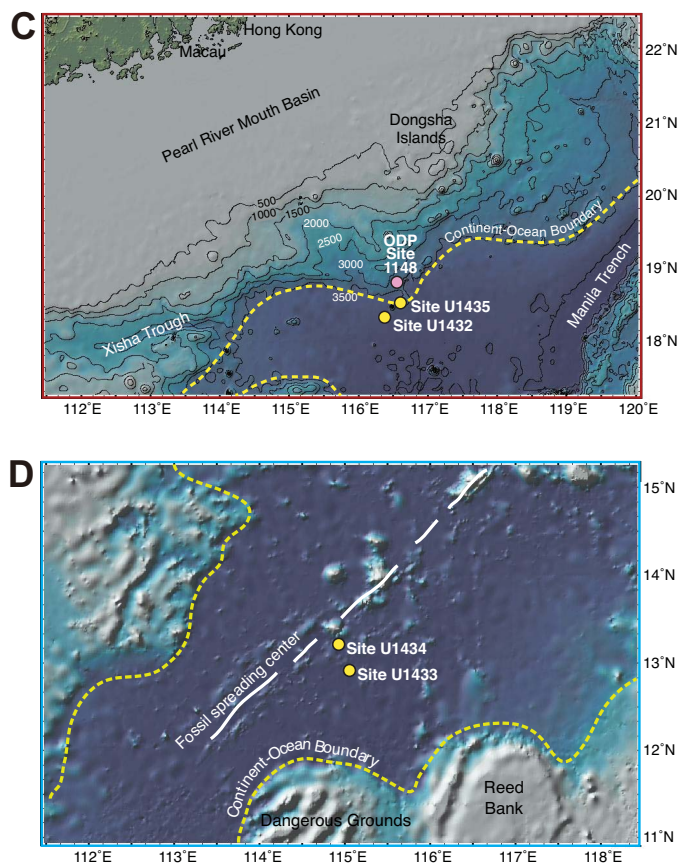


**Figure F9.** Lithostratigraphic and physical properties summary of Site U1431 based on a composite of Holes U1431D and U1431E. Core magnetic susceptibility and gamma-ray attenuation (GRA) density (filtered) were measured on the Section-Half Multisensor Logger, moisture and density (MAD) were measured on discrete samples, and *P*-wave velocities were measured on the Section Half Measurement Gantry. Downhole log data, magnetic susceptibility, and total natural gamma radiation are from the main pass of the triple combination tool string, and *P*-wave velocities are from Pass 2 of the Formation MicroScanner-sonic tool string. Downhole log depths have been shifted upwards by 5 m to correlate with the core physical property data.

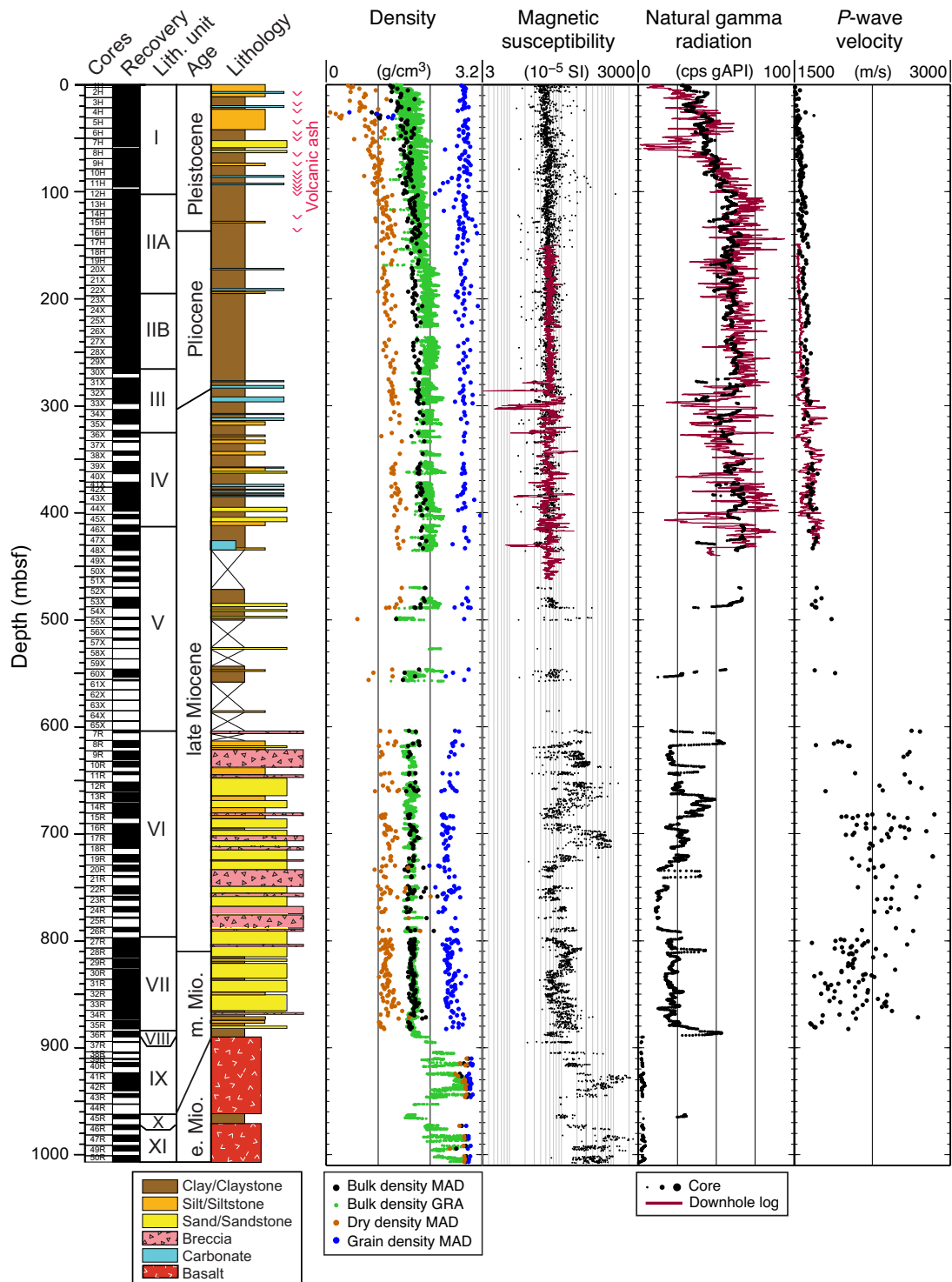


**Figure F10.** Age-depth model with estimated sedimentation rates for Site U1431 based on biostratigraphic and paleomagnetic datums. Dashed lines indicate an alternate or tentative interpretation.

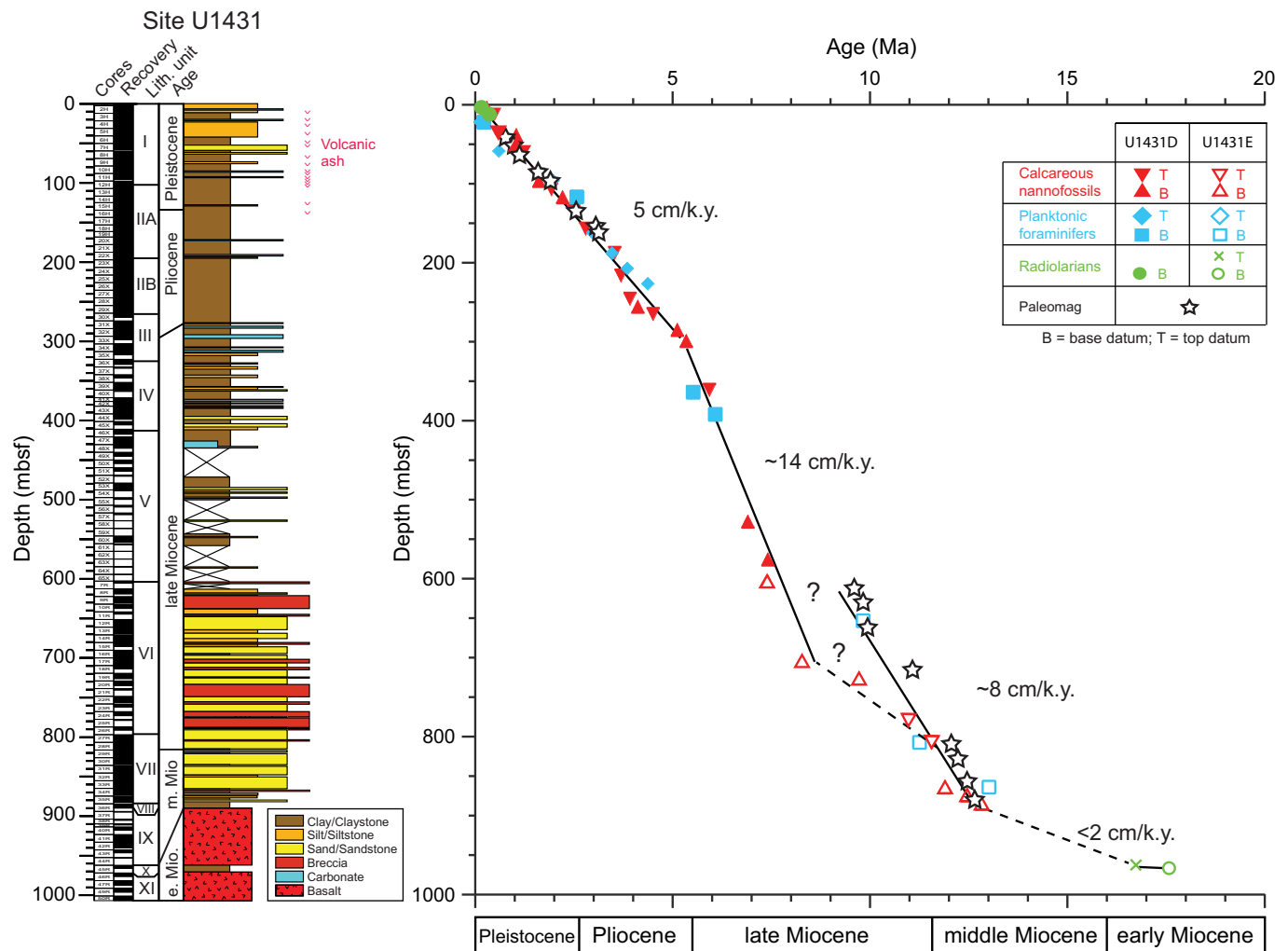


**Figure F11.** Lithostratigraphic summary of igneous rock and lithologic features, Hole U1431E. EOH = end of hole.

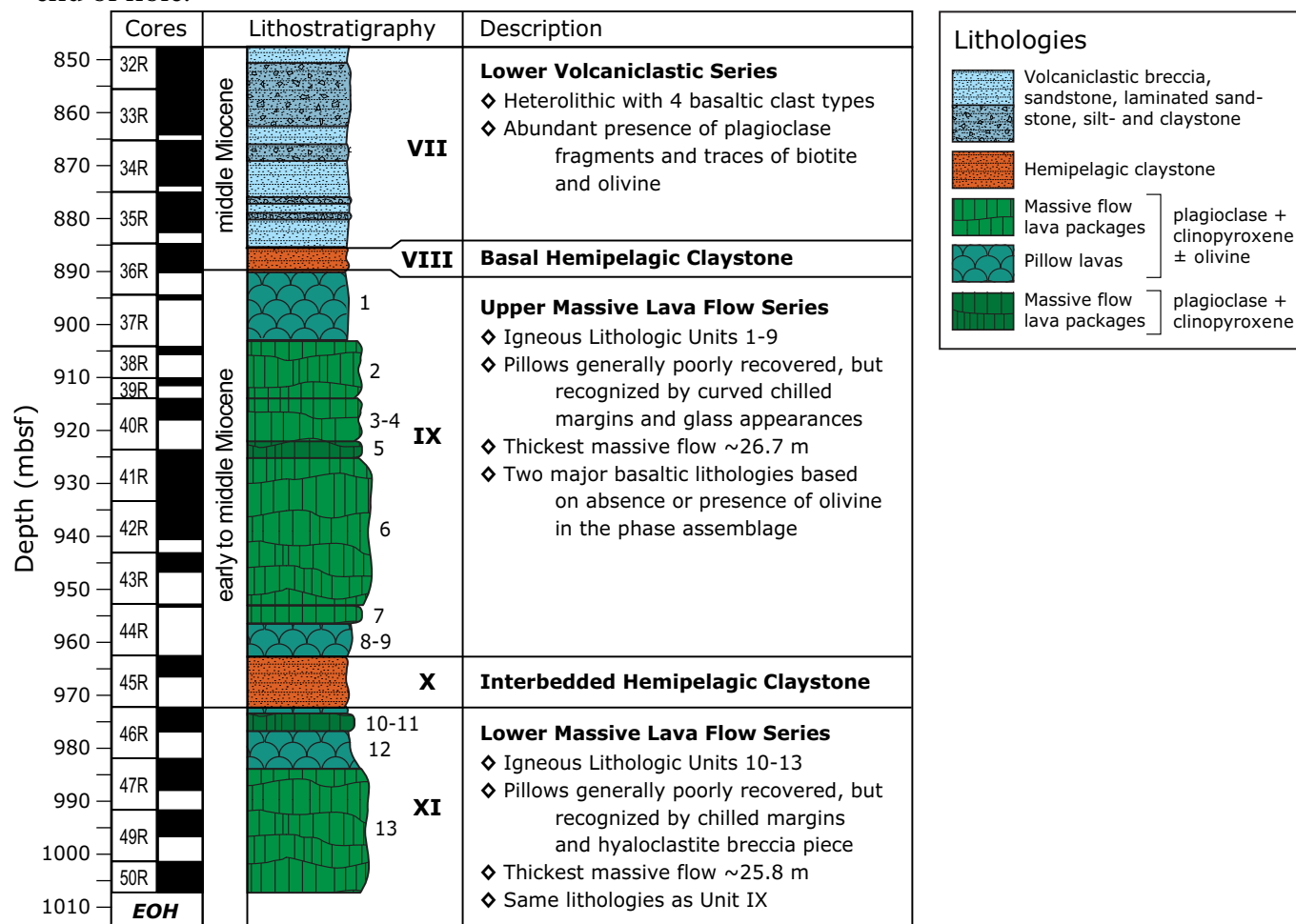


**Figure F12.** Total alkalis vs. silica, with classification of volcanic rock types of Le Maitre et al. (1989). The dashed blue line divides data between tholeiitic and alkalic lavas of Hawaii (Macdonald and Katsura, 1964; Macdonald, 1968). Shown for comparison are data for Indian Ocean mid-ocean-ridge basalt (MORB) from the Geochemical Rock Database ([georoc.mpch-mainz.gwdg.de/](http://georoc.mpch-mainz.gwdg.de/)), the seamount in the South China Sea (Tu et al., 1992; Hékinian et al., 1989), ocean island basalt of Hainan Island (Wang et al., 2012), and Pacific MORB (Zhang et al., 2009, 2012a, 2012b, 2013).

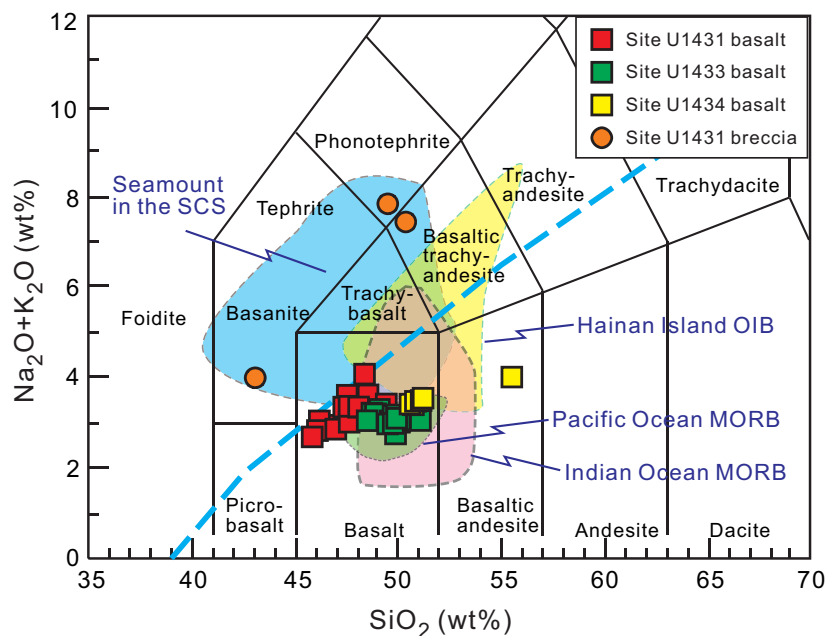


**Figure F13.** Plots of  $\text{TiO}_2$  vs. (A)  $\text{P}_2\text{O}_5$ , (B) V, (C) Sc, and (D) Sr. Shown for comparison are data for Indian Ocean mid-ocean-ridge basalt (MORB) from the Geochemical Rock Database ([georoc.mpch-mainz.gwdg.de/](http://georoc.mpch-mainz.gwdg.de/)), the seamount in the South China Sea (Tu et al., 1992; Hékinian et al., 1989), ocean island basalt of Hainan Island (Wang et al., 2012), and Pacific MORB (Zhang et al., 2009, 2012a, 2012b, 2013).

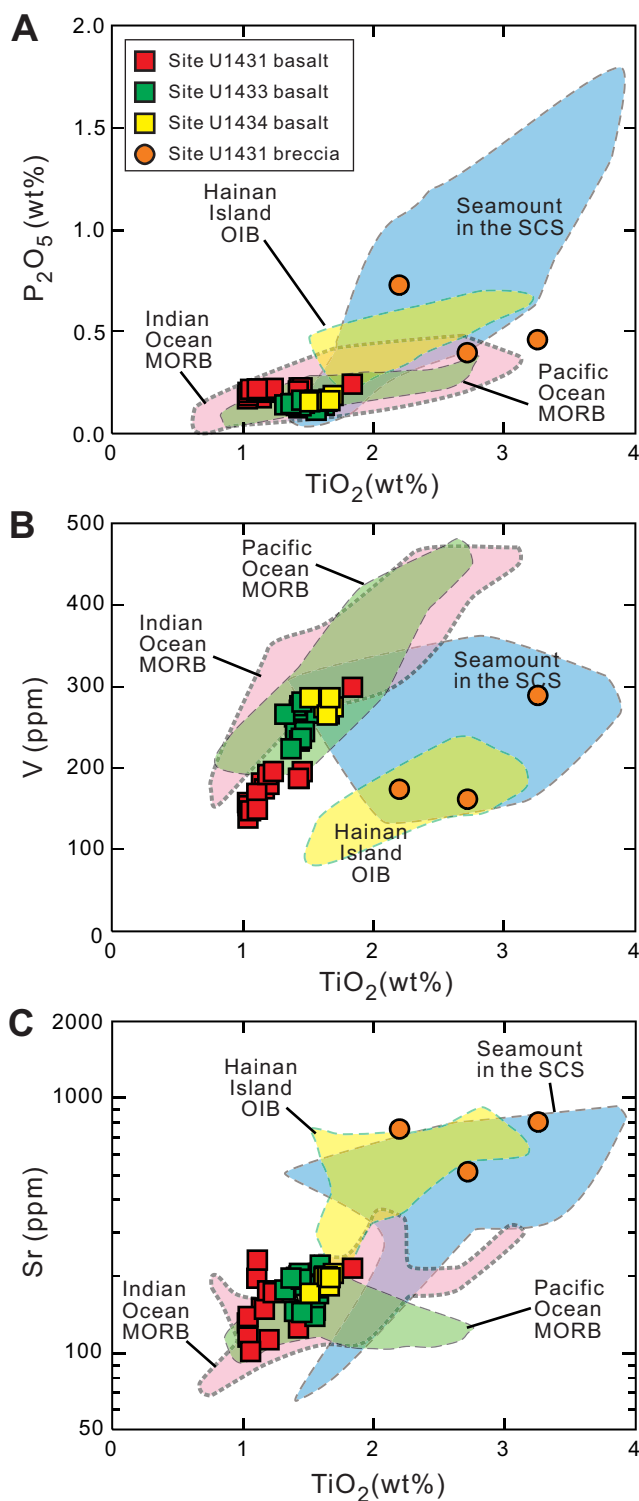
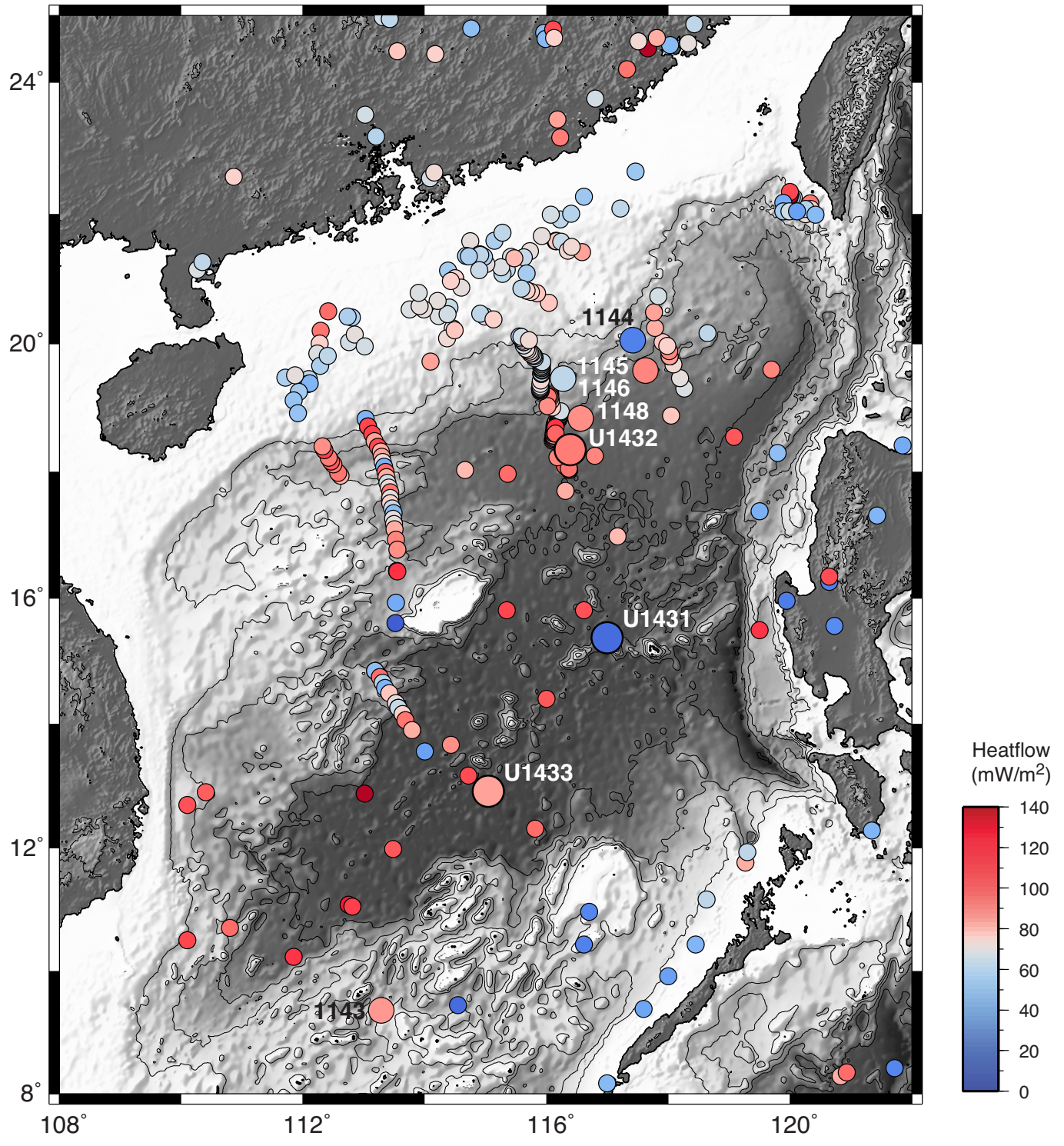
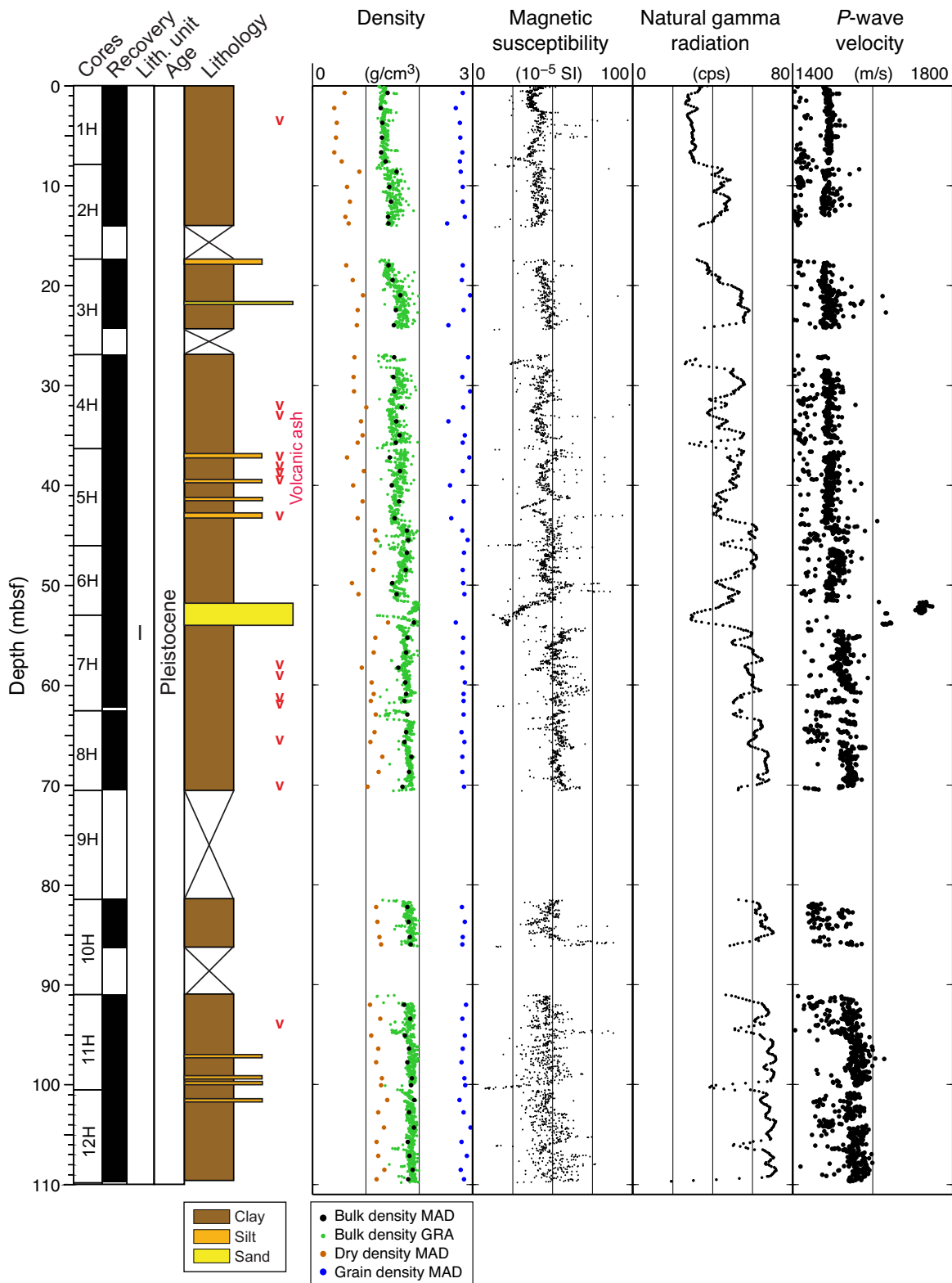


Figure F14. Map of heat flow values for Expedition 349 (large circles) and Ocean Drilling Program Leg 184 (large circles) and the compilation of heat flow data in Li et al., 2010 (small circles).



**Figure F15.** Lithostratigraphic and physical properties summary, Hole U1432C. Core magnetic susceptibility and gamma-ray attenuation (GRA) density (filtered) were measured on the Section-Half Multisensor Logger, moisture and density (MAD) were measured on discrete samples, and *P*-wave velocities were measured on the Section Half Measurement Gantry.



**Figure F16.** Age-depth model with estimated sedimentation rate for Hole U1432C based on biostratigraphic and paleomagnetic datums.

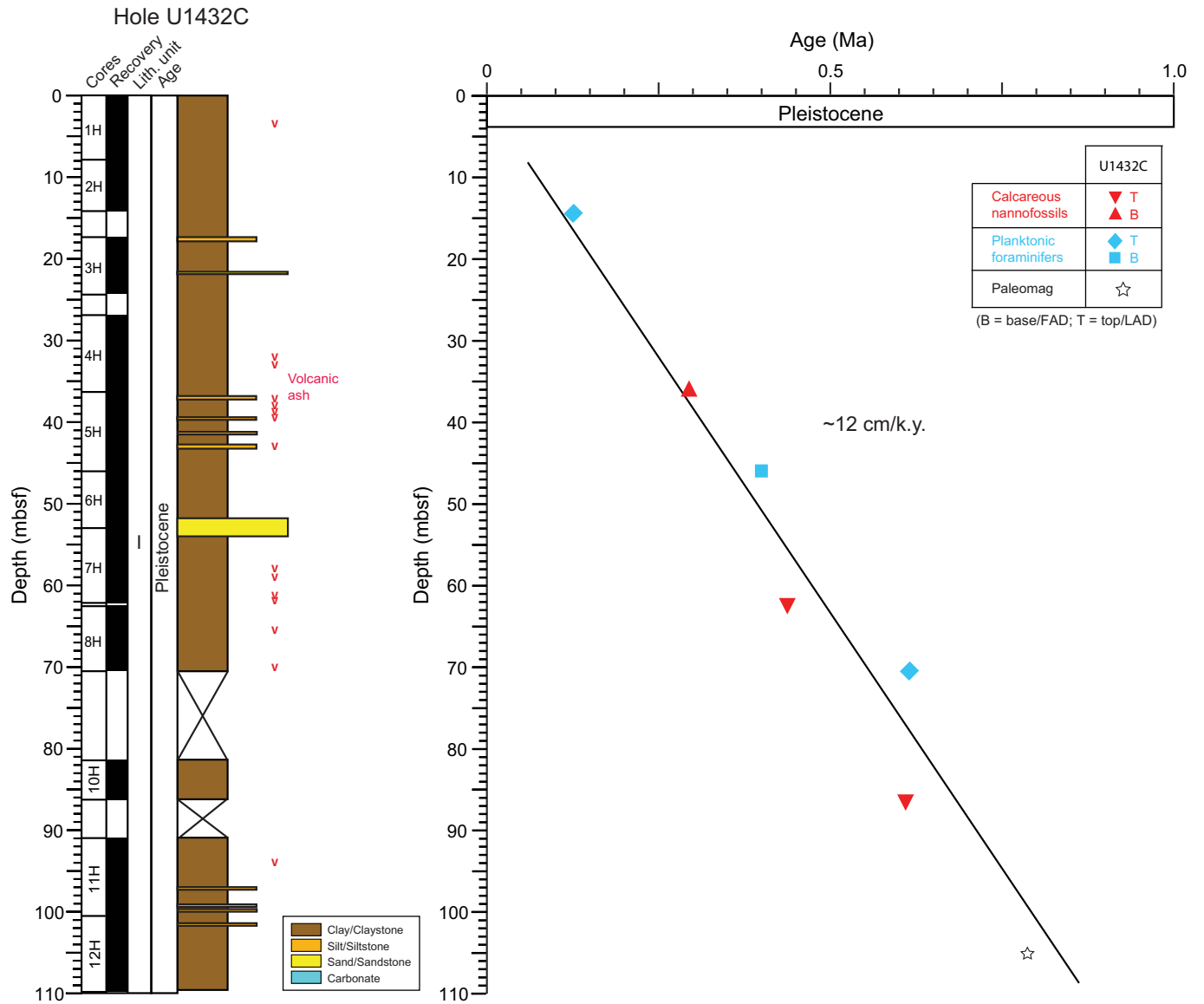


**Figure F17.** Lithostratigraphic and physical properties summary, Site U1433. Physical properties and downhole measurements are from Holes U1433A and U1433B. Core magnetic susceptibility and gamma-ray attenuation (GRA) density (filtered) were measured on the Section-Half Multisensor Logger, moisture and density (MAD) were measured on discrete samples, and *P*-wave velocities were measured on the Section Half Measurement Gantry. Downhole log data, magnetic susceptibility, and total natural gamma radiation are from the main pass of the triple combination tool string, and *P*-wave velocities are from the main pass of the Formation MicroScanner-sonic tool string. Downhole log depths have been shifted upward by ~2 m to correlate with the core physical property data.

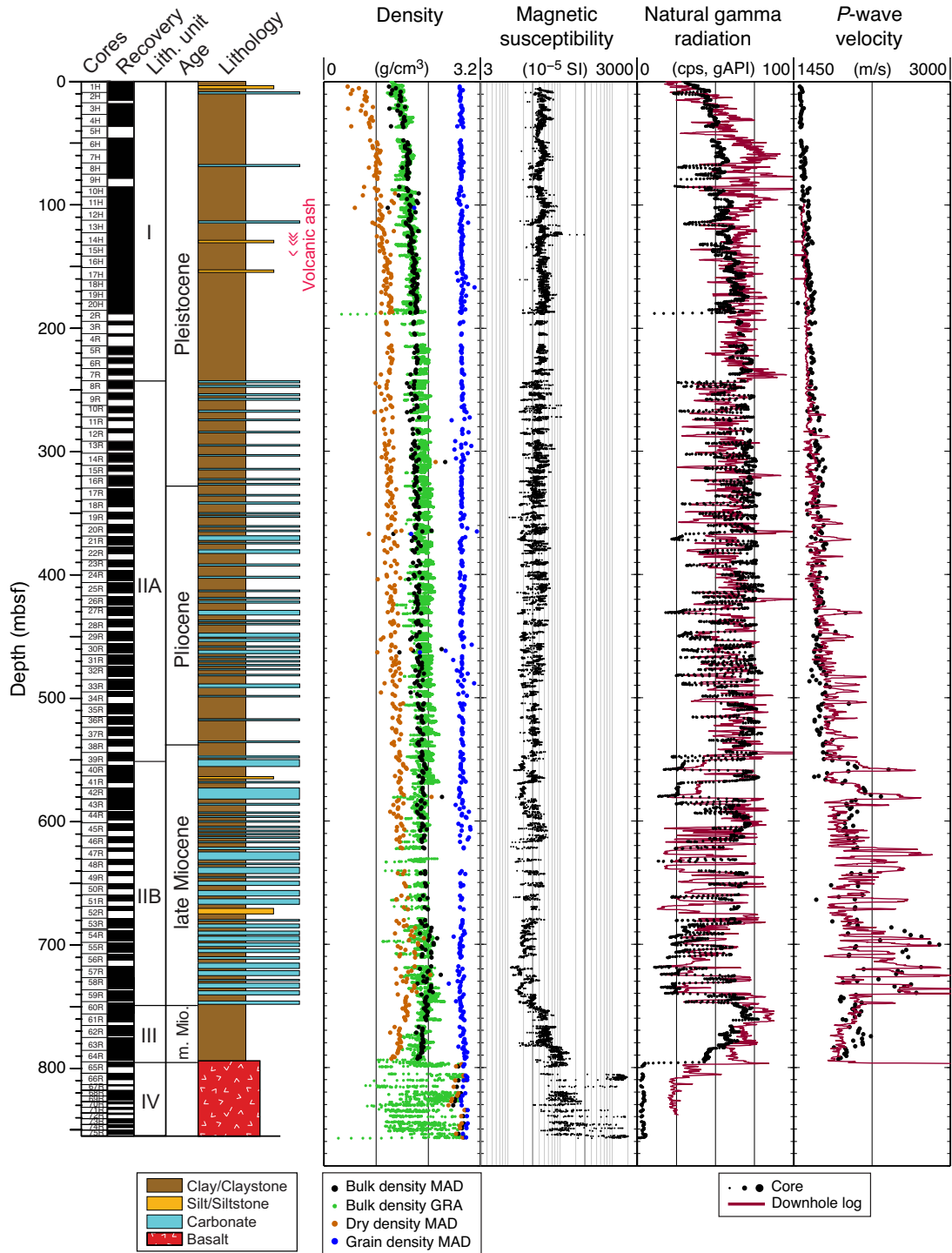


**Figure F18.** Age-depth model with estimated sedimentation rates for Site U1433 based on biostratigraphic and paleomagnetic datums. Dashed line indicates a tentative interpretation.

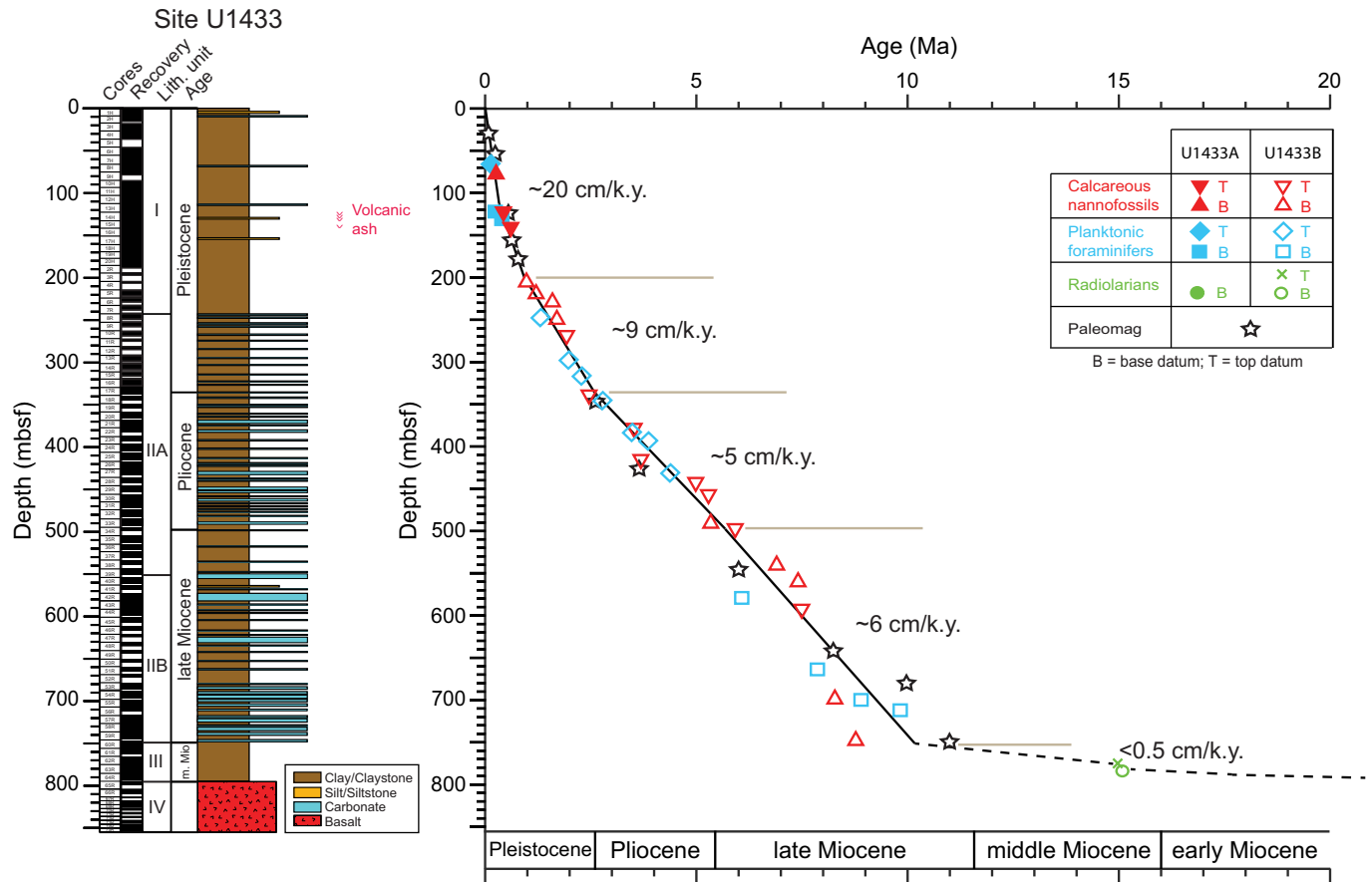


**Figure F19.** Lithostratigraphic summary of igneous rock and lithologic features, Hole U1433B. EOH = end of hole.

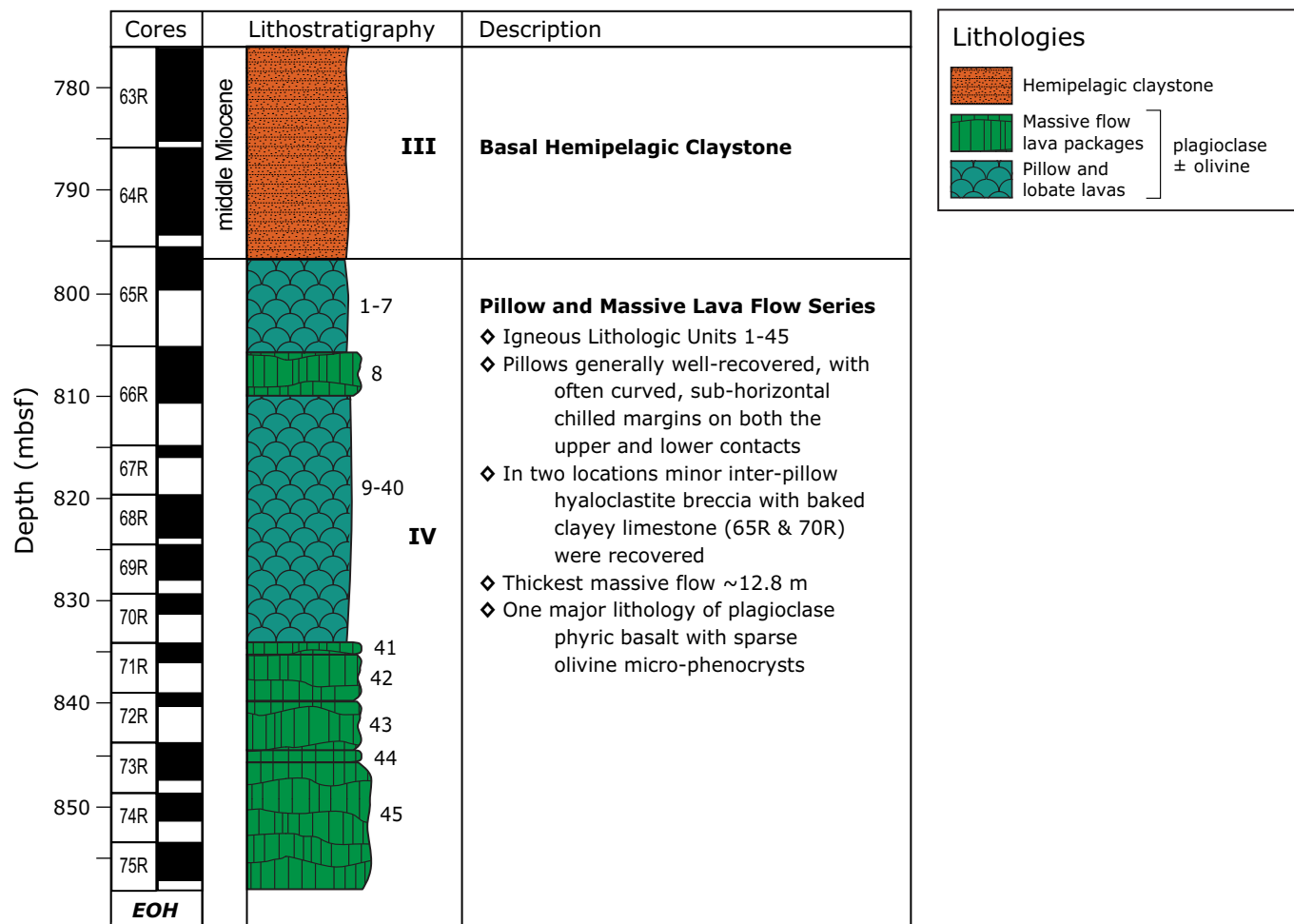


**Figure F20.** Downhole Formation MicroScanner (FMS) images showing basalt pillows in the 833–836 m WMSF interval, Hole U1433B.

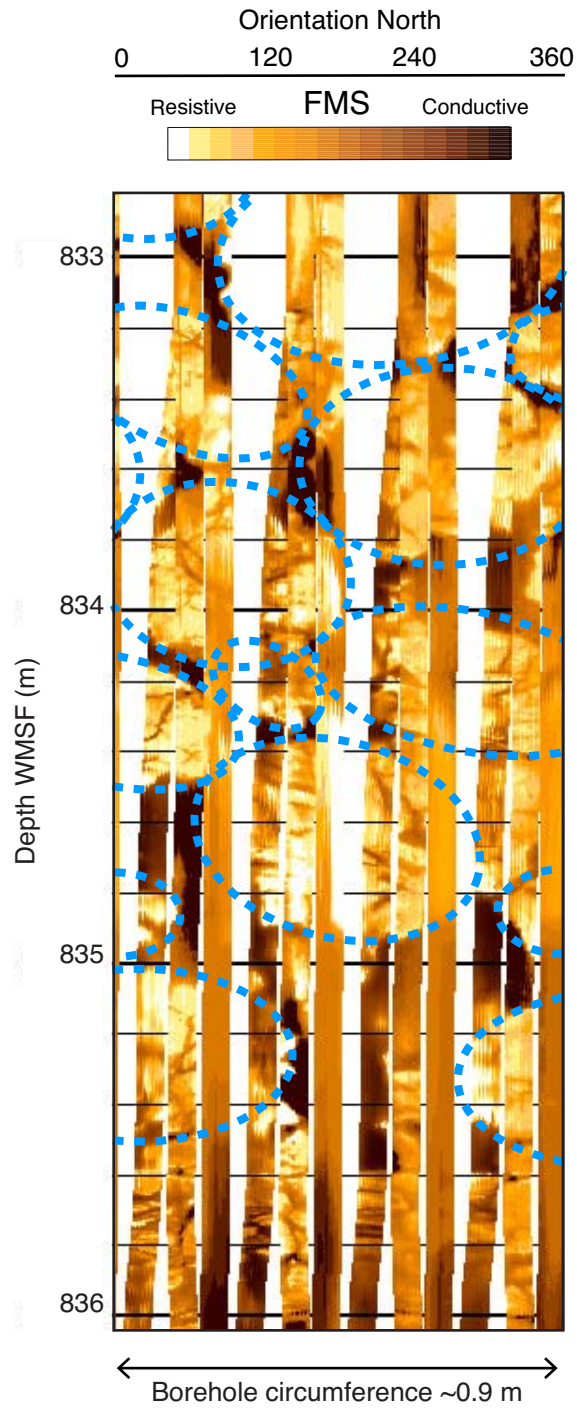


**Figure F21.** Lithostratigraphic and physical properties summary, Hole U1434A. Core magnetic susceptibility and gamma-ray attenuation (GRA) density (filtered) were measured on the Section-Half Multisensor Logger, moisture and density (MAD) were measured on discrete samples, and *P*-wave velocities were measured on the Section Half Measurement Gantry.

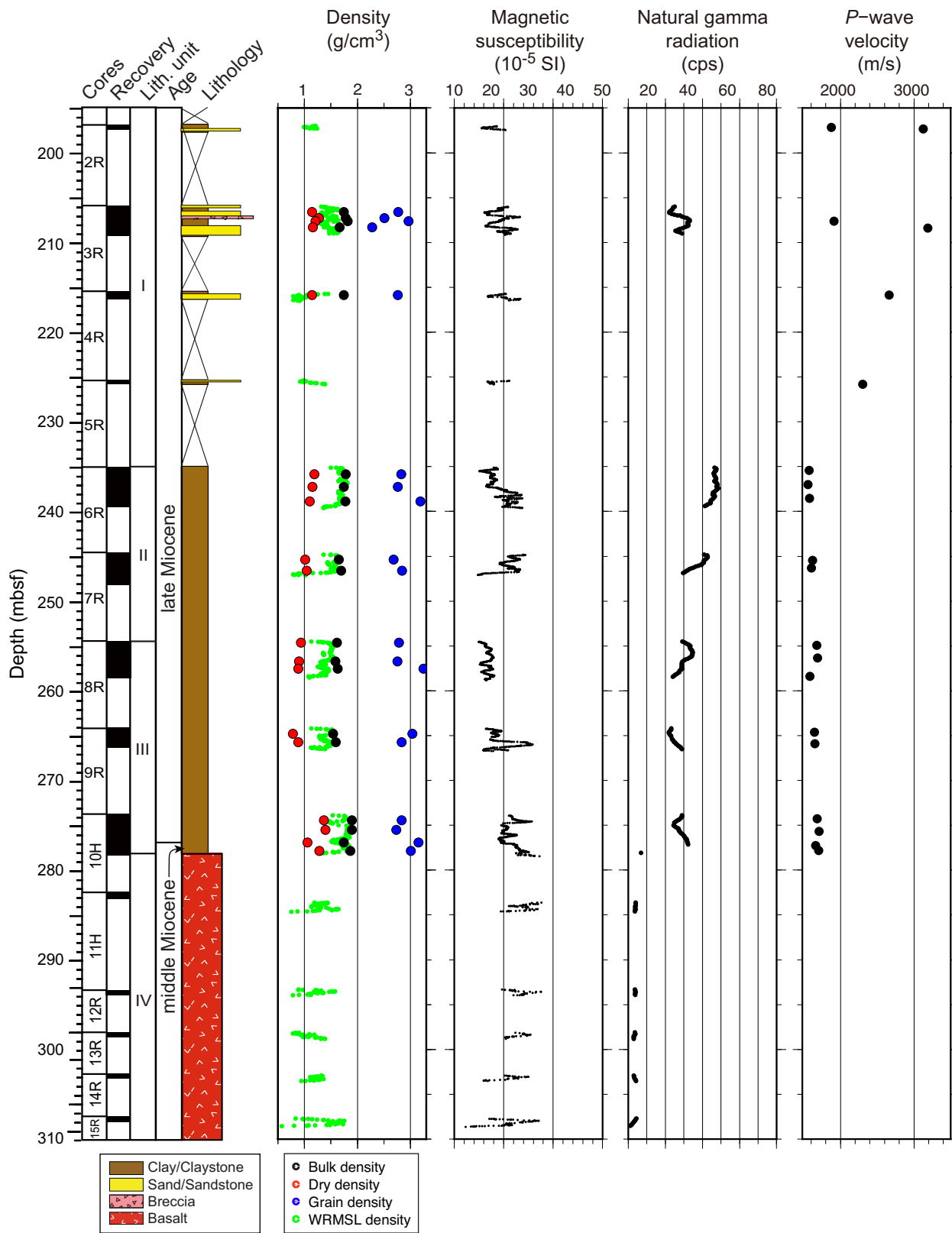


**Figure F22.** Age-depth model with estimated sedimentation rate for Site U1434 based on biostratigraphic and paleomagnetic datums.

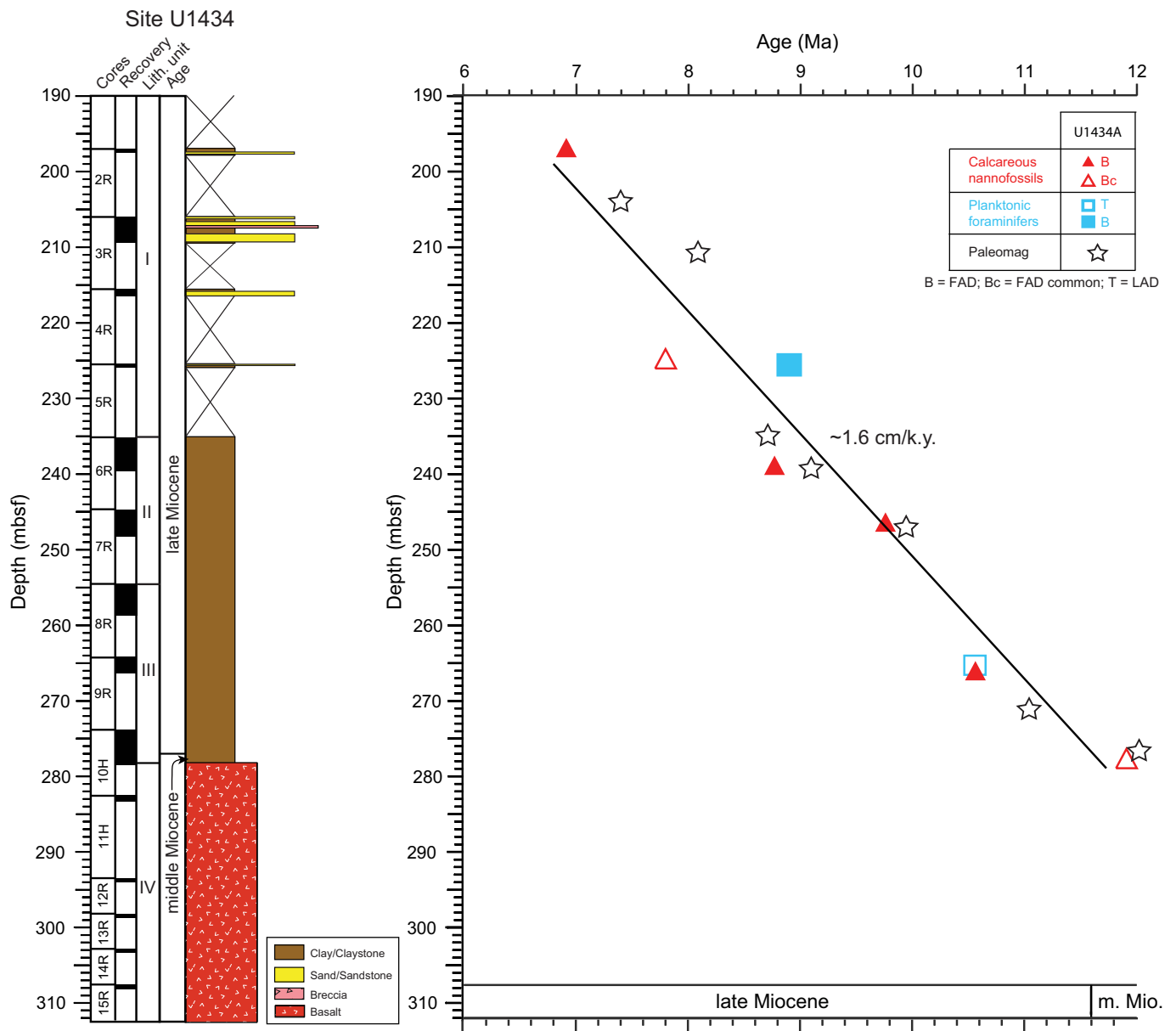


**Figure F23.** Lithostratigraphic summary of igneous rock and lithologic features, Hole U1434A. EOH = end of hole.

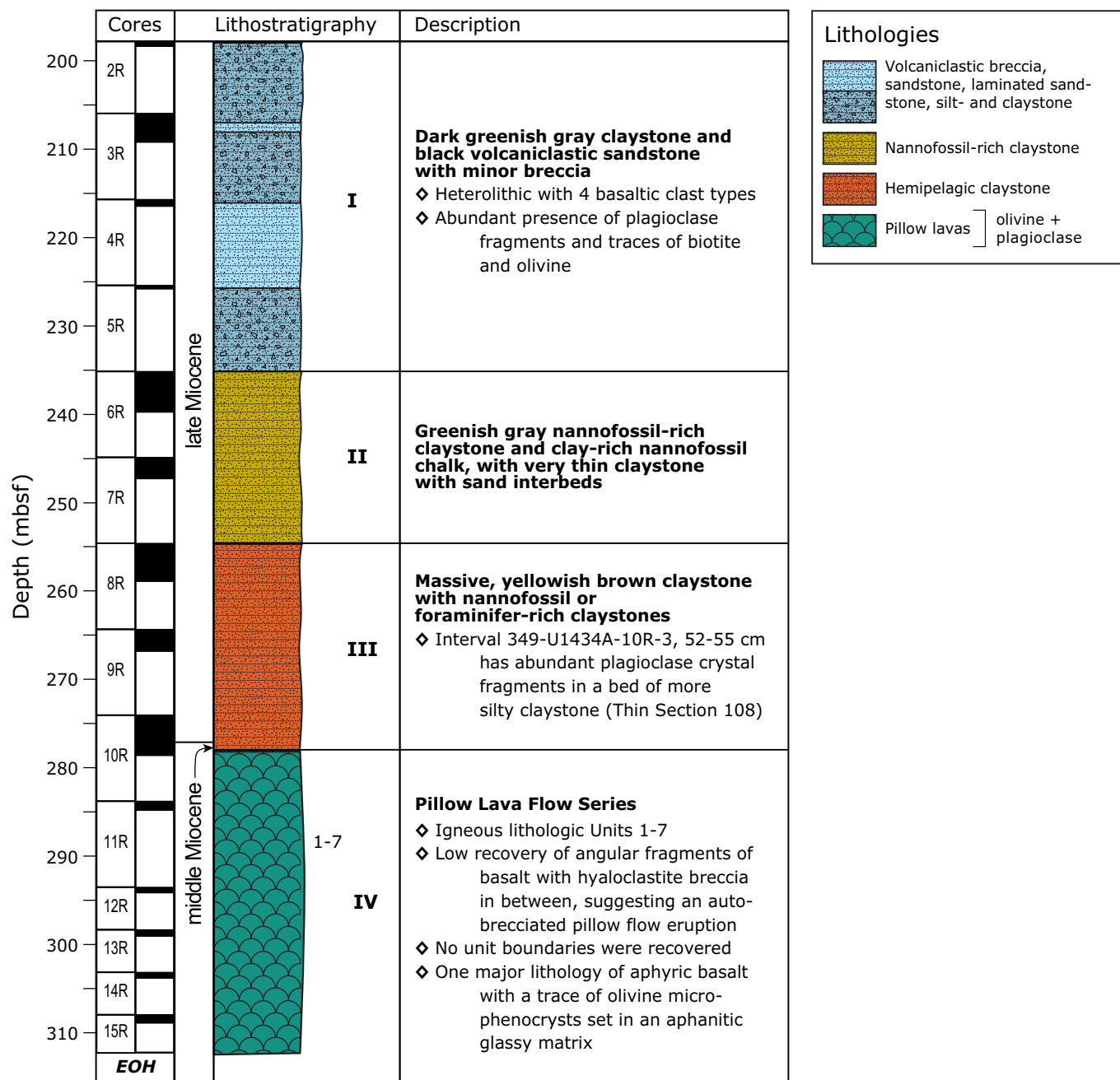


**Figure F24.** Lithostratigraphic and physical properties summary, Hole U1435A. Core magnetic susceptibility and gamma-ray attenuation (GRA) density (filtered) were measured on the Section-Half Multisensor Logger, moisture and density (MAD) were measured on discrete samples, and *P*-wave velocities were measured on the Section Half Measurement Gantry.

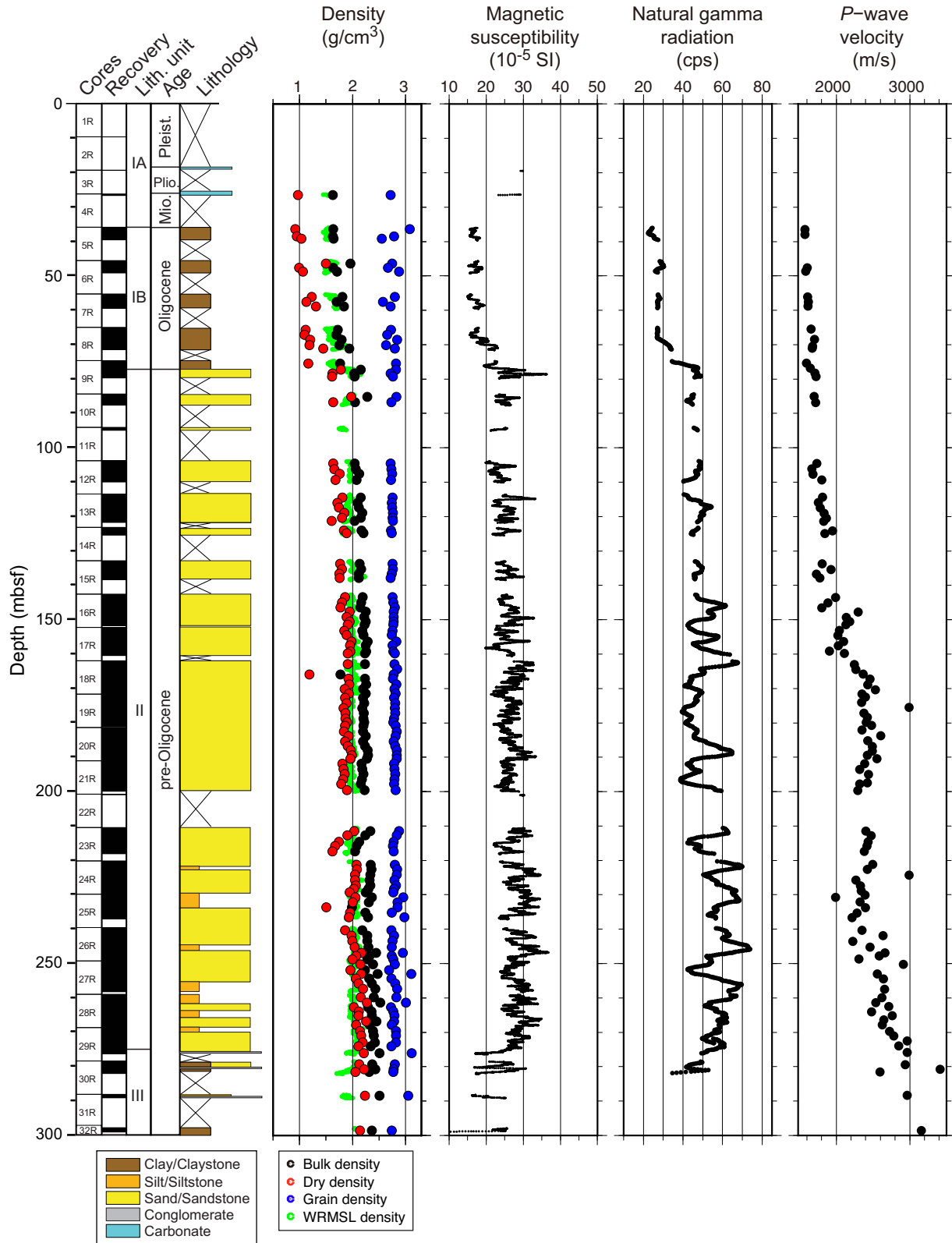


**Figure F25.** Age-depth model for Site U1435 based on biostratigraphic and paleomagnetic datums. Dashed line indicates a tentative interpretation. Wavy lines indicate possible hiatuses.

